Scalable Nickel-free Synthesis of Poly(pyrene-4,5,9,10-tetraone) and Stable Cycling in CNT/Ketjen Black-composite Electrodes for Sodium Batteries

Md. Adil,[a,b] Robin Wessling,[a,b,c] Niko Kokott,[a,b] Elena Mena-Osteritz,[a] Benedikt Prifling,[d] Markus Osenberg,[e] Thomas Diemant,[f] Volker Schmidt,[d] Ingo Manke[e] and Birgit Esser*[,a,b,f]

Affiliations:

[a] Institute of Organic Chemistry II and Advanced Materials, Ulm University, Albert-Einstein-Allee 11, 89081 Ulm, Germany. E-mail: birgit.esser@uni-ulm.de; Web: https://www.esserlab.com

[b] CELEST Green Energy Lab Ulm, Ulm University, Lise-Meitner-Str. 16, 89081 Ulm, Germany.

[c] Present address: Department for Energy Conversion and Storage, Technical University of Denmark (DTU), Anker Engelunds Vej 301, 2800 Kongens Lyngby, Denmark

[d] Institute of Stochastics, Ulm University, Helmholtzstraße 18, 89081 Ulm, Germany

[e] Institute of Applied Materials, Helmholtz-Zentrum Berlin für Materialien und Energie, Hahn-Meitner-Platz 1, 14109, Berlin, Germany

[f] Helmholtz Institute Ulm (HIU) Electrochemical Energy Storage, Helmholtzstraße 11, 89081 Ulm, Germany.

Table of contents

Materials and methods

Materials

Chemicals for electrode preparation and battery cell assembly. To prepare the negative electrodes for Na-based half-cells, sodium metal cubes (purity ≥ 99.95 % metal basis) were purchased from Sigma Aldrich. The electrolyte components, sodium hexafluorophosphate ($NaPF_6$, Purity ≥ 99+%), and anhydrous diethylene glycol dimethyl ether (DEGDME, purity ≥ 99.5%) were purchased from ThermoFischer Scientific and Sigma Aldrich, respectively. $NaPF_6$ and DEGDME were stored under argon prior to use. Singled-walled carbon nanotubes (SWCNTs, carbon content ≥ 98%, specific surface area ≥ 800 $m^2\ g^{-1}$), Ketjen Black EC-600JD (surface area ~1400 $m^2\ g^{-1}$), Super P carbon (Timical, surface area ~62 $m^2\ g^{-1}$) and polyvinylidene fluoride (PVDF, Kynar® HSV 900, Arkema) were purchased from Sigma Aldrich, Weber&Schaer, MTI Corporation, and Arkema, respectively. Ketjen black and SWCNTs were pre-dried at 80 ˚C for 2 days under vacuum. Whatman® glass microfiber separators (GF/D, binder-free, 0.67 mm thick, 257 mm diameter) and *N*-methyl-2-pyrrolidone (NMP, Acroseal®, 99.5%, dried and stored over molecular sieves) were purchased from Merck and ThermoFischer Scientific, respectively. CR2032-type coin cells were purchased from Shandong Gelon Lib Co., Ltd, China.

Chemicals for the synthesis of poly(pyrene-4,5,9,10-tetraone) (PPTO)

PTO	BLDpharm	98%
1,2-Propanediol	CarlRoth	≥99.5%
$B(OH)_3$	CarlRoth	≥99.5%
p-TsOH	CarlRoth	≥98%

$(B(pin))_2$	SIGMA-ALDRICH	99%
$[Ir(OMe)COD]_2$	SIGMA-ALDRICH	100%
4,4′-Di-*tert*-butyl-2,2′-dipyridyl (Dtbpy)	SIGMA-ALDRICH	98%
$Pd(OAc)_2$	SIGMA-ALDRICH	98%
$Cu(OAc)_2$	SIGMA-ALDRICH	98%

All other commercially available chemicals were purchased from SIGMA ALDRICH, ACROS ORGANICS, CARLROTH, VWR INTERNATIONAL, BLDPHARM or ALFA AEASAR (see above table) and were utilized without further purification. Anhydrous solvents were dried prior to use in a MBRAUN SPS-800 instrument. $Pd(OAc)_2$, $[Ir(OMe)COD]_2$, $(Bpin)_{2,}$ as well as dtbpy were stored under an argon atmosphere in a glove box with complete exclusion of moisture. PTO was bought from BLDPHARM in a purity of 98% and was used without further purification.

Preparation of the electrodes

Various electrodes with different electrode compositions were prepared with PPTO and PTO as active materials:

1) **Preparation of PPTO@CNTs@KB electrodes.** This composite electrode was prepared by first mixing PPTO (50 wt%) and SWCNTs (20 wt%) using a mortar and pestle and then adding Ketjen black (20 wt%) conductive carbon and PVDF binder (10 wt%) to the mixture. The dry mixture was dissolved/dispersed in NMP using a planetary centrifugal mixer (Thinky mixer, ARM 310) until a sanguineous-like slurry was obtained. The electrode formulation was stirred at room temperature for 30–40 minutes at 1500 rpm. The obtained honey-like slurry was uniformly cast onto an aluminum foil (GOODFELLOW,

thickness: 20 μm, ≥99.8%) using an automatic blade-coating machine equipped with heated plates (Proceq automatic film applicator, ZAA 2300) with a coating speed of 0.5 mm s^{-1}. The coated foil was dried under vacuum at 60 ˚C. The electrode was cut into a circular disk with a handheld electrode puncher (NOGAMI) with a diameter of 12 mm. The electrodes were further dried at 80 ˚C under vacuum before electrochemical cell fabrication. The average active-material mass loading in the dried electrode was between 0.5-0.6 mg cm^{-2}.

2) **Preparation of PPTO@CNTs@KB electrodes with higher active material content.** A composite electrode was prepared with a higher content of PPTO using the same procedure as mentioned in 1). Briefly, PPTO, SWCNTs, Ketjen Black, and PVDF binder were mixed in a weight ratio of 70:15:10:05. The average active-material mass loading lay between 0.5–1.0 mg cm^{-2}.

3) **Preparation of PPTO@KB and PPTO@Super P electrodes.** The conventional electrodes using Ketjen black and Super P conductive carbon were prepared following the same procedure as mentioned in 1). Briefly, PPTO, conductive carbon (Ketjen black or Super P), and PVDF binder were mixed in a 50:40:10 weight ratio. The average active-material mass loading in the final dried electrode for PPTO@KB and PPTO@Super P was in the range of 0.4–0.6 mg cm^{-2}.

4) **Preparation of PPTO free-standing electrodes.** The PPTO/CNT free-standing binder and current collector free electrode was prepared in a 1:2 (PPTO:SWCNTs) weight ratio. To prepare the free-standing PPTO buckypaper electrode, the following procedure was applied. At first, SWCNTs were added to 20 mL of ethanol (purity ≥99.50%, SIGMA ALDRICH), and the dispersion was sonicated using a probe-type sonicator (FISHERBRAND™, FB120, USA) for 20 minutes. Subsequently, a calculated amount of PPTO powder was added to the mixture and further sonicated for 20 minutes. After that, the solution mixture

was kept to stir overnight over a magnetic stirrer (IKA RCT standard) at room temperature to ensure homogeneity. The obtained ink-like suspension was filtered using a poly(vinylidene fluoride) microporous membrane (0.22 µm pore size, 47 mm thick, Durapore, MERCK) with the aid of vacuum filtration, and thoroughly washed with ethanol. The resulting free-standing buckypaper film was dried at 60 ˚C under vacuum. The composite electrode is a self-standing, polymer-supported, metallic current collector and binder-free buckypaper film, cut in a circular disk of 10 mm and directly applied as electrode.

5) **Preparation of PTO@CNTs@KB electrodes.** The composite electrode using the PTO small molecule was prepared using the same procedure as mentioned in 1). Briefly, PTO monomer, SWCNTs, Ketjen black, and PVDF binder were mixed in a weight ratio of 50:20:20:10. The active-material mass loading in the final dried electrode (diameter: 12 mm) lay between 0.6–0.8 mg cm^{-2}.

6) **Preparation of PTO@KB electrodes.** Composite electrodes using the PTO small molecule and Ketjen black conductive carbon, and PVDF binder in a 50:40:10 weight ratio were prepared using the method mentioned in 1). The active-material mass loading in the final dried electrode (diameter: 12 mm) was in the range of 0.5–0.8 mg cm^{-2}.

7) **Preparation of carbon-based electrodes.** Three carbon-based electrodes were prepared to maintain the same ratio as in the PPTO@CNTs@KB, PPTO@KB, and PPTO free-standing buckypaper electrodes.

    I. **SWCNTs, KB, and PVDF carbon electrodes.** The electrodes were prepared by mixing SWCNTs, Ketjen black carbon, and PVDF binder in a weight ratio of 40:40:20. The mixture was dissolved in NMP to obtain a homogenous suspension and cast onto aluminum foil, as mentioned in 1).

The dried electrodes were cut into 12 mm circular disks and directly used. The carbon loading in the final dried electrodes ranged between 0.7–0.8 mg cm^{-2}.

II. **Ketjen black and PVDF carbon electrodes.** The electrodes were prepared using the same procedure as mentioned in 1). Specifically, Ketjen black and PVDF binder were mixed in a 80:20 weight ratio. The dried electrode was cut into a circular disk with a diameter of 12 mm. The carbon loading in the final electrode was in the range of 0.6–0.7 mg cm^{-2}.

III. **SWCNT free-standing electrodes.** The free-standing SWCNT electrodes were prepared following the same procedure as mentioned in 4), using only SWCNT powder. The dried electrode was cut into a circular disk with a diameter of 10 mm. The carbon loading in the final dried electrode ranged between 1.7–2.5 mg cm^{-2}.

8) **Preparation of electrodes for post-cycling characterizations.** For the post-cycling studies, the electrodes were prepared in a similar way as mentioned in 1). Typically, PPTO, SWCNTs, Ketjen black, and PVDF binder were mixed in an 80:10:05:05 weight ratio. The dried electrode was cut into a 12 mm circular disk, having an active-material mass loading of 0.9–1.1 mg cm^{-2}.

Preparation of electrolytes

For the Na-based cells, $NaPF_6$ and DEGDME were used as received. However, both chemicals were kept under vacuum for 2 days and further inside an argon atmosphere before breaking the seal. In a fresh vial, a calculated amount of $NaPF_6$ and DEGDME solvent was added to obtain a 1 molar (M) concentration and kept to stir overnight inside a glove box (O_2 and H_2O levels < 0.5

ppm) to form a homogenous solution. The prepared electrolyte was transparent and colorless and handled inside the glove box. The other two electrolytes, viz., 1 M $NaClO_4$ in TEGDME and 4 M $NaPF_6$ DME, were prepared similarly.

Dissolution experiments

Solubility tests of PPTO and PTO powder in the battery electrolyte: The solubility test of the PPTO and PTO powder samples was carried out in the battery electrolyte (1 M $NaPF_6$ DEGDME) under an argon atmosphere. Briefly, a pinch of powder sample was added to the battery electrolyte and left for 2 days inside a glove box to observe the change in electrolyte color. The PPTO powder did not show any sign of dissolution as judged by the lack of coloring of the battery electrolyte. However, the PTO small molecule readily dissolved into the electrolyte making the battery electrolyte orange in color.

Solubility test of PPTO electrodes prepared with different conductive carbons in the battery electrolyte: The solubility test of the PPTO electrodes with various conductive carbon additives (viz., PPTO@CNTs@KB, PPTO@KB, and PPTO@Super P) at the fully-discharged state was conducted under an argon atmosphere in the battery electrolyte (1 M $NaPF_6$ DEGDME). Typically, Na-ion-based half-cells (CR2032) containing PPTO@CNTs@KB, PPTO@KB, or PPTO@Super P electrodes were discharged to 1.0 V *vs.* $Na^+|Na$, disassembled inside a glove box, and the electrodes were immersed in the battery electrolyte for several weeks. PPTO@KB and PPTO@Super P electrodes exhibited dissolution of active material into the electrolyte with time. After 15 weeks, the battery electrolytes containing these two electrodes turned completely black, confirming the high dissolution of electrode components in the electrolyte. The discharged PPTO@CNTs@KB electrode, on the other hand, inhibited the dissolution of the electrode components, as judged by the absence of color change of the battery electrolyte, even after 15-weeks.

Material characterizations

NMR spectroscopy. NMR spectra were recorded on BRUKER Avance Neo 400 and BRUKER Avance Neo 600 instruments (^{1}H: 400 MHz or 600 MHz, ^{13}C 101 MHz or 151 MHz) at 298 K. $CDCl_3$ and DMSO-d_6 were used as solvents, and the spectra were calibrated to the corresponding solvent peak (^{1}H NMR: 7.26 ($CDCl_3$), 2.50 (DMSO-d_6); ^{13}C NMR: 77.2 ($CDCl_3$), 39.5 (DMSO-d_6). ^{13}C solid-state NMR spectra were referenced against adamantane (37.78). NMR chemical shifts (δ) are denoted in ppm and coupling constants (J) in Hz. The NMR data are given in our previous report.[1]

Gel-permeation chromatography. The molecular weight and dispersity of the obtained polymers were measured with a polystyrene matrix-based SECcurity GPC System from AGILENT TECHNOLOGIES (1260 Infinity) with THF as an eluent. For calibration, polystyrene standards by PSS Polymer Standards Service were used.

MALDI mass spectra were measured on a BRUKER UltrafleXtreme MALDI TOF/TOF using trans-2-[3-(4-tert-Butylphenyl)-2-methyl-2-propenylidene]malononitrile (DCTB) as matrix material.

Thermogravimetric Analysis (TGA) measurements were conducted on a TGA 8000 by PERKIN ELMER.

Differential scanning calorimetry (DSC) measurements were conducted on a DSC 2 STARe System by METTLER-TOLEDO.

Column chromatography. Column chromatography was performed using silica 60 with a particle size of 0.04 – 0.063 mm from MACHEREY-NAGEL. For the adsorption of the crude products, celite® was used.

ATR-FT-IR spectroscopy. Fourier-transform infrared spectroscopy (FT-IR) was performed on a BRUKER Alpha II FT-IR spectrometer equipped with a diamond ATR unit. The FT-IR spectra of the PPTO (protected) and PPTO (de-protected) powder samples were recorded in transmission mode within the range of 100-4000 cm^{-1}. However, the FT-IR spectra of the charged and discharged electrodes were acquired in absorbance mode within 600–4000 cm^{-1}. All the FT-IR spectra were recorded in ATR mode.

Surface-enhanced laser Raman spectroscopy. Raman measurements were performed with an inVia confocal Raman spectrometer (RENISHAW) equipped with a 532 nm solid-state laser as the excitation light source, operating at a power of 25 mW. The spectra were acquired through a 50X Carl Zeiss objective lens, with a 10-second acquisition time, over the spectral range of 1000–2000 cm^{-1}.

X-ray powder diffraction. The solid-state structure and phase purity of the PPTO powder sample were characterized using X-ray powder diffraction (XRD, Stoe STADI PXRD diffractometer) in Debye-Scherrer geometry using a molybdenum (Mo) Kα X-ray source ($\lambda = 0.709$ Å) at an operating current and voltage of 30 mA and 40 keV, respectively. The diffraction pattern was recorded within the angular range of 5°–70° (2 theta) with a 2° per minute step size.

Scanning-electron microscopy. The morphology of the as-prepared powder sample and various charge-discharged electrodes was investigated by scanning-electron microscopy (SEM, THERMOFISHER Scientific Apreo 2 SEM) with a spatial resolution of 1.00 nm at an accelerating voltage of 40 kV. In addition, energy-dispersive X-ray spectroscopy (EDS) was used for the determination of the elemental compositions and mapping.

X-ray photoelectron spectroscopy. The chemical state of the sample surfaces was analyzed by X-ray photoelectron spectroscopy (XPS) measurements on a Specs XPS system with a Phoibos 150 energy analyzer. The spectra were recorded using monochromatized Al Kα radiation (300 W, 15 kV) and pass energies of 90 and 30 eV for survey and detail measurements, respectively. All binding energies were calibrated to the C1s peak of C-C/C-H species at 284.8 eV. To avoid surface contamination, the samples were transferred in an inert gas atmosphere to the sample load lock of the XPS system. The peak fit of the XPS results was done with CasaXPS, using Shirley-type backgrounds and Gaussian-Lorentzian (GL30) peak shapes.

Electrochemical characterizations

All electrochemical tests were conducted in two-electrode coin-cells (CR2032) that were assembled inside a glove box, using a Biologic MPG-2 potentiostat at room temperature. Electrodes of PPTO with various conducting carbon additives and sodium foil were used as working and counter electrodes, respectively, and a glass fiber disk (16 mm, Whatman GF/D) was used as separator. 1 M $NaPF_6$ in DEGDME, 1 M $NaClO_4$ in TEGDME and 4 M NaPF6 in DME were used as electrolytes (100–110 microliters per cell). The galvanostatic charge/discharge and rate capability measurements were conducted within 1.0–3.5 V *vs.* Na^+|Na. The galvanostatic intermittent titration technique (GITT) was employed to determine the Na^+ diffusion coefficients. The GITT measurements were performed by applying a current impulse of 200 mA g^{-1} for 10 minutes, followed by a 4-hour relaxation time. Electrochemical impedance spectroscopy (EIS) experiments were performed in potentiostatic mode at various discharge/charge potentials. A sinusoidal perturbation signal of 10 mV amplitude was applied across a frequency range spanning from 100 kHz to 10 mHz with 15 logarithmically spaced points per decade. The specific capacity of the cell is based on the active material PPTO/PTO mass unless otherwise mentioned. The cells were allowed to rest for ~12 hours before the start of cycling.

Tomographic imaging

The electrode samples were prepared on standard 12.5 mm aluminum specimen pins (Agar Scientific) using EM-Tec AG44 conductive silver paint (Micro to Nano). To avoid contamination of the central regions of interest, silver paint was applied only at the edges. In order to preserve the native structure, the samples were not infiltrated with resin. To ensure good conductivity and to protect the surface from gallium beam damage, a gold coating was applied using a Cressington 108 Auto sputter coater. FIB tomography was performed using a Zeiss Crossbeam 340 at the Correlative Microscopy and Spectroscopy facility at Helmholtz-Zentrum Berlin (HZB). The SEM working distance was set to the crossover point at 5.2 mm. For initial trench milling, a gallium-ion beam at 30 keV with a current of 30 nA was used to create a square opening. The final edge intended for tomography was polished using a 3 nA current at 30 keV. Serial sectioning was conducted with a slicing interval of 10 nm. To minimize electron interaction volume and lower edge artefacts, the acceleration voltage was reduced to 1 keV (close to the minimum at the given working distance), a 30 µm aperture was used. The low acceleration voltage also resulted in a shallow depth of field, aiding the later suppression of shine-through artifacts. Images were acquired with a pixel size of 10 nm (x and y), using the microscope tilt compensation and dynamic focus. Each image took 23.3 seconds to capture. During tomography, two detectors were used simultaneously: the chamber SE2 detector and the InLens SE detector. The differing shadowing effects captured by the two signals were later leveraged for improved structural reconstruction.

Tomographic image processing

Each of the two tomography datasets comprises approximately 4.5 billion voxels, corresponding to an edge length of approximately 1650 voxels (16.5 µm). As a first preprocessing step, a drift correction was performed using the "Descriptor-Based Series Registration" plugin in ImageJ/Fiji[2], referencing the uppermost region of each section where no milling had occurred and only the sample surface was visible. Subsequently, intensity normalization of the milled cross-sectional areas was carried out using an average depth projection of the entire stack as a correction pattern. This normalization was applied to both detector channels. In addition to the original SE2 and InLens signals, a third signal was generated by applying a 3D Gaussian blur ($\sigma = 100$) to the chamber signal SE2 dataset. These three signals were combined into an RGB image stack, which was then used to train a random forest classifier for multi-channel image segmentation[3] using Ilastik.[4] The trained classifier effectively removed background and shine-through artifacts, producing a binary dataset where Class 1 represented the true milled surface and Class 2 encompassed all other regions. Following segmentation, a local thickness filter combined with region growing techniques was applied to further differentiate highly porous areas from denser, polymer-rich regions, leading to a total of three classes: active material (AM), carbon-binder domain (CBD, i.e., the union of conductive additives and binder), and pore space (P).

Geometrical descriptors

The segmented 3D image is the basis for a quantitative characterization of the 3D microstructure via the following geometric descriptors: Volume fraction, specific surface area, chord length distribution, geodesic tortuosity, connectivity, and the distribution of local volume fraction. The detailed information regarding the formal definition and the estimation of these geometrical descriptors is given in our previous report.[5] Note that the computation of the distribution of local volume fraction is carried out by computing the volume fraction of the considered phase separately for non-overlapping cubic cutouts with a side length of 1 µm. Moreover, note that connectivity is defined as the ratio of the volume of the largest connected component (with respect to the 26-neighborhood) of a predefined phase and the volume of this phase.

Quantum-chemical calculations

Density-functional theory (DFT) calculations were performed with the Gaussian 16 program package. The optimum geometries of all molecules and charged species were first fully optimized in the gas phase with the B3LYP hybrid functional and a 6-311++G(d,p) basis included in the Gaussian16 package.[53] To take into account small changes in geometry when going from gas to solvent, we re-optimized the geometry of the molecule in DEGDME. We used a continuum solvation model approach (SMD variation of IEFPCM protocol) in which the full solute electron density was used without defining partial atomic charges, and the solvent was represented as a 7.5 dielectric constant medium (to simulate the DEGDME solvent) with surface tension at the solute−solvent boundary. In some special cases, additional calculations were made, treating explicitly solvent molecules close to the cations before applying the continuum SMD. Frequency calculations in the gas phase and in solution were carried out to validate the optimum geometry convergence and to obtain zero-point energies and thermal corrections in order to convert the internal energies to the Gibbs energies at 298.15 K. The connection between the gas and solvent phases was obtained through the calculation of the solvation Gibbs free energy of all species. Time-dependent DFT calculations were performed for the analysis of the electronic transitions at the B3LYP/6-311++G(d,p) level. Frontier orbitals plots and electrostatic potential surfaces were generated with GaussView 6.1.1[54]

Synthetic procedures and thermal characterization

Poly(4,5,9,10-tetra(propyleneglycol)ketal-pyrene) (P(PTO$_{PrG}$) (with Figures S1-S4)

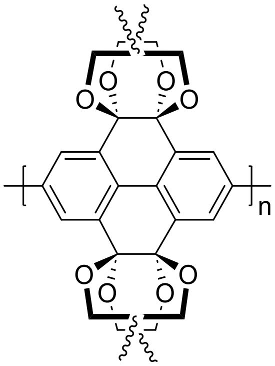

P(PTO$_{PrPG}$) was synthesized following a modified procedure by MINUS *et al.*[6]

PrG-protected PTO bis(boronic ester) **2** was synthesized according to our previously published protocol.[1] **2** (747 mg, 1.00 mmol), $B(OH)_3$ (310 mg, 5.01 mmol, 5.0 eq.), $Pd(OAc)_2$ (14.0 mg, 60 µmol, 6 mol-%) and $Cu(OAc)_2$ (20.1 mg, 100 µmol, 10 mol-%) were dissolved in DMSO (11.2 mL)[1] in an open vial[2] and stirred at room temperature[3] for 40 h.[4] Subsequently, the reaction mixture was added dropwise to stirred MeOH (50 mL).[5] The resulting precipitate was separated by centrifugation and purified by two cycles of washing in an ultrasonic bath (10 min each) and

---

[1] Regular DMSO with water content.

[2] Screw-cap vial covered with a paper wipe to prevent particles from entering.

[3] Reaction mixture was kept at constant temperature by positioning the vial in a sand bath.

[4] The clear, greenish solution turns opaque.

[5] At this point, the polymer had already partly precipitated.

centrifugation in MeOH (35 mL). Afterwards, the crude polymer was dissolved in $CHCl_3$ / toluene[6] and precipitated from MeOH/H_2O (5:1, v:v; 35 mL). Centrifugation and drying at 60 °C under high vacuum ($<10^{-2}$ mbar) yielded the title compound (258.1 mg, 52%) as a dark yellow, glassy solid.

^{1}H NMR (600 MHz, $CDCl_3$, sample contains traces of toluene with m at $\delta = 7.16$ and s at $\delta = 2.35$ and CH_2Cl_2 with s at $\delta = 5.34$): $\delta = 8.50$–7.96 (m, 4H, Ar-H), 7.83–7.73 (m, 8% of 4H, Ar-$H_{endgroup}$), 7.55–7.45 (m, 8% of 2H, Ar-$H_{endgroup}$),[7] 4.95–4.45 (m, 17% of 12H, CH), 4.43–3.79 (m, 51% of 12H, CH/CH_2), 3.78–3.13 (m, 32% of 12H, CH_2), 1.54–1.17 (m, 54% of 12H, CH_3), 1.15–0.64 (m, 46% of 12H, CH_3).

^{13}C NMR (150 MHz, $CDCl_3$, sample contains traces of toluene with s at $\delta = 138.01$, 129.17, 128.36, 125.44 and 21.59): $\delta = 141.82$, 134.30, 133.82, 128.61, 125.96, 93.62, 93.04, 92.26, 91.69, 69.62, 68.80, 64.71, 24.87, 16.76, 16.49, 16.02.

^{13}C MAS-NMR (100 MHz, 14 kHz, Adamantane): $\delta = 141.34$, 134.81, 128.06, 125.59, 92.42, 69.18, 64.35, 24.74, 15.53.

Anal. GPC (THF, polystyrene as standard, MWD (254 nm): $\bar{M}_n = 4.41 \cdot 10^3$ g mol^{-1}, $\bar{M}_w = 7.37 \cdot 10^3$ g mol^{-1}, Đ = 1.67.

---

[6] Polymer is more soluble in $CHCl_3$ but precipitates better from toluene. Thus, it is dissolved in a generous amount of $CHCl_3$, then few drops of toluene are added and the $CHCl_3$ is removed under reduced pressure to yield a highly concentrated solution in toluene for precipitation.

[7] These two multiplets are caused by the arylic endgroup protons in *para*-position (orange in **Error! Reference source not found.**S4) and *meta*-positions (red in **Error! Reference source not found.**S4). Integration suggests an end-group content of 8%.

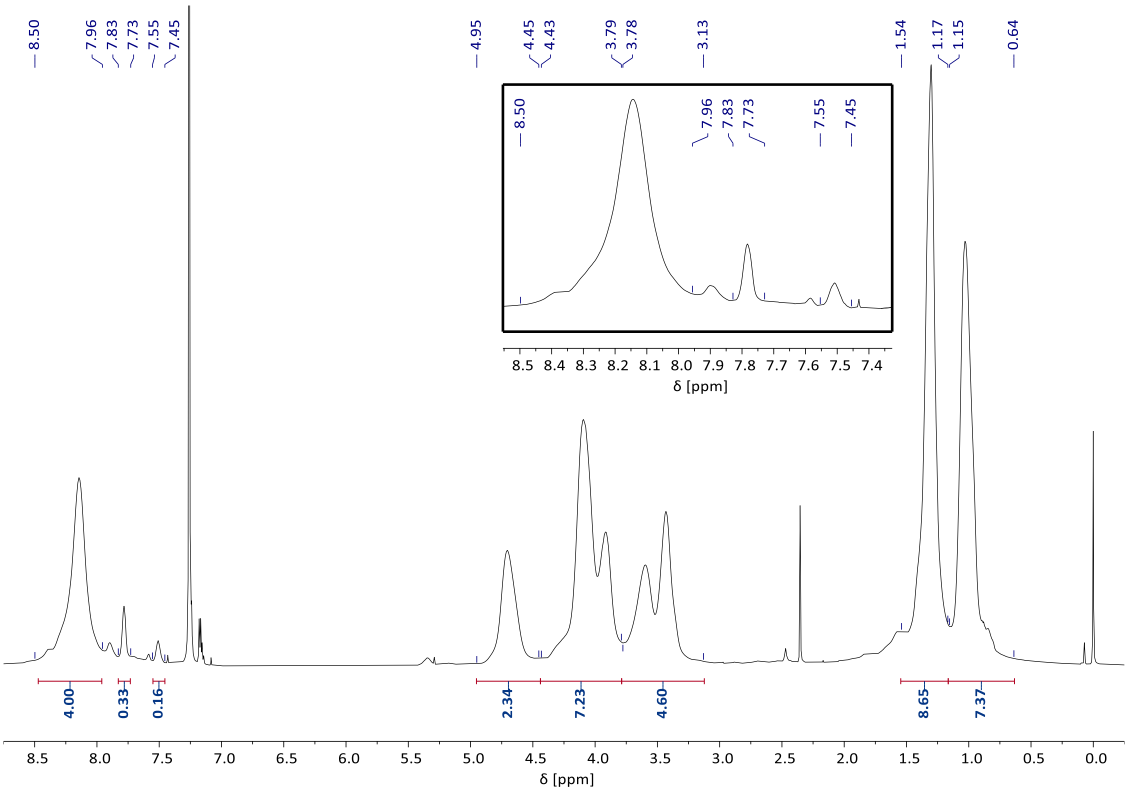

Figure S1: ^{1}H NMR spectrum of P(PTO$_{PrG}$) in CDCl$_3$ (600 MHz).

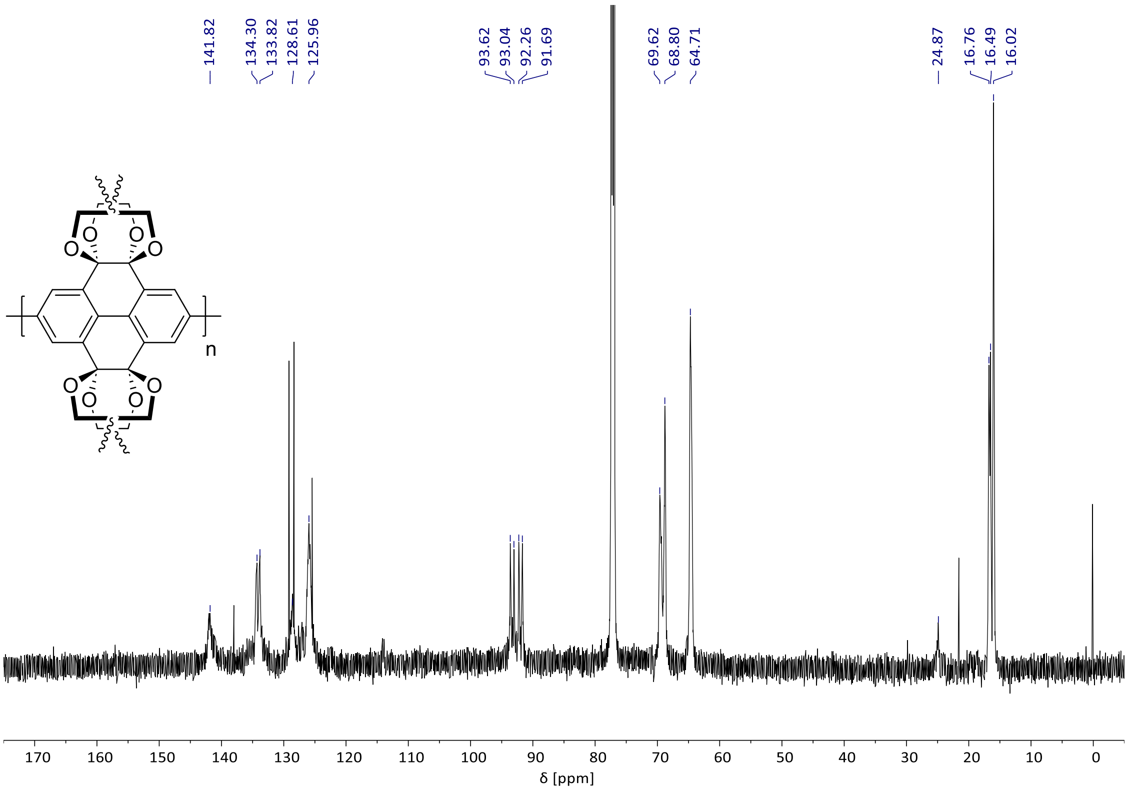

Figure S2: ^{13}C NMR spectrum of P(PTO$_{PrG}$) in CDCl$_3$ (151 MHz).

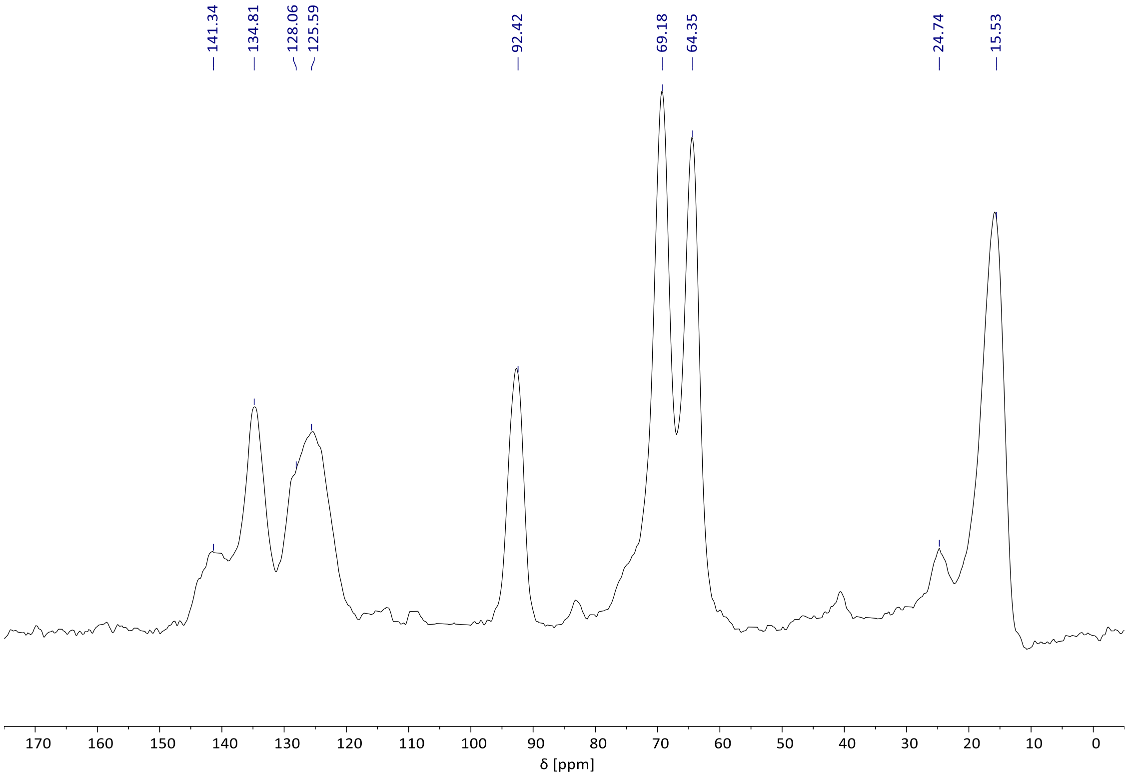

Figure S3: ^{13}C CP-MAS NMR spectrum of P(PTO$_{PrG}$) (100 MHz, 14 kHz, adamantane, 1000 scans).

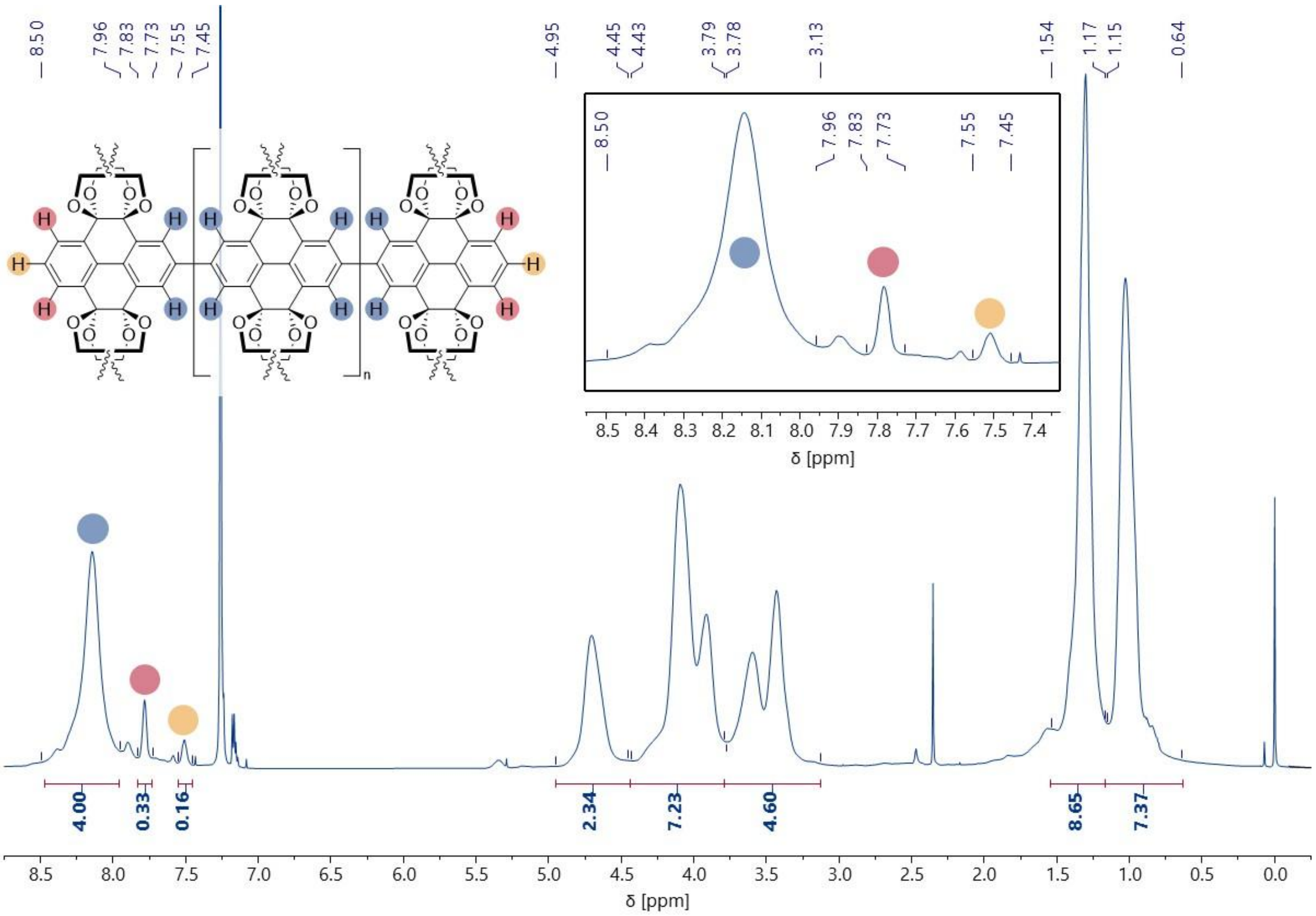

Figure S4: ^{1}H NMR spectrum of P(PTO$_{PrG}$) in CDCl$_3$ (600 MHz). The end-group protons are assigned by colored circles: blue = protons of the chain backbone, red and orange = *meta* and *para* protons of the end-groups.

Poly(pyrene-4,5,9,10-tetraone) (PPTO)

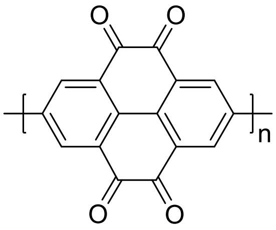

The deprotection of P(PTO$_{PrG}$) to PPTO was done following a modified procedure by XIE *et al*.[7] P(PTO$_{PrG}$) (236.5 mg) was dissolved in a mixture of trifluoroacetic acid / H_2O (9:1, v:v, 17 mL), which had previously been purged with argon.[8] The mixture was heated to 110 °C in a closed vessel for 7 days. After cooling the reaction to room temperature, the suspension was added to cold H_2O (50 mL). The precipitate was separated by centrifugation and purified by multiple washing cycles with a variety of solvents in an ultrasonic bath and subsequent centrifugation (H_2O: 5 × 35 mL; MeOH: 2 × 35 mL, THF: 2 × 35 mL, $CHCl_3$: 2 × 35 mL). The title compound (103 mg, 82%)[9] was obtained as a dark red[10] solid.

^{13}C CP-MAS-NMR (100 MHz, 14 kHz, Adamantane, sample contains traces of incompletely deprotected P(PTO)$_{PrPG}$ with signals at $\delta = 68.44, 25.76$): $\delta = 177.95, 131.59$.

---

[8] It is advised against using steel cannulas to inject the Ar-gas to avoid corrosion of the cannula and ion-contamination of the reaction. A glass pipette or PTFE cannula driven through a septum is the method of choice.

[9] Gravimetric yields of >100% can be achieved, which indicates incomplete deprotection. However, the polymer precipitates as very fine particles, so losses during work-up are close to unavoidable. Thus, yields <100%, like in the run presented here, do not necessarily indicate a complete deprotection.

[10] When dried, it appeared mostly black.

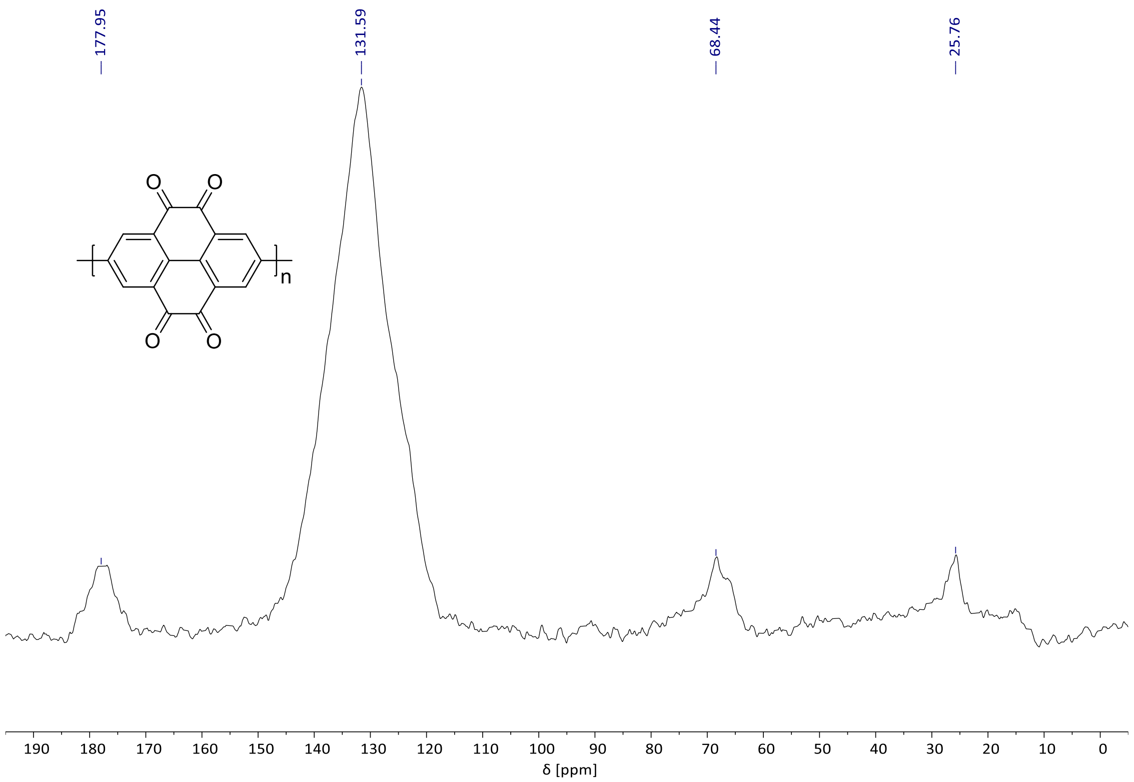

Figure S5: ^{13}C CP-MAS NMR spectrum of PPTO (100 MHz, 14 kHz, adamantane, 6000 scans).

Thermal characterization data of P(PTO)$_{PrPG}$ and PPTO (with Figures S6-S7)

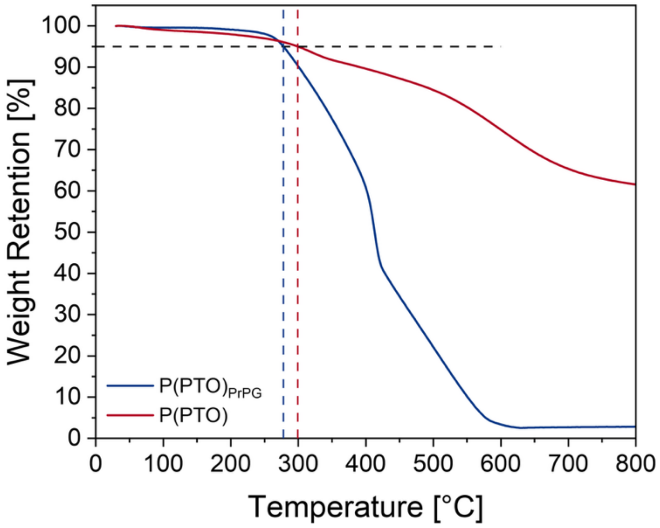

Figure S6: TGA curves of P(PTO$_{PrG}$) and PPTO under N_2-atmosphere. Heating rate = 10 K min^{-1}. Temperatures of 95% weight retention are shown as dashed lines. P(PTO$_{PrG}$) decomposes significantly faster and more completely than PPTO.

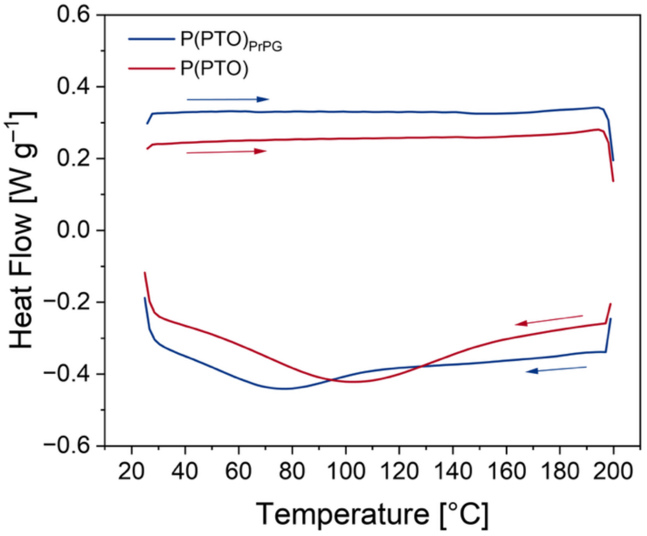

Figure S7: DSC data for P(PTO$_{PrG}$) and PPTO. The respective second heating and cooling processes are shown. Heating and cooling rate = 10 K min^{-1}, dwell time = 30 s. No significant thermal transitions could be observed.

Additional figures and details

Additional Figures S8–S28

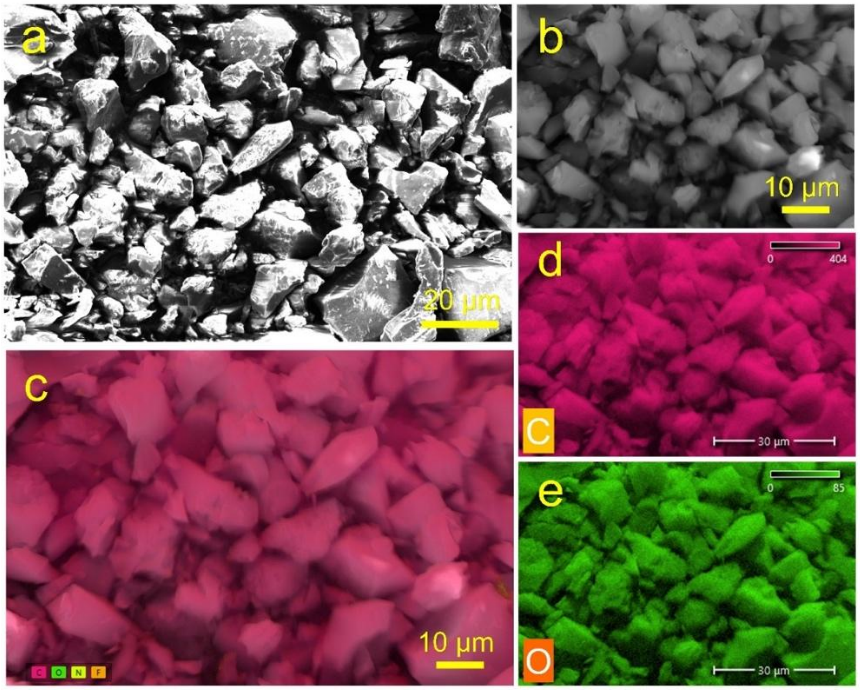

Figure S8. SEM/EDS elemental mapping of pristine PPTO powder. **(a)** SEM image, **(b)** selected area, **(c)** colored image with all elements. **(d)** carbon and **(e)** oxygen.

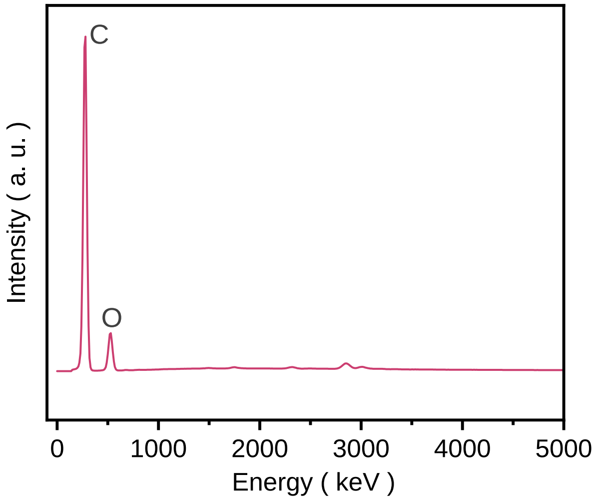

Figure S9. EDS spectrum of the as-prepared PPTO powder.

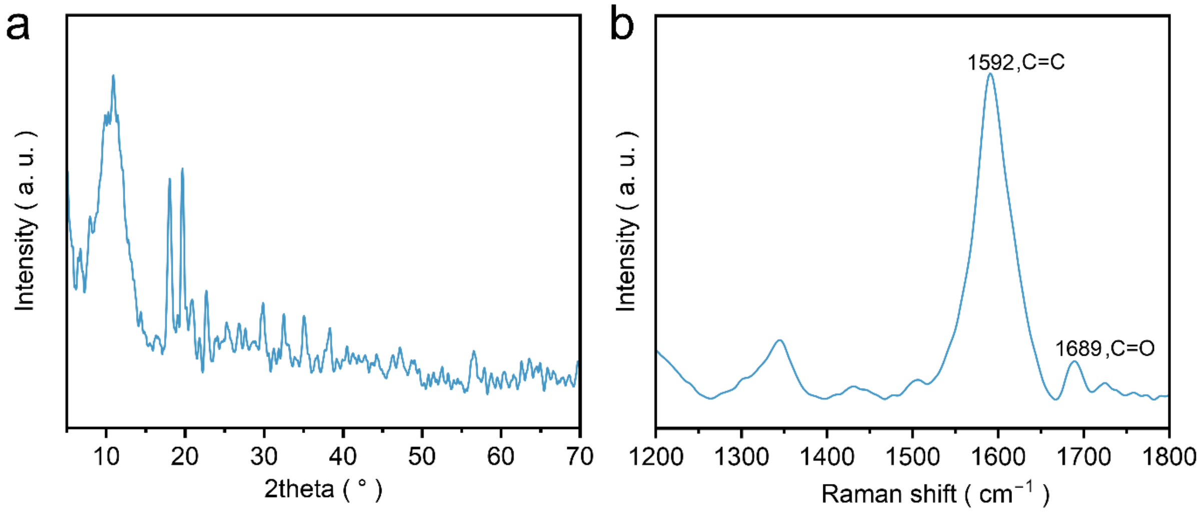

Figure S10. **(a)** XRD pattern and **(b)** Raman spectrum of pristine PPTO powder.

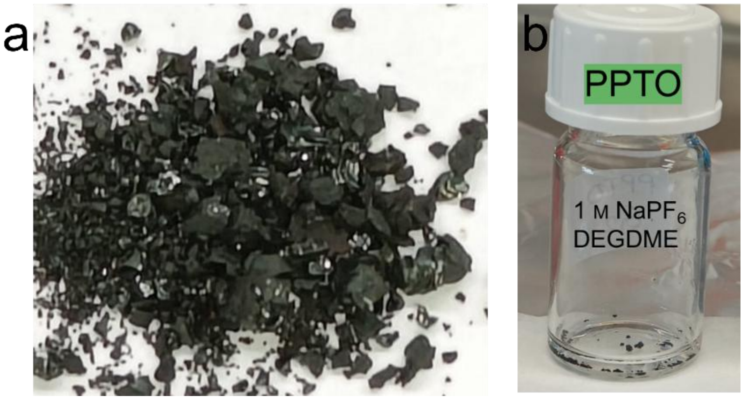

Figure S11. Photographic image of the solubility test of the as-prepared PPTO powder dissolved in 1 M $NaPF_6$ in DEGDME electrolyte under argon atmosphere. (a) PPTO powder and (b) PPTO powder in 1 M $NaPF_6$ in DEGDME electrolyte.

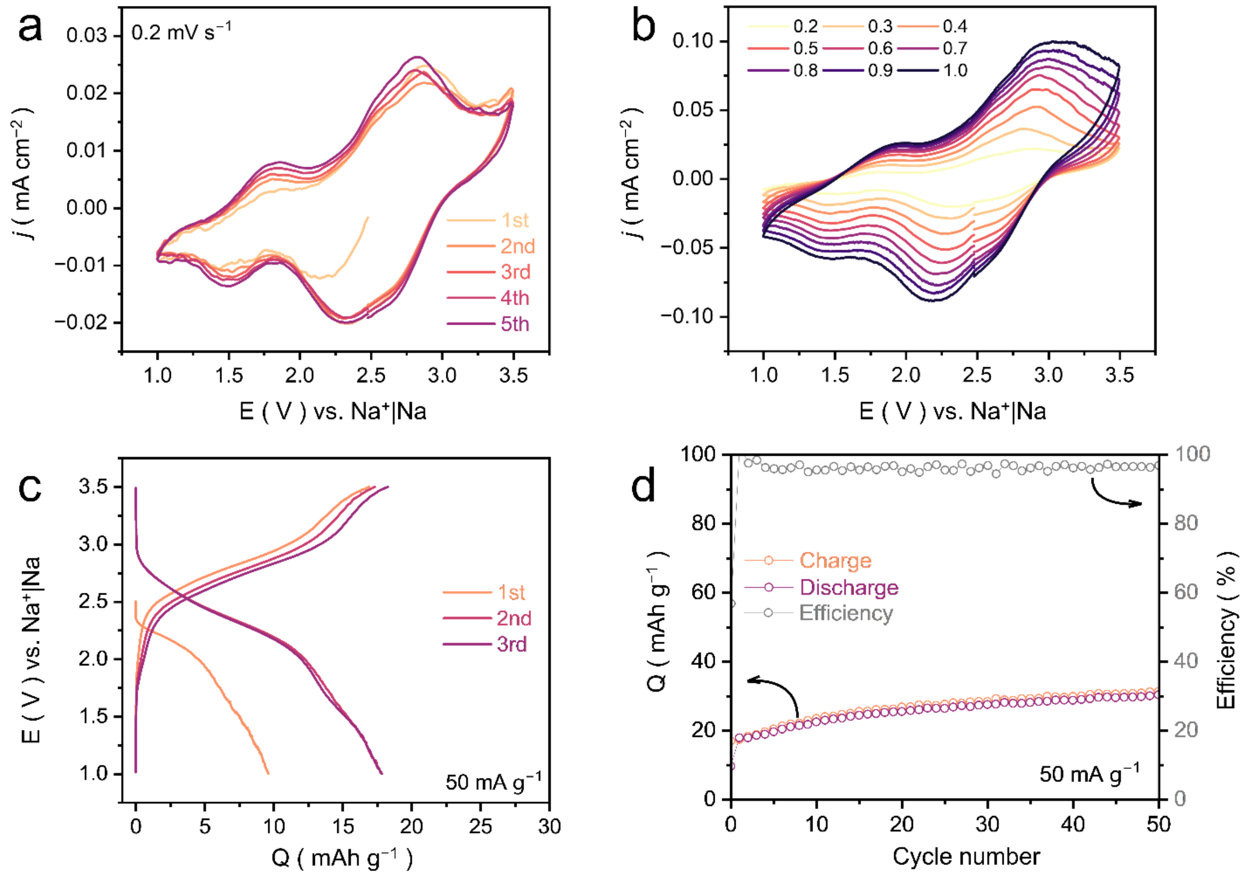

Figure S12. Electrochemical performance of the PPTO@Super P electrode (PPTO: Super P:PVDF 50:40:10 wt%) in 1 M $NaClO_4$ TEGDME electrolyte at room temperature. **(a)** Cyclic voltammograms (CVs) at a scan rate of 0.2 mV s^{-1}. **(b)** CVs at different scan rates. **(c)** Galvanostatic charge/discharge profiles at a current rate of 50 mA g^{-1} and **(d)** the corresponding cycle life.

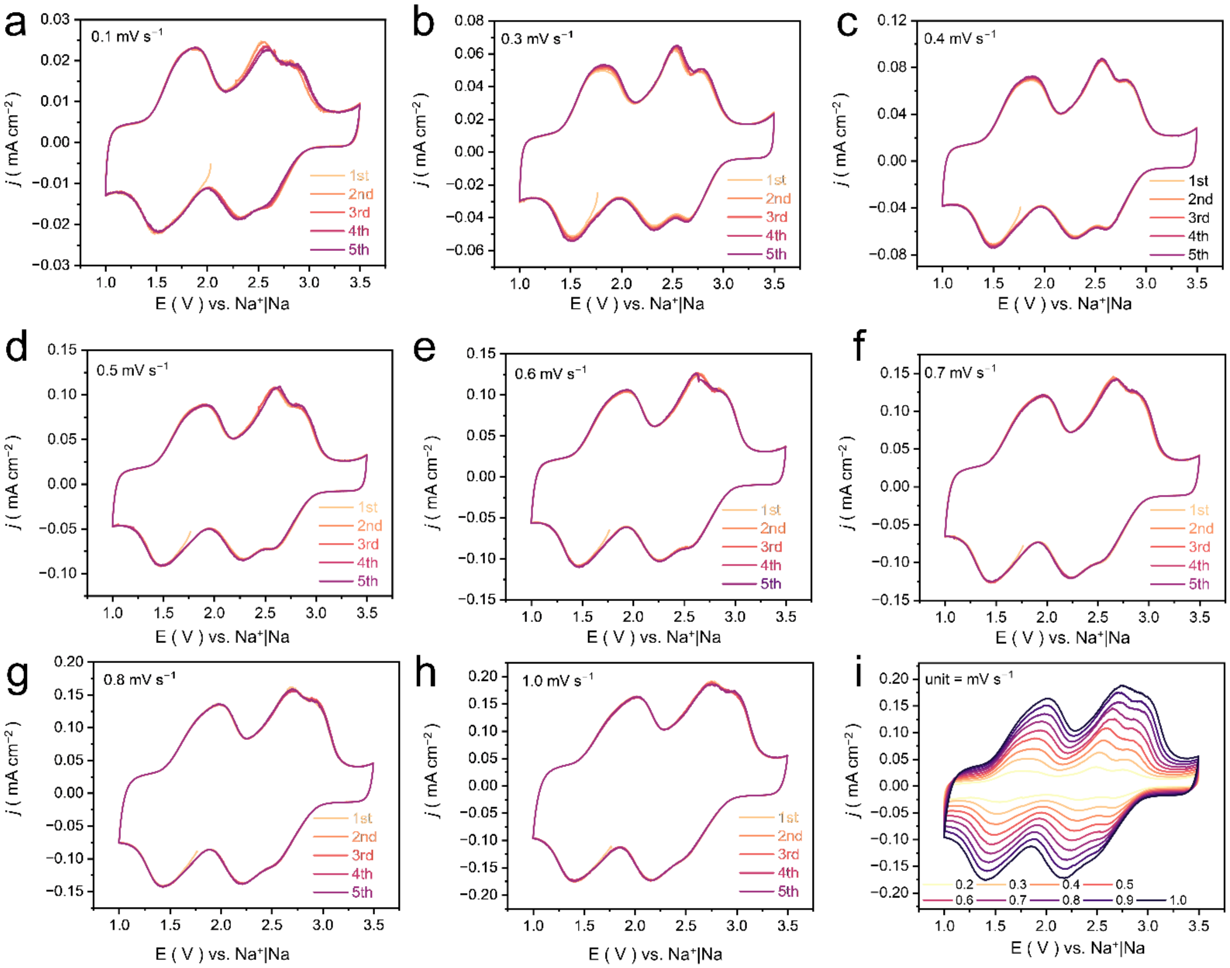

Figure S13. CVs of the PPTO@KB electrode (PPTO:KB600:PVDF 50:40:10 wt%) in 1 M NaClO$_4$ TEGDME electrolyte at room temperature. **(a-h)** CVs at various scan rates and **(i)** combined CVs at different scan rates.

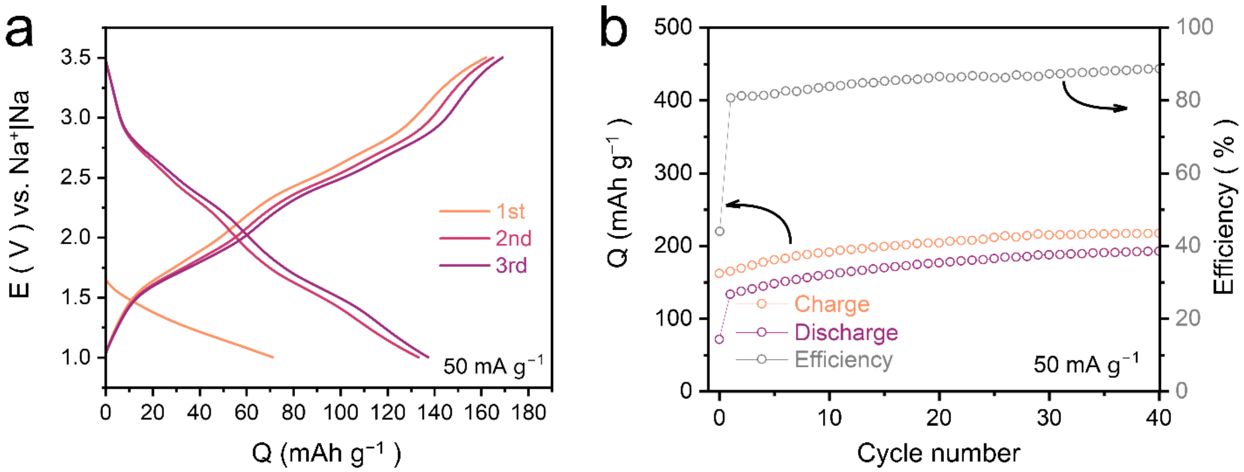

Figure S14. Electrochemical performance of the PPTO@KB electrode (PPTO:KB600:PVDF 50:40:10 wt%) in 1 M $NaClO_4$ TEGDME electrolyte at room temperature. **(a)** Galvanostatic charge/discharge profiles at a current rate of 50 mA g^{-1} and **(b)** the corresponding cycle life.

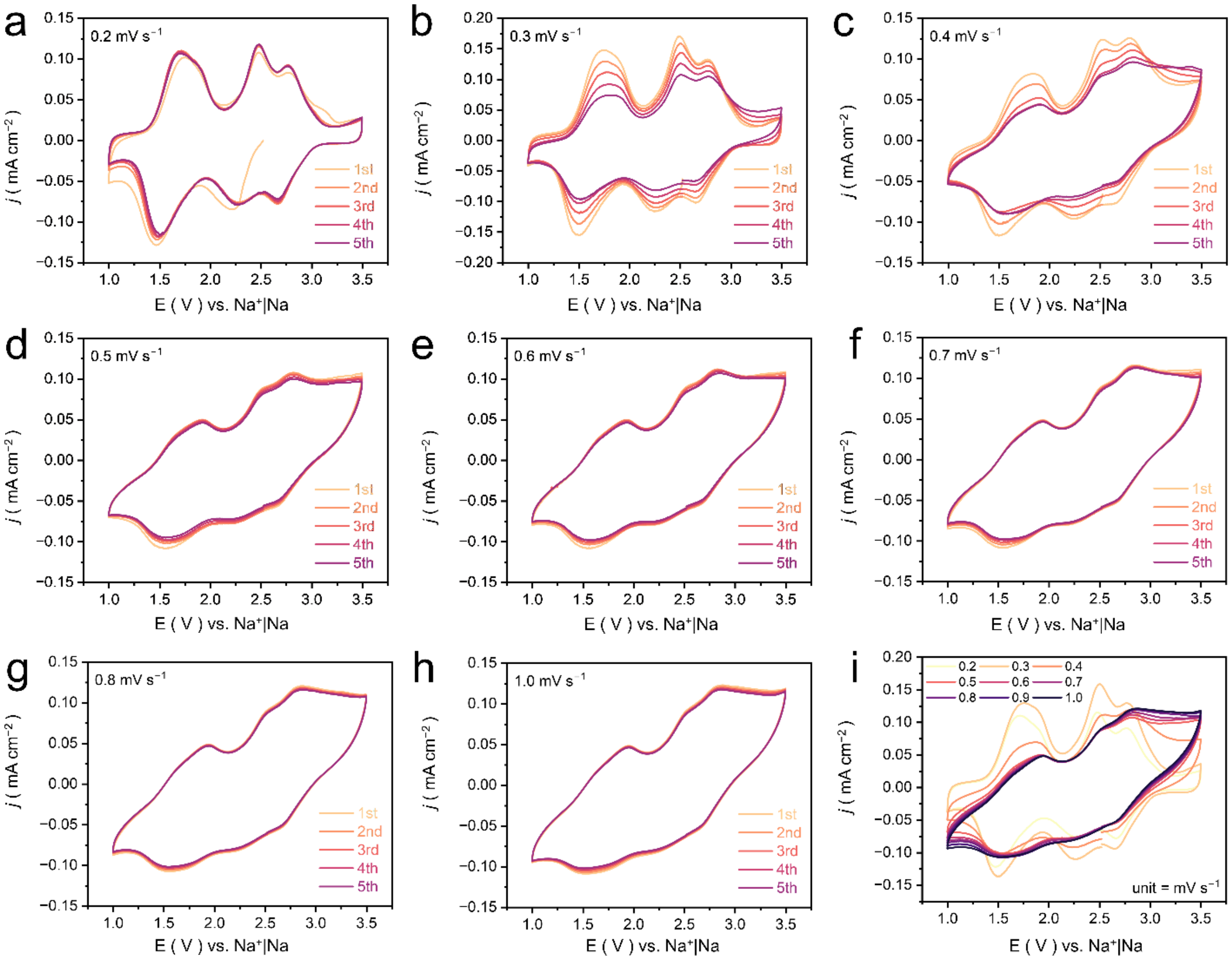

Figure S15. CVs of the PPTO@CNTs@KB electrode (PPTO:SWCNTs:KB600:PVDF 50:20:20:10 wt%) in 1 M $NaClO_4$ TEGDME electrolyte at room temperature. **(a-h)** CVs at various scan rates and **(i)** combined CVs at different scan rates.

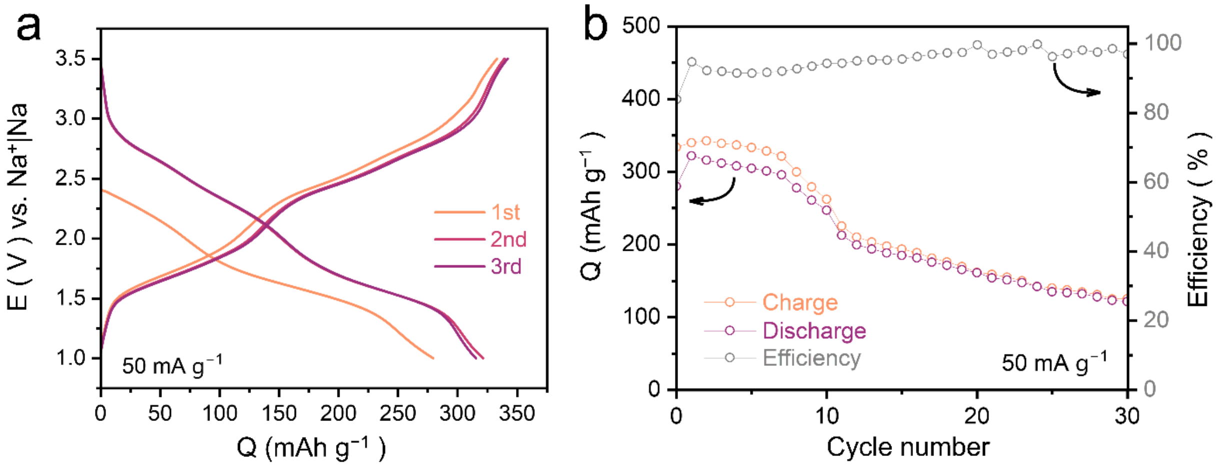

Figure S16. Electrochemical performance of the PPTO@CNTs@KB electrode (PPTO:SWCNTs:KB600:PVDF 50:20:20:10 wt%) in 1 M $NaClO_4$ TEGDME electrolyte at room temperature. **(a)** Galvanostatic charge/discharge profiles at a current rate of 50 mA g^{-1} and **(b)** the corresponding cycle life.

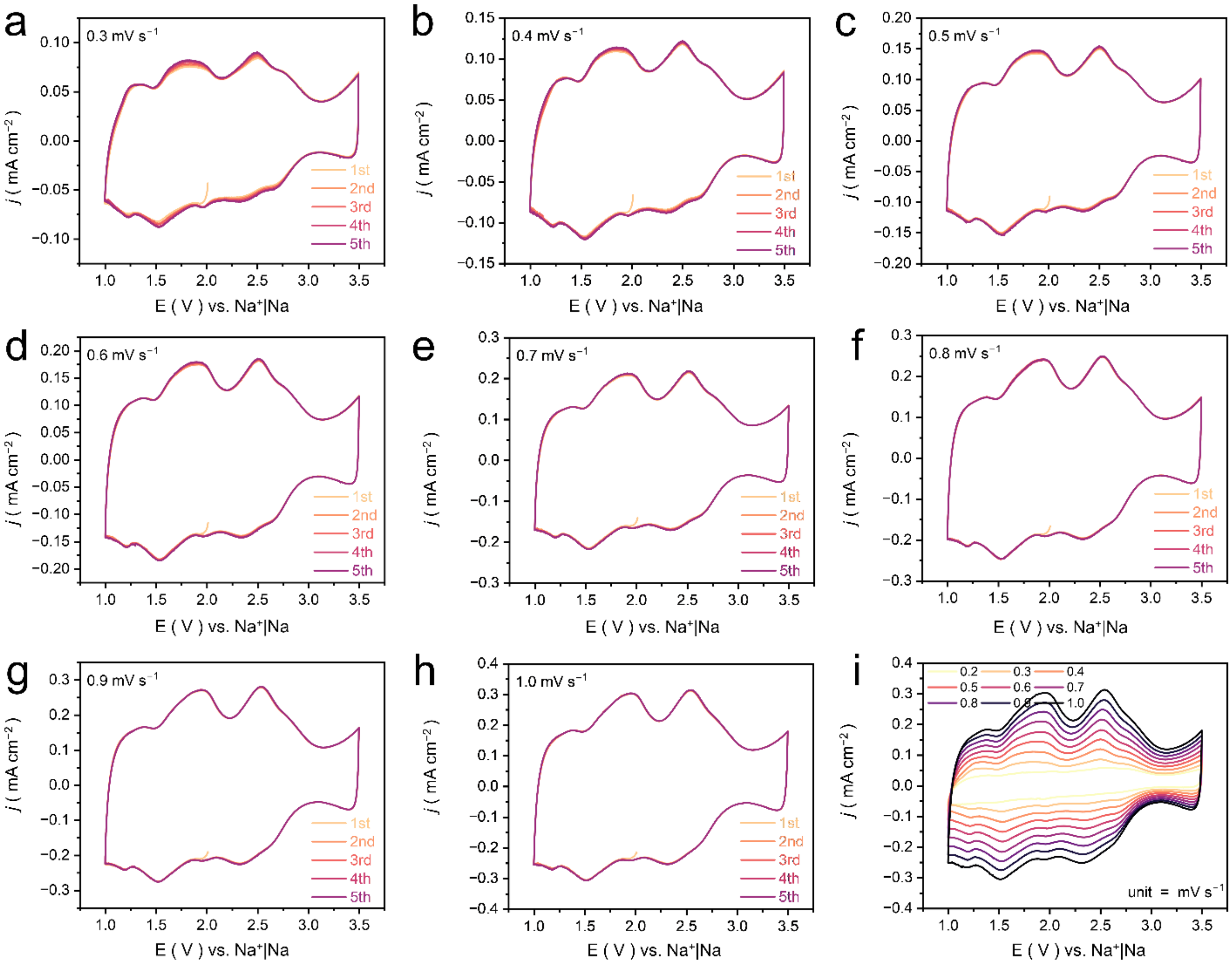

Figure S17. CVs of the PPTO-free-standing electrode (PPTO: SWCNTs 1:2 wt%) in 1 M $NaClO_4$ TEGDME electrolyte at room temperature. **(a-h)** CVs at various scan rates and **(i)** combined CVs at different scan rates.

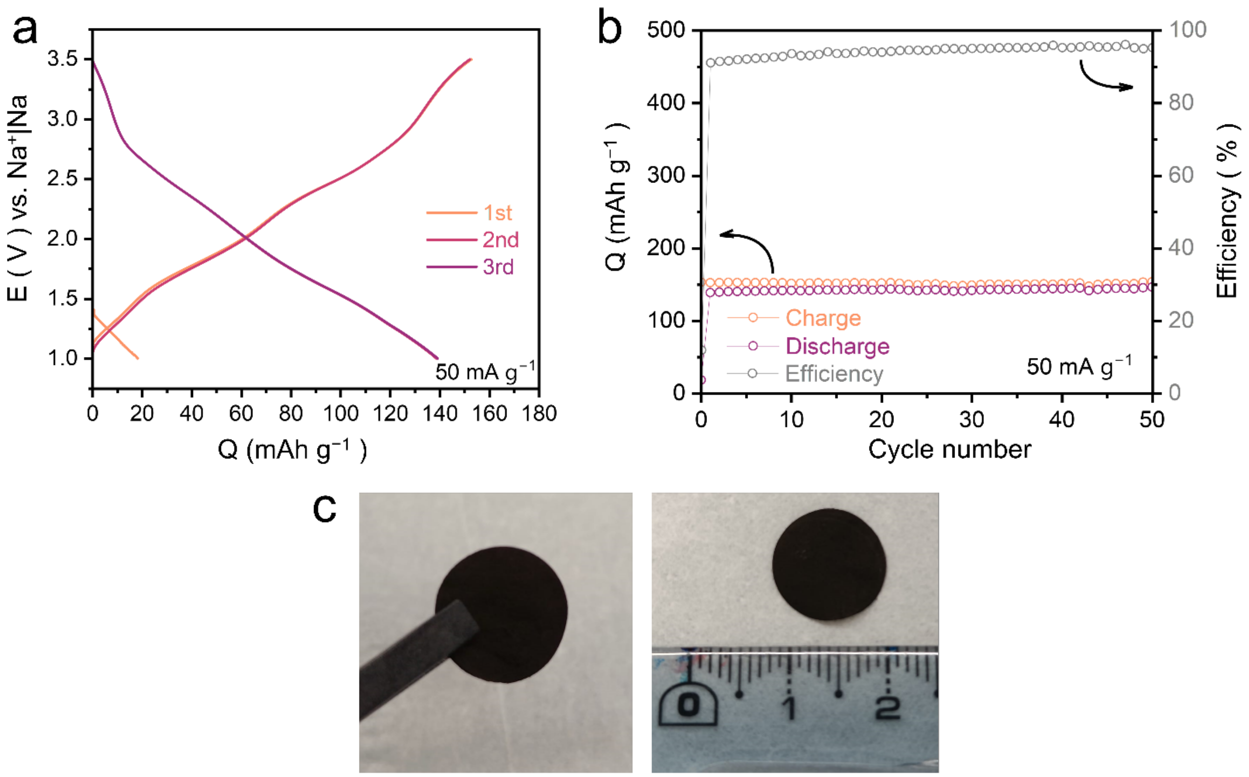

Figure S18. Electrochemical performance of the PPTO-free-standing electrode (PPTO: SWCNTs 1:2 wt%) in 1 M $NaClO_4$ TEGDME electrolyte at room temperature. **(a)** Galvanostatic charge/discharge profiles at a current rate of 50 mA g^{-1} and **(b)** the corresponding cycle life. **(c)** Digital images of the current collector and binder-free PPTO -free-standing electrode.

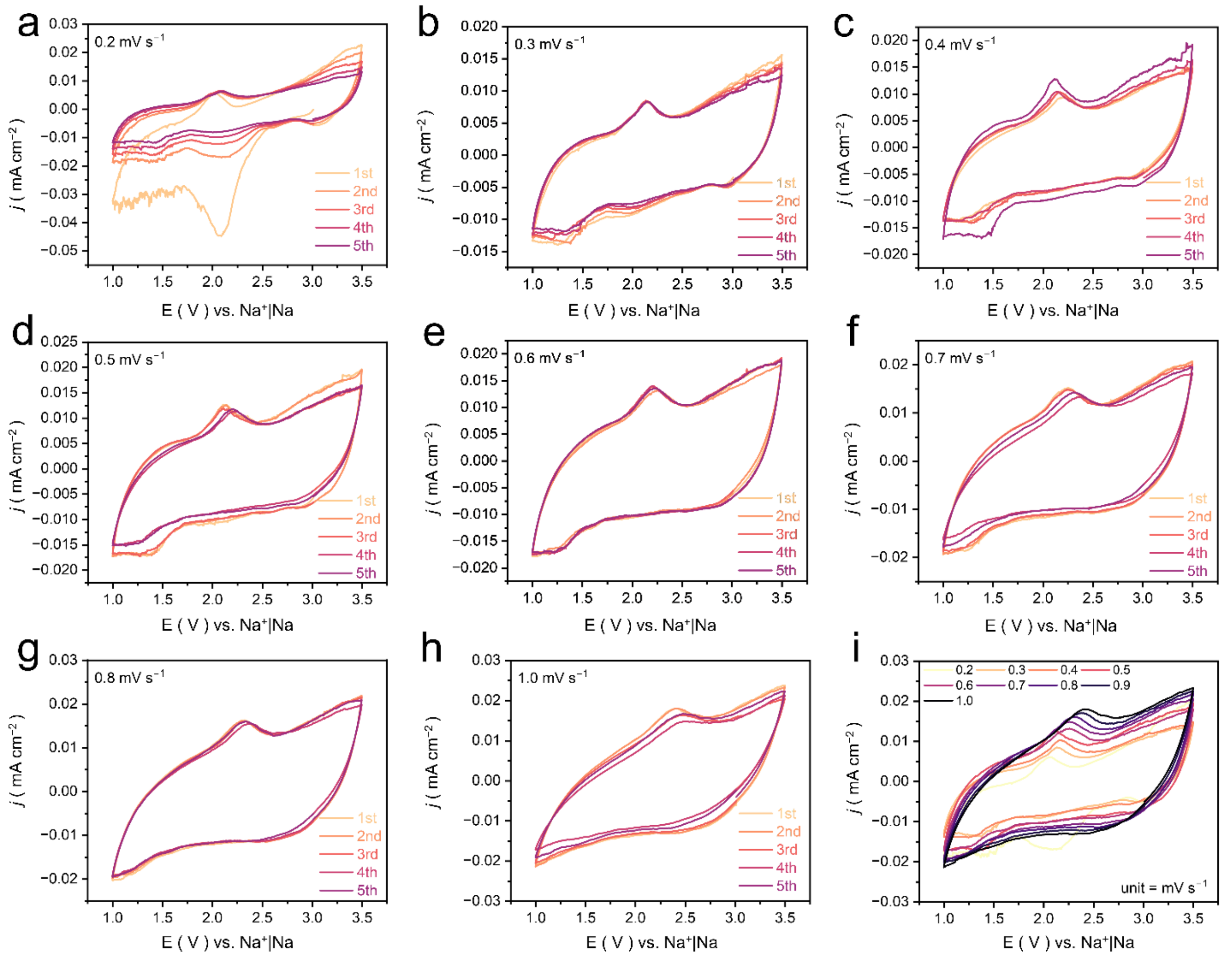

Figure S19. CVs of the PPTO@KB electrode (PPTO:KB600:PVDF 50:40:10 wt%) in 4 M NaPF$_6$ DME electrolyte at room temperature. **(a-h)** CVs at various scan rates and **(i)** combined CVs at different scan rates.

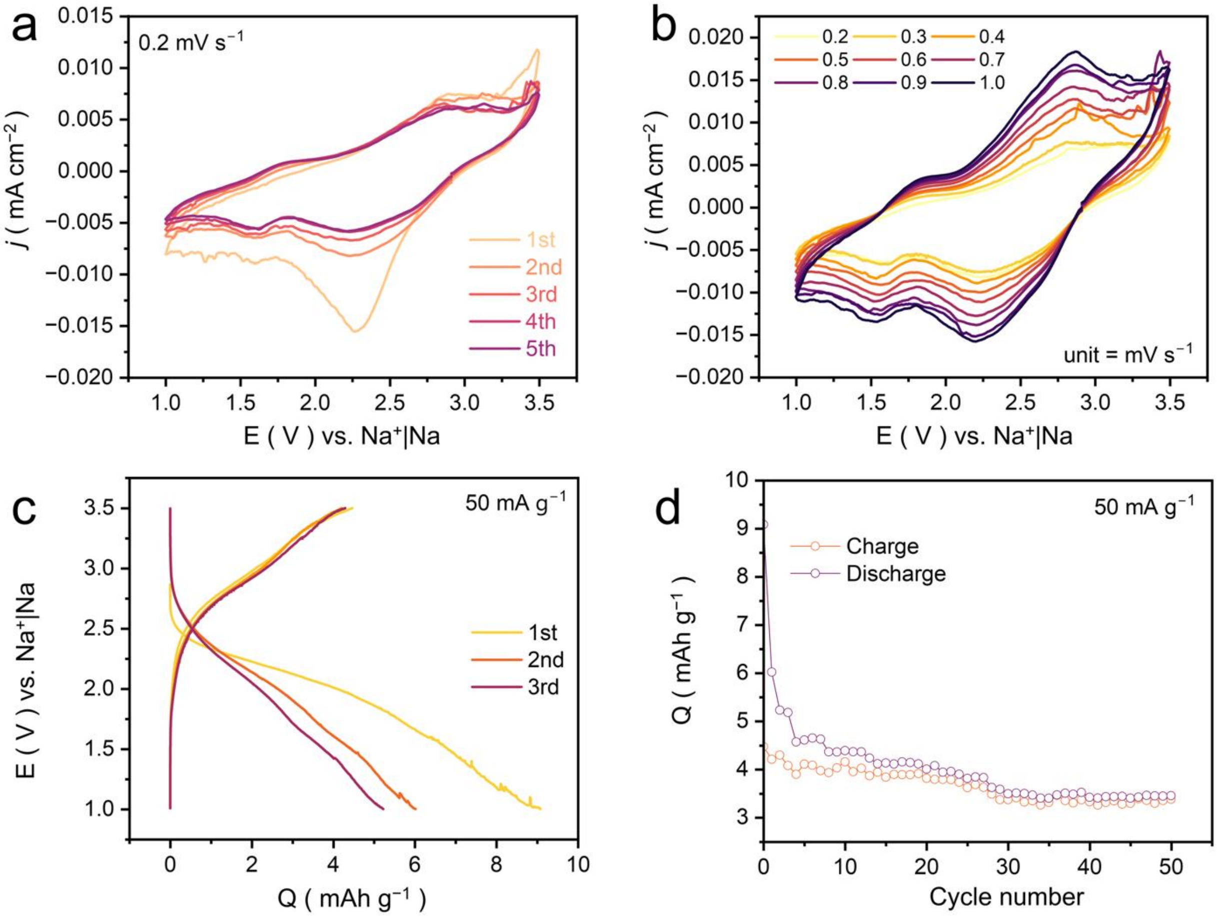

Figure S20. Electrochemical performance of the PPTO@Super P electrode (PPTO:Super P: PVDF 50:40:10 wt%) in 1 M $NaPF_6$ DEGDME electrolyte at room temperature. **(a)** Cyclic voltammograms (CVs) at a scan rate of 0.2 mV s^{-1}. **(b)** CVs at different scan rates. **(c)** Galvanostatic charge/discharge profiles at a current rate of 50 mA g^{-1} and **(d)** the corresponding cycle life.

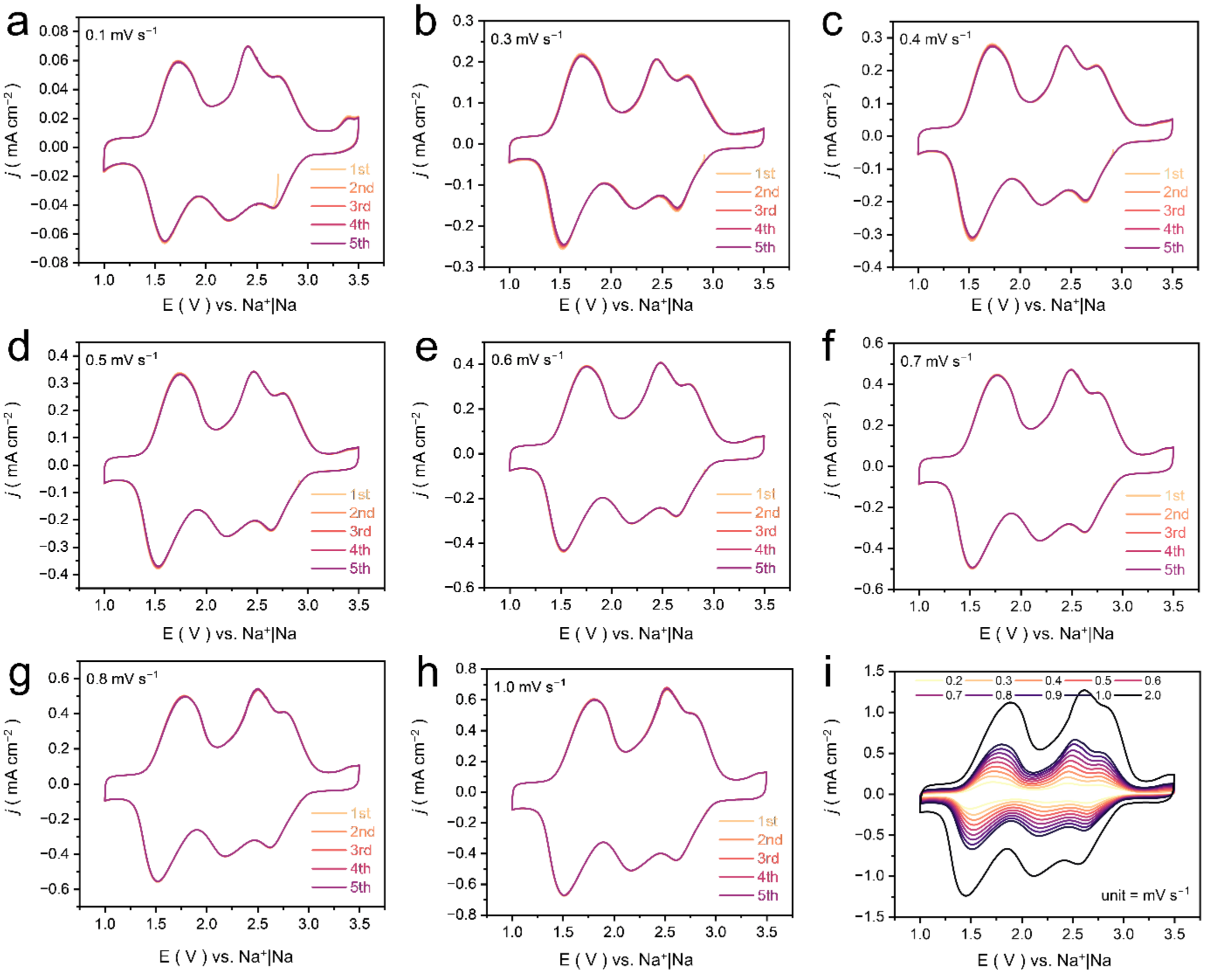

Figure S21. CVs of the PPTO@CNTs@KB electrode (PPTO:SWCNTs:KB600:PVDF 50:20:20:10 wt%) in 1 M $NaPF_6$ in DEGDME electrolyte at room temperature. **(a-h)** CVs at various scan rates and **(i)** combined CVs at different scan rates.

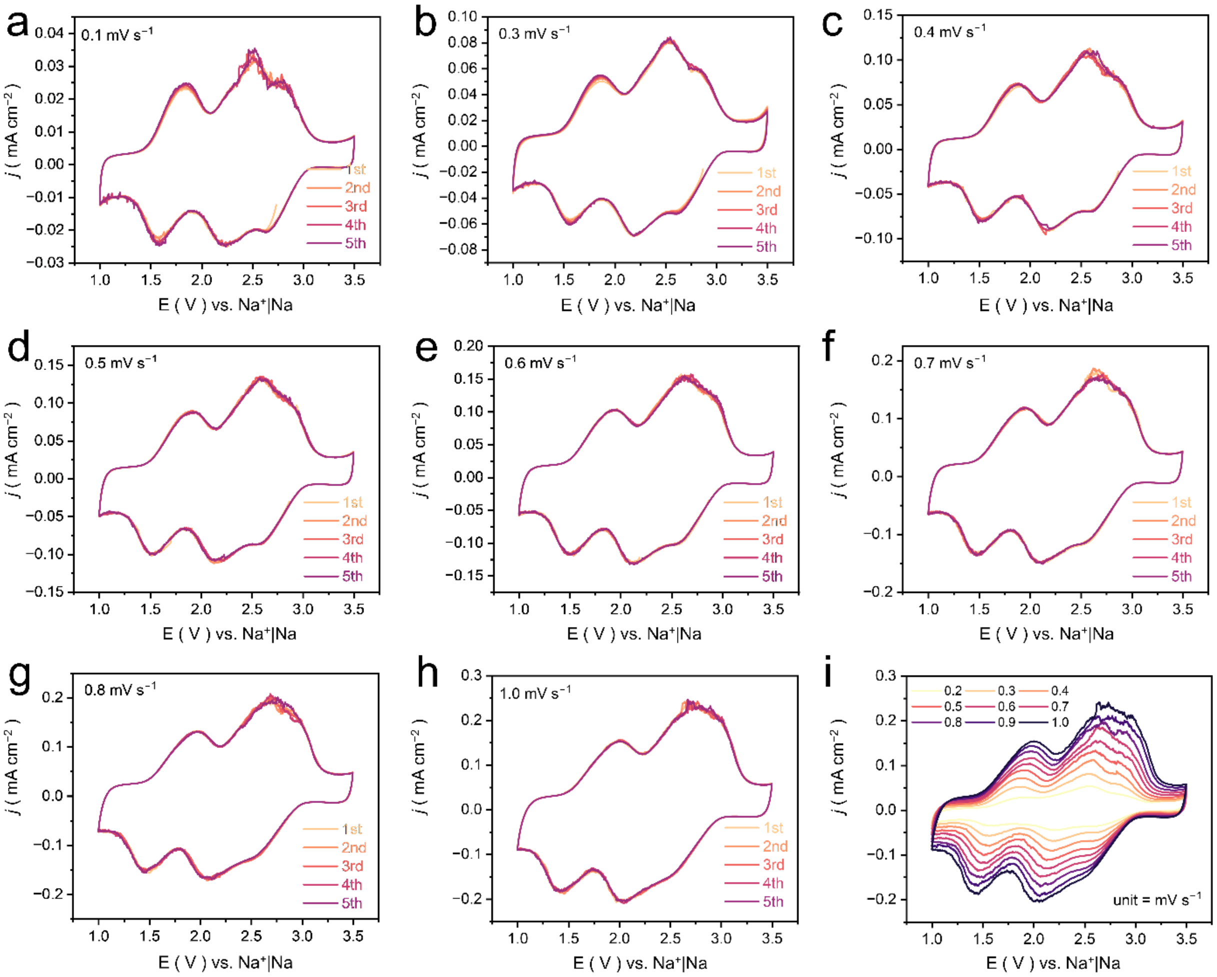

Figure S22. CVs of the PPTO@KB electrode (PPTO:KB600:PVDF 50:40:10 wt%) in 1 M $NaPF_6$ DEGDME electrolyte at room temperature. **(a-h)** CVs at various scan rates and **(i)** combined CVs at different scan rates.

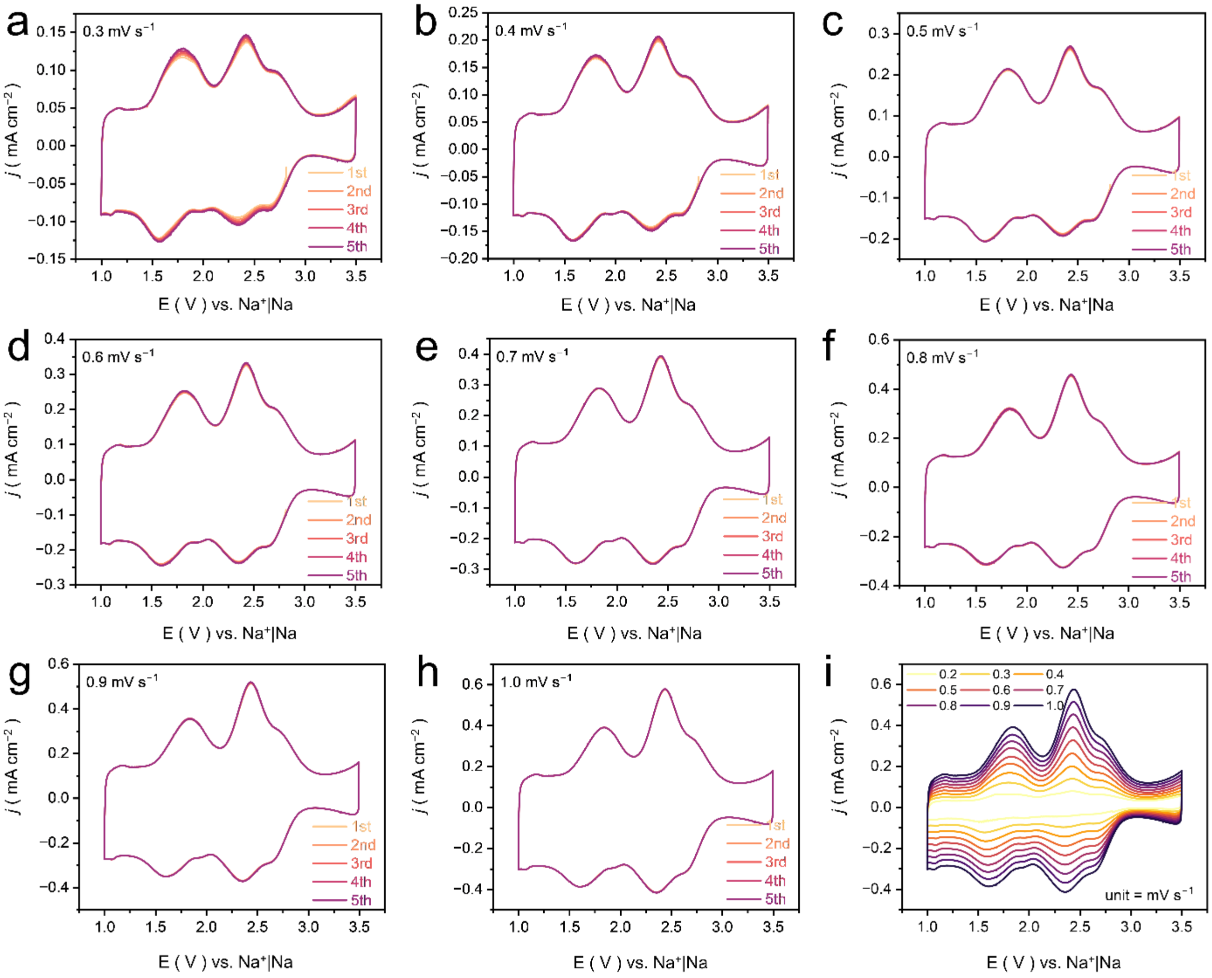

Figure S23. CVs of the PPTO free-standing electrode (PPTO: SWCNTs 1:2 wt%) in 1 M $NaPF_6$ DEGDME electrolyte at room temperature. **(a-h)** CVs at various scan rates and **(i)** combined CVs at different scan rates.

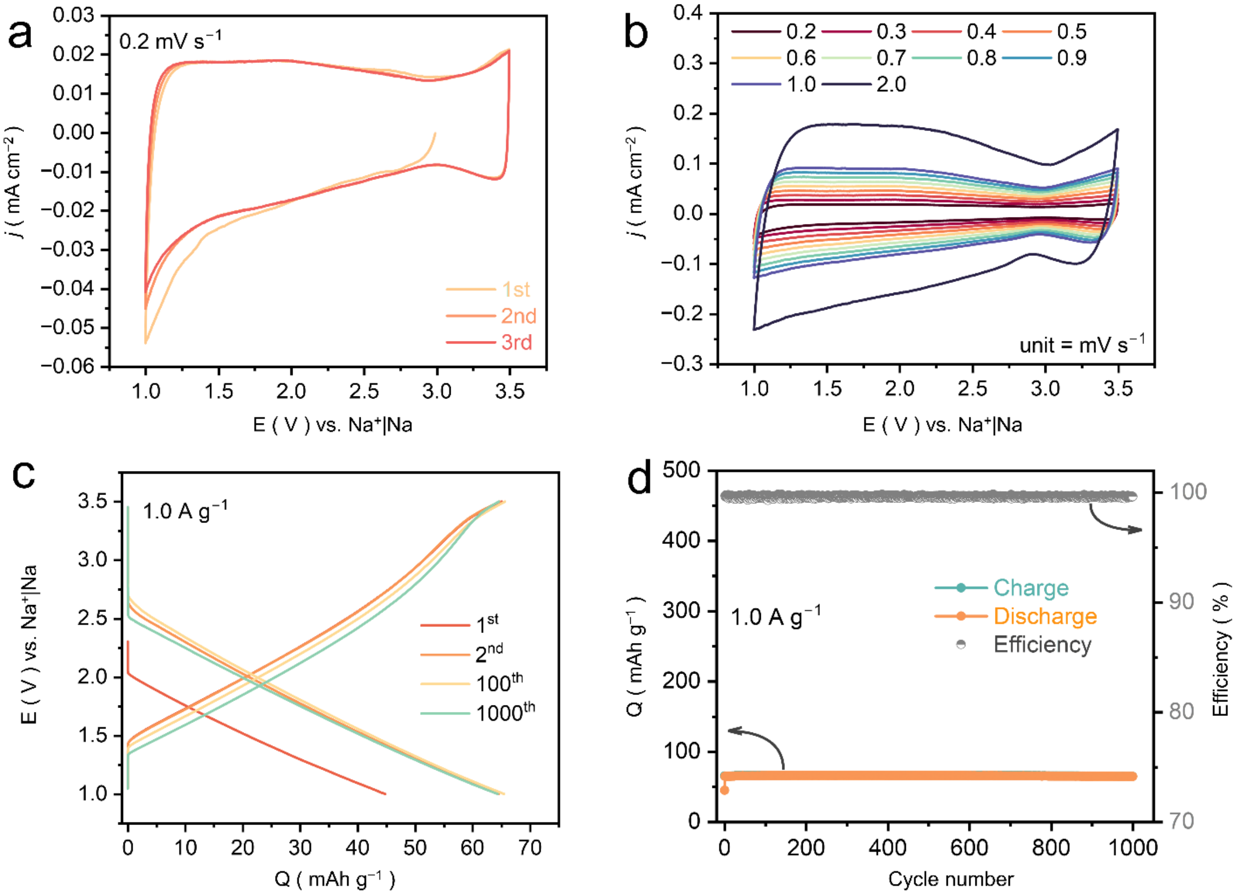

Figure S24. **(a)** Cyclic voltammetry profile of CNTs-KB600 electrode (SWCNTs:KB600:PVDF 40:40:20) at a scan rate of 0.2 mV s^{-1}. **(b)** Combined cyclic voltammetry profile at different scan rates. **(c)** Galvanostatic charge-discharge profile at a current rate of 1.0 A g^{-1} and **(d)** the corresponding cycle life in 1 M $NaPF_6$ DEGDME electrolyte at room temperature.

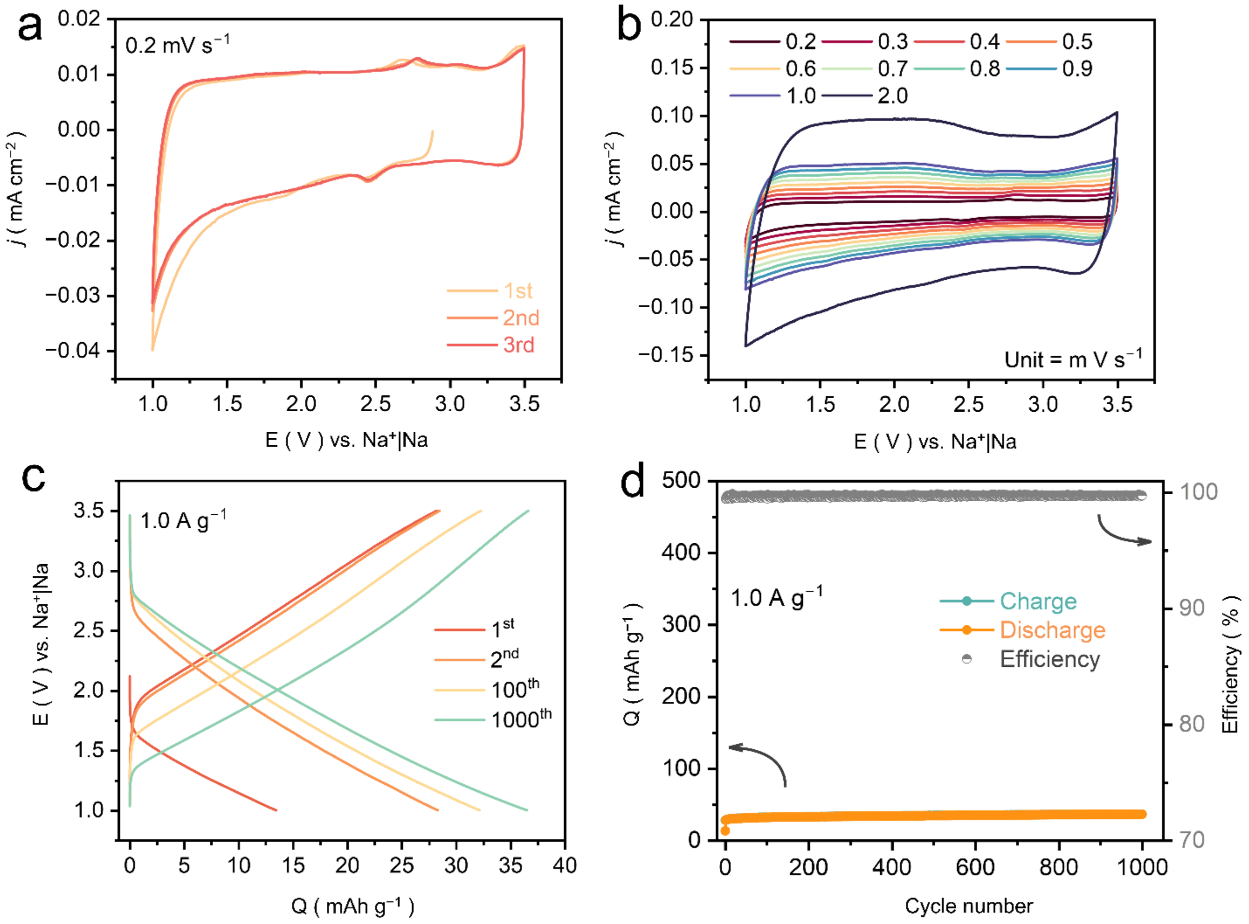

Figure S25. **(a)** Cyclic voltammetry profile of KB600 electrode (KB600:PVDF 80:20) at a scan rate of 0.2 mV s^{-1}. **(b)** Combined cyclic voltammetry profile at different scan rates. **(c)** Galvanostatic charge-discharge profile at a current rate of 1.0 A g^{-1} and **(d)** the corresponding cycle life in 1 M $NaPF_6$ DEGDME electrolyte at room temperature.

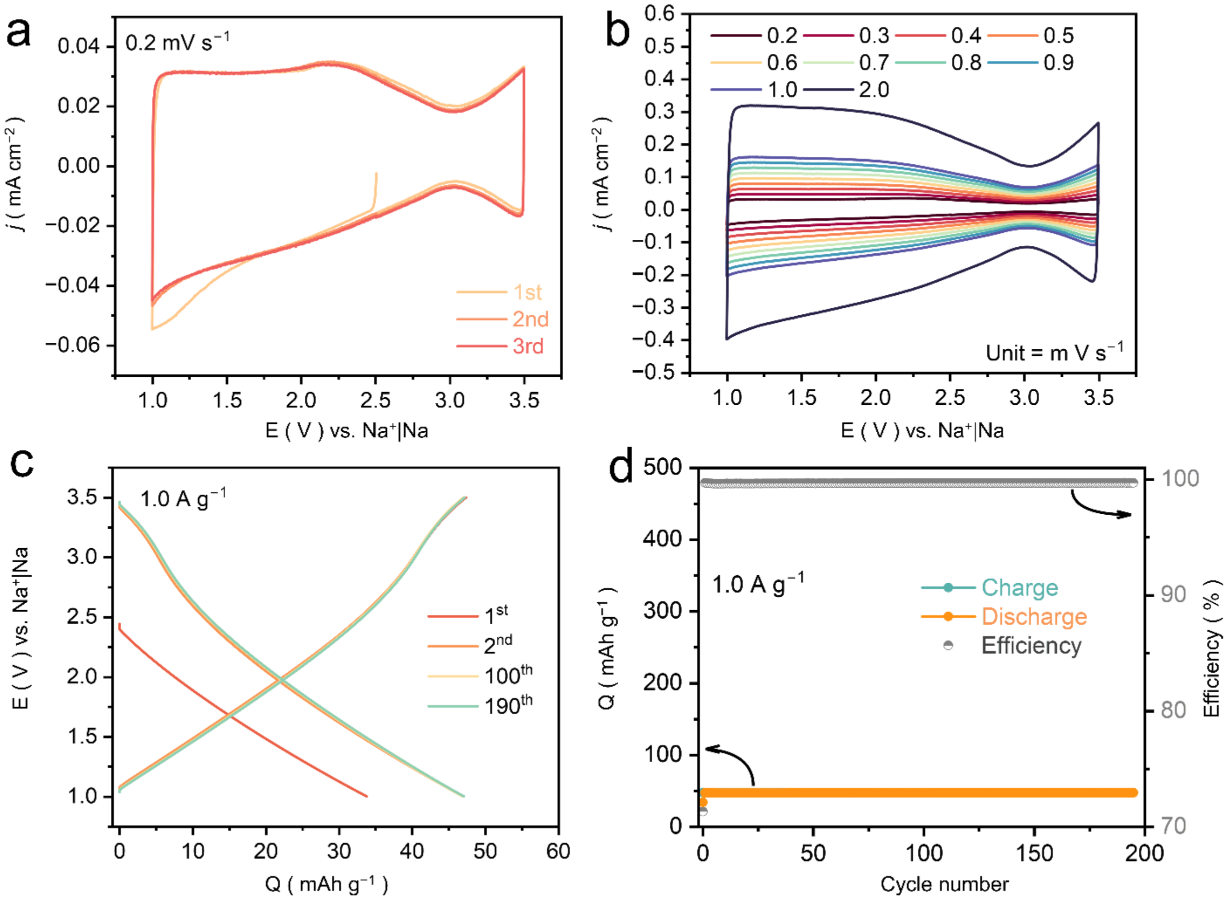

Figure S26. **(a)** Cyclic voltammetry profile of the free-standing binder-free SWCNTs electrode (100 wt% SWCNTs) at a scan rate of 0.2 mV s^{-1}. **(b)** Combined cyclic voltammetry profile at different scan rates. **(c)** Galvanostatic charge-discharge profile at a current rate of 1.0 A g^{-1} and **(d)** the corresponding cycle life in 1 M NaPF$_6$ DEGDME electrolyte at room temperature.

Figure S27. **(a-d)** Photographs of the separators from PPTO@CNTs@KB||Na cells at different states of charge and discharge (showing no sign of dissolution). **(e, f)** Separator and positive electrode from PPTO@KB||Na and PPTO@Super P||Na cells after the first discharge. (**g–i**) Separator and positive electrode from PPTO@CNTs@KB||Na, PPTO@KB||Na and PPTO@Super P||Na cells after long-term cycling (all at 1 A g^{-1} current rate and in 1 M $NaPF_6$ DEGDME electrolyte at room temperature).

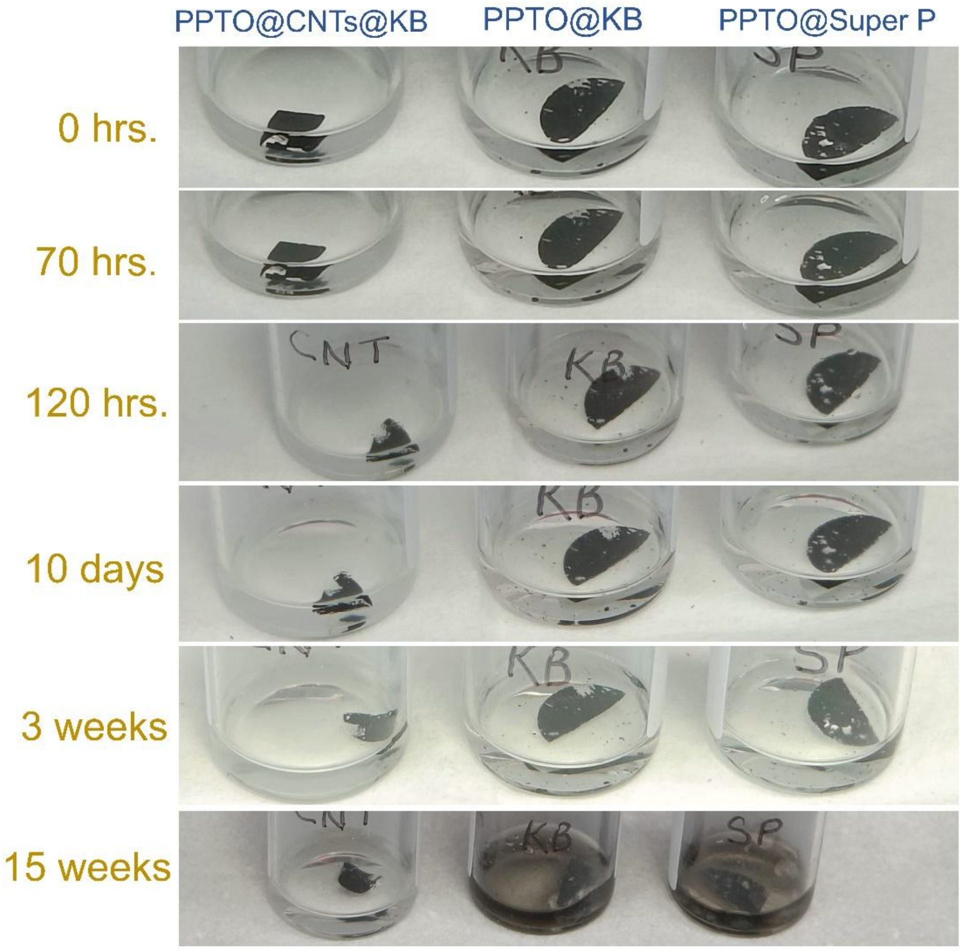

Figure S28. Digital images of discharged electrodes (discharged to 1.0 V at 0.1 A g^{-1}) of PPTO@CNTs@KB (CNT), PPTO@KB (KB), and PPTO@Super P (SP) soaked in 1 M $NaPF_6$ DEGDME electrolyte inside the glovebox.

Time-dependent density functional theory (DFT) calculations (Figure S29)

Time-dependent DFT calculations with a 7.5 dielectric constant (DEGDME) in the continuum solvation model approach (SMD) allow for comparison of the absorption spectra of PTO and PTO-4Na (**Figure S29)**. A significant red shift occurs after reduction. This red shift reflects the reduction of the PTO carbonyls, formation of delocalized enolate structures, and a smaller electronic band gap in the sodium-inserted electrode compared to the pristine PTO powder.

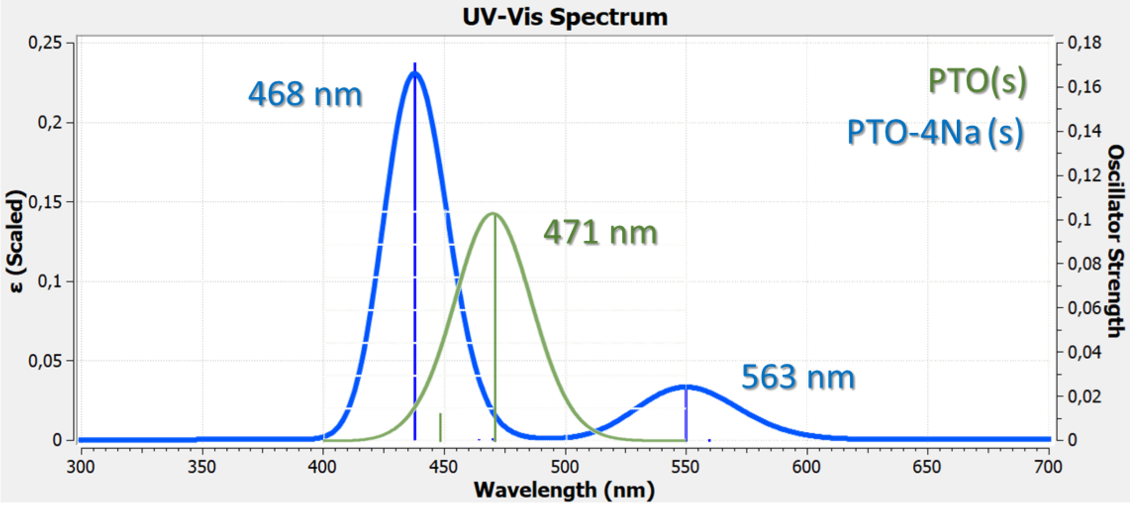

Figure S29. TD-DFT calculated absorption spectra of PTO and PTO-4Na in a simulated DEGDME solvent.

Additional Figure S30

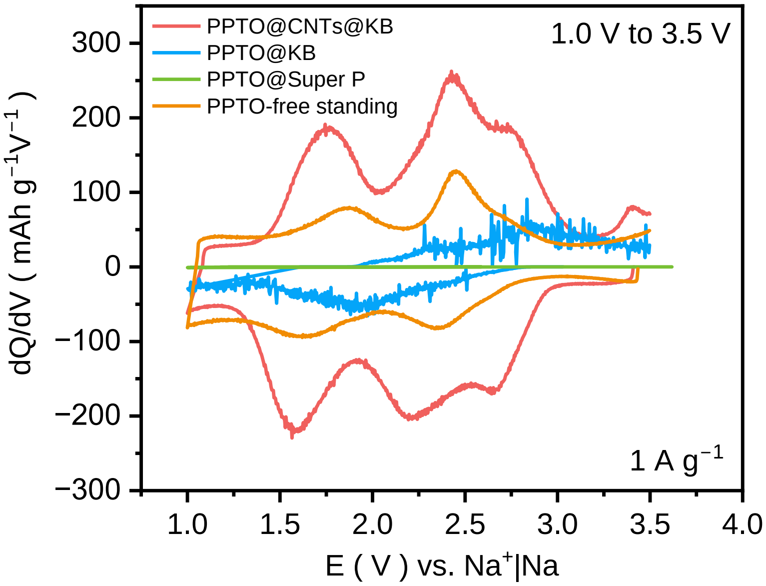

Figure S30. The second cycle differential capacity curves of various PPTO-based electrodes within 1.0 V to 3.5 V at 1 A g^{-1} current rate in 1 M $NaPF_6$ DEGDME electrolyte.

Average cell voltage calculation (Figure S31)

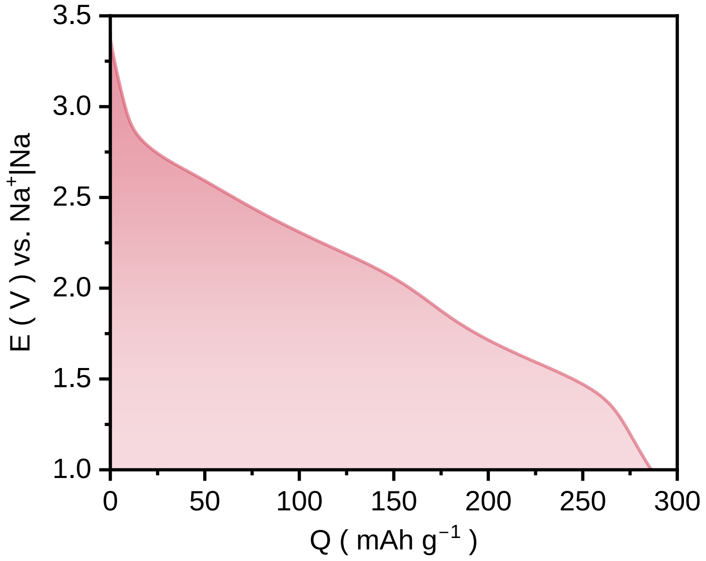

Figure S31. First cycle discharge profile of the PPTO@CNTs@KB cathode at a current rate of 1.0 A g^{-1} in 1 M $NaPF_6$ in DEGDME electrolyte at room temperature.

Calculation of the average cell voltage:

The details of the calculation are given in our previous report[8] and the following paragraph. The first cycle specific discharge capacity of the PPTO@CNTs@KB cathode is calculated from the experimental data, resulting in a value of 286.29 mAh g^{-1}, equivalent to 286.29 Ah kg^{-1}. This value represents the integral of dQ from the initial discharge (Q1) to the final discharge (Q2). The specific energy density (Wh kg^{-1}) is determined by integrating the product of voltage (V) and specific discharge capacity. Graphically, this is represented by the area under the curve of voltage (V) versus specific capacity.

Mathematically, the energy density of the cell can be expressed as:

Energy density (Wh kg^{-1}) = Voltage (V) × Specific capacity (Ah kg^{-1})

Thus, Voltage (V) = $\frac{Energy\ density}{Specific\ capacity}$ S1

$\int_{Q1}^{Q2} dQ$ = specific discharge capacity of the PPTO@CNTs@KB cathode = 286.29 mAh g^{-1}

$\int_{Q1}^{Q2} V\, dQ$ = specific energy density of the PPTO@CNTs@KB cathode = 591.89 Wh kg^{-1} (based on the active material mass of PPTO)

Consequently, the average nominal cell potential (V_{avg}) of the PPTO@CNTs@KB cathode//Na cell = 2.067 V *vs.* $Na^+|Na$.

Additional Figures S32–S35, Table S1

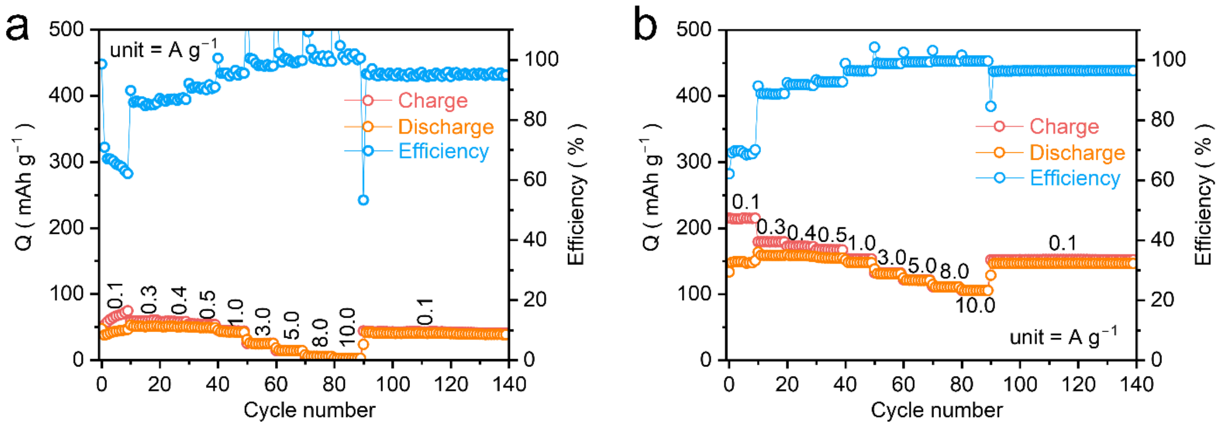

Figure S32. Rate capabilities at different current rates **(a)** PPTO@KB, and **(b)** PPTO-free-standing cathode in 1 M $NaPF_6$ DEGDME electrolyte at room temperature.

Table S1. Conversion of current density to C-rate for PPTO electrode material. The theoretical specific capacity is 412 mAh g^{-1}.

$Q_{theoretical}$ = 412mAh g^{-1} = 0.412Ah g^{-1}

$$\text{C-rate} = \frac{I\ (\text{A/g})}{0.412\ (\text{Ah/g})}$$

Current (A g^{-1})	**C-rate**
0.5	1.21
1.0	2.48

2.0	4.85
3.0	7.28
5.0	12.14
8.0	19.42
10.0	24.27

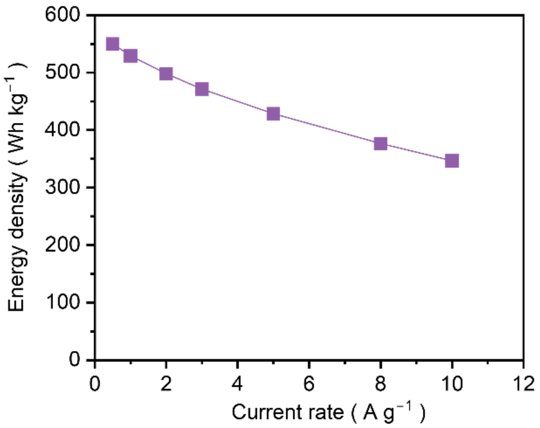

Figure S33. Energy density versus current rate plot for the PPTO@CNTs@KB electrode in a Na half cell (based on the mass of PPTO active material) obtained in the 1 M $NaPF_6$ DEGDME electrolyte at room temperature.

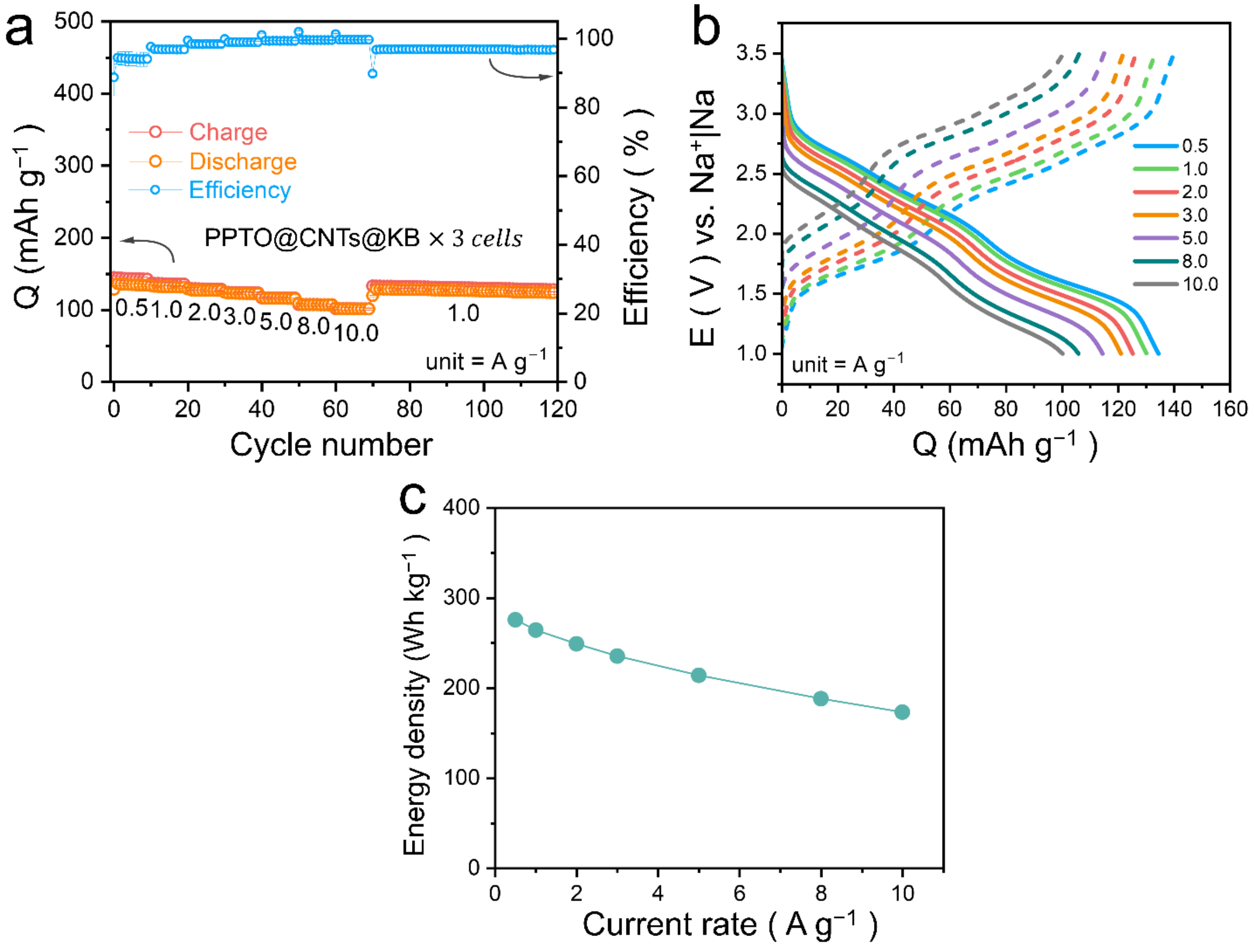

Figure S34. **Electrochemical characterization of PPTO@CNTs@KB electrode based on the total mass of the electrode in a Na half-cell. (a)** Rate performance as an average of three cells data with error bar. **(b)** Galvanostatic charge-discharge curves at various current rates. **(c)** Energy density versus current rate obtained in the 1 M $NaPF_6$ DEGDME electrolyte at room temperature.

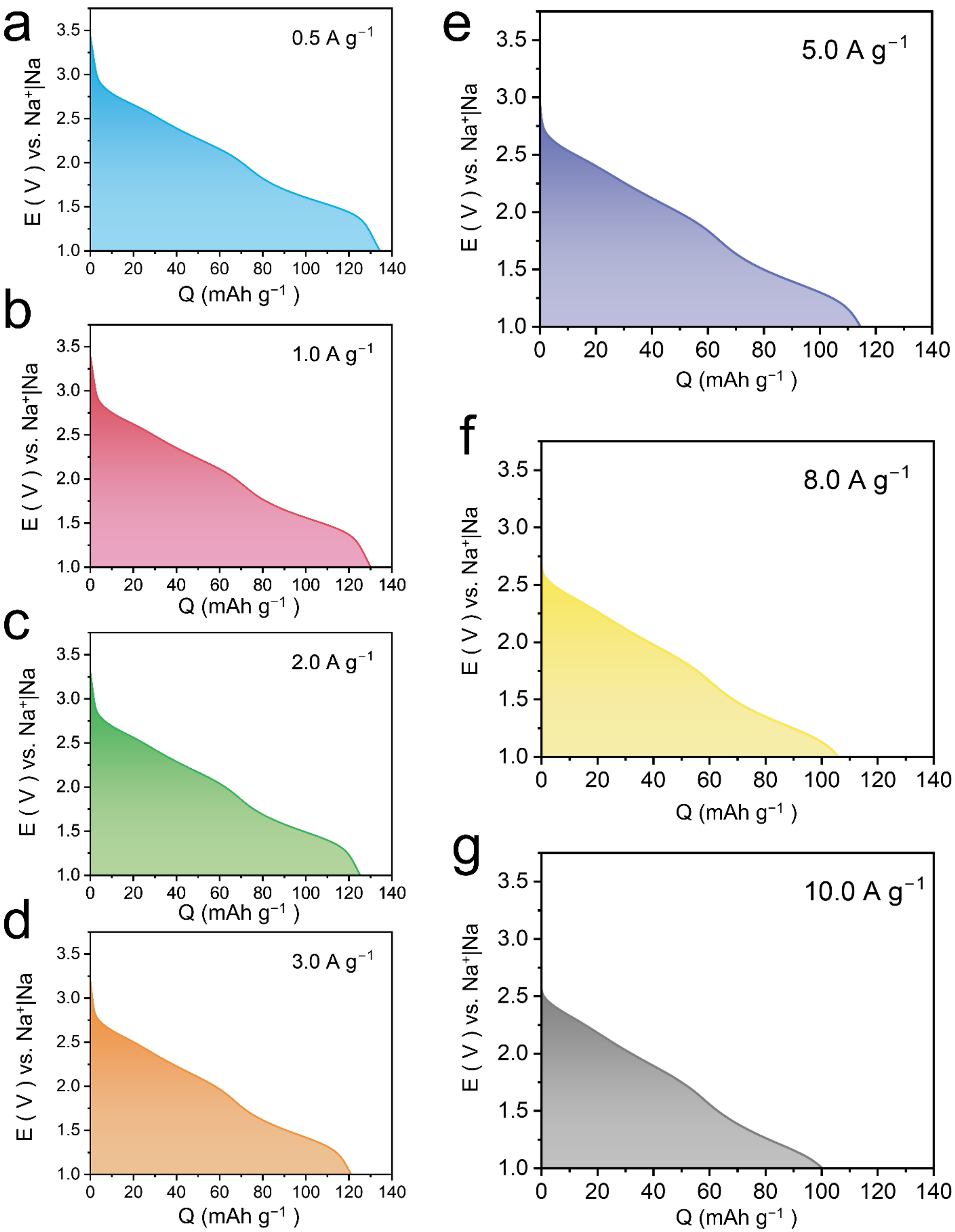

Figure S35. Second cycle discharge profiles of PPTO@CNTs@KB cathode at various current rates (based on the total mass of the electrode) in 1 M $NaPF_6$ DEGDME electrolyte at room temperature.

Energy density calculation

The energy density of the cell, based on the total electrode mass, was calculated as follows:

Generally, the specific energy density can be reckoned by multiplying the maximum specific capacity of the battery for the mid-point voltage (i.e., the voltage at which the cell is discharged to 50% of its specific capacity).

Mathematically, the energy density of the cell can be expressed as:

Energy density (Wh kg^{-1}) = Voltage (V) × Specific capacity (Ah kg^{-1})

Graphically, it is the area under the curve of voltage versus specific capacity as shown in **Figure S35.**

For example, the calculation of energy density at a current rate of 0.5 A g^{-1} is given below.

$\int_{Q1}^{Q2} dQ$ = specific discharge capacity of the PPTO@CNTs@KB cathode based on the total electrode mass = 134.53 mAh g^{-1}

Thus, integrating the voltage versus specific capacity curve yields an energy density value.

$\int_{Q1}^{Q2} V\, dQ$ = specific energy density of the PPTO@CNTs@KB cathode = 275.81 Wh kg^{-1} (based on the total mass of the electrode)

Literature comparison (Table S2)

Table S2: Comparison of the electrochemical performance of PPTO electrodes with those of previously reported organic positive electrodes for Na-ion batteries.

Organic compound	Voltage window (V)	Electrolyte	Electrode composition (active material: carbon: binder)	Capacity (mAh g^{-1})/current density (mA g^{-1}/C) /cycle number/retention (%)	Ref.
PPTO	1.0−3.5	1 M $NaPF_6$ DEGDME	50:20:20:10	286/1000/500/72	This work
PPTO	1.0−3.5	1 M $NaPF_6$ DEGDME	50:40:10 and 60:30:10	194.5/10000/1300/95	[9]
PPTS	0.8−3.2	1 M $NaPF_6$ DME	40:50:10	290/100/100/74	[10]
PTCDA	1.9−3.0	1 M $NaPF_6$ DEGDME	70:20:10	115/5C/500/79	[11]
TDT	1.0−3.5	1 M $NaPF_6$ DEGDME	70:20:10	250/3000/3500/73	[12]
PBQ	1.2−3.4	1 M $NaPF_6$ DEGDME	50:30:20	242/1000/400/91	[13]
PTPAn	2.0−4.0	1 M $NaClO_4$ EC/DMC	60:30:10	92/400/500/81	[14]
PDPPD	3.5−3.7	0.5 M $NaPF_6$ EC/PC	50:40:10	94/1C/500/76	[15]
PDA	1.3−4.2	1 M $NaClO_4$ EC/DMC	80:10:20	228/250/100/62	[16]

PBAQ	0.9−2.3	Saturated $NaPF_6$ in DME/DOL	60:30:10	200/50/1000/96	[17]
PHATN	1.0−3.5	4 M $NaPF_6$ DME	60:30:10	165/2000/10000/89	[18]
p-$Na_2C_6H_2O_6$	1.0−3.0	1 M $NaClO_4$ EC/DMC/FEC	50:40:10	121/0.1C/50/67	[19]
BAQB	1.2−3.4	4 M $NaPF_6$ DME	60:30:10	217/200/1100/73	[20]
PAQS	1.0−3.0	1 M NaTFSI DOL/DME	60:30:10	175/100/100/95	[21]
CP-PDAB	1.1−2.4	1 M NaOTf DEGDME	70:20:10	141/500/100/NA	[22]
PPQ	1.0−3.5	1 M $NaPF_6$ DME	60:20:10:10	90/800/700/93	[23]
PAQS	1.2−2.6	7.6 M $NaI.3.3NH_3$	60:30:10	220/5C/150/60	[24]
Ti−PTCD	1.0−3.0	1 M $NaClO_4$ PC	70:15:15	100/18C/500/89	[25]
PI	1.5−3.5	1 M $NaPF_6$ EC/DMC	60:30:10	207/200/100/43	[26]
DHAQNa/G	1.0−4.0	1 M $NaClO_4$ EC/DMC	25:65:10	176/0.1C/100/86	[27]
TAPT−NTCDA@CNT	1.0−3.5	1 M $NaPF_6$ EC/DMC	80:10:10	91/30/200/77	[28]
p−DNB	1.0−3.7	1 M NaTFSI DOL/DME	70:20:10	590/50/50/50	[29]

P−PANI	2.5−4.2	1 M $NaClO_4$ EC/DEC/FEC	70:20:10	210/200/200/68	[30]
PQPZ	1.0−4.0	1 M $NaPF_6$ DEGDME	60:30:10	270/0.5C/300/90	[31]
PAQS2	1.0−3.0	1 M $NaClO_4$ TEGDME	60:30:10	271/50/200/46	[32]
Na_2BNDI	1.3−3.3	1 M $NaClO_4$ DEGDME	60:30:10	100/1C/300/95	[33]
PTCDI−DAQ	1.0−3.5	4 M $NaPF_6$ DME	60:30:10	203/100/2000/75	[34]
HOF−DAT	1.2−3.0	0.5 M $NaPF_6$ DOL/DME	60:30:10	126/200/2000/83	[35]
PI@NC	1.5−3.5	1 M $NaPF_6$ EC/DMC/FEC	80:10:10	126/100/200/100	[36]
NDI−TFP	1.3−3.3	1 M $NaClO_4$ EC/DMC	30:40:20:10	92/20/100/89	[37]
PI	1.5−3.5	1 M $NaPF_6$ PC	60:30:10	126/100/50/90	[38]
PAQS	1.2−2.8	1 M $NaPF_6$ DOL/DME	40:50:10	185/8C/200/99	[39]

Acronyms of the above table

PPTO – Poly(pyrene-4,5,9,10-tetraone); PPTS − Poly(pentacenetetrone sulfide); PTCDA − perylene- 3,4,9,10-tetracarboxylic dianhydride; TDT − 2,3,7,8-tetraamino-5,10-dihydrophenazine-1,4,6,9-tetraone; PBQ − Poly(tetraminobenzoquinone-alt-2,5-dihydroxy-1,4- benzoquinone); PTPAn – Polytriphenylamine; PDPP − poly(N,N0-diphenyl-p-phenylenediamine); PDA –

Polydopamine; PBAQ – Anthraquinone-based polymer; PHATN − Poly(hexaazatrinaphthalene); *p*-$Na_2C_6H_2O_6$ − Para-disodium-2,5-dihydroxy-1,4-benzoquinone; BAQB − 1,4-bis(9,10-anthraquinonyl)benzene; CP−PDAB − polyimide poly(2,6-diaminoanthraquinone) benzamide; PPQ − Poly(9,10-phenanthraquinone-alt-benzene); Ti−PTCD – Titanium oxide coated perylene-3,4,9,10-tetracarboxylicacid dianhydride; DHAQNa/G − 1,5-dihydroxy anthraquinone sodium salt with graphene; TAPT−NTCDA@CNT − 4,40,40'- (1,3,5-triazine-2,4,6-triyl)trianiline (TAPT) and 1,4,5,8-naphthalenetetracarboxylic dianhydride (NTCDA) and multiwalled carbon nanotube; *p*−DNB – para-dinitrobenzene; P−PANI − Protonated polyaniline; PQPZ − 9,10-phenanthraquinone and dihydrophenazine; PAQS2 − poly (1,5-anthraquinonyl sulfide); Na_2BNDI − N, N′-bis(glycinyl) naphthalene diimide; PTCDI−DAQ − [N,N'-bis(2-anthraquinone)]-perylene-3,4,9,10-tetracarboxydiimide; HOF−DAT – Hydrogen bonded organic framework diaminotriazole; PI@NC − Poly (3,4,9,10-perylenetetracarboxylic dianhydride ethylene diamine) @ nitrogen doped carbon; NDI−TFP − naphthalene diimide (NDI) and triformylphloroglucinol; PAQS − Poly(2,6-anthraquinonyl sulfide); PI − N,N′-diamino-3,4,9,10 perylenetetracarboxylic polyimide

Additional Figures S36–S43, Table S3

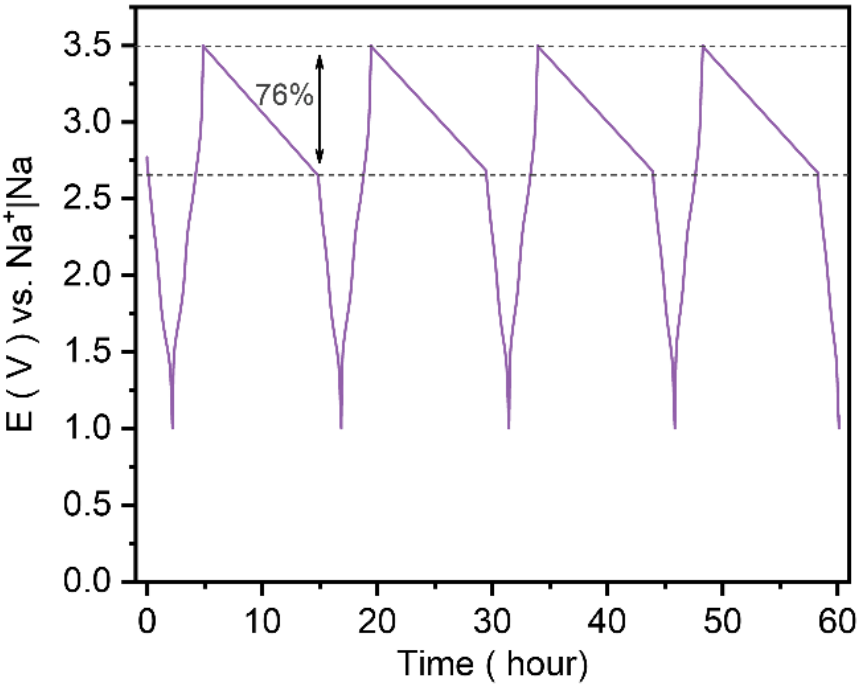

Figure S36. Open circuit voltage decay of the PPTO@CNTs@KB electrode in a Na half-cell in 1 M $NaPF_6$ in DEGDME electrolyte at room temperature over a ten-hour resting period after charging the cell to 3.5 V *vs*. Na$^+$|Na. The cell was given 30 activation cycles at the current rate of 1.0 A g^{-1} before the voltage decay experiment. The voltage decay test was performed at the current rate of 0.1 A g^{-1}.

Table S3: Literature references corresponding to panel "f" of Figure 3.

Organic Compound	Reference
PPTO-CNTs	[9]
PTO-COF@CNTs	[40]
PPTS	[10]
PBAQ	[17]
BAQB	[20]

PHATN	[18]
PPTO	[9]
PC-PDA-APS	[16]
PPTO@CNTs	[9]
PPQ	[23]
BPOE	[41]

Acronyms of the above table

PPTO – Poly(pyrene-4,5,9,10-tetraone); CNTs – Carbon nanotubes; PTO-COF@CNTs − pyrene-4,5,9,10-tetraone-based covalent organic framework; PPTS − poly(pentacenetetrone sulfide; PBAQ − Poly(benzene–anthraquinone) conjugated polymer; BAQB − 1,4-bis(9,10-anthraquinonyl)benzene; PHATN − poly(hexaazatrinaphthalene); PC-PDA-APS – Porous carbon-ammonium persulfate induced quinone rich Polydopamine; PPQ − poly(9,10-phenanthraquinone-alt-benzene); BPOE − bipolar porous organic electrode

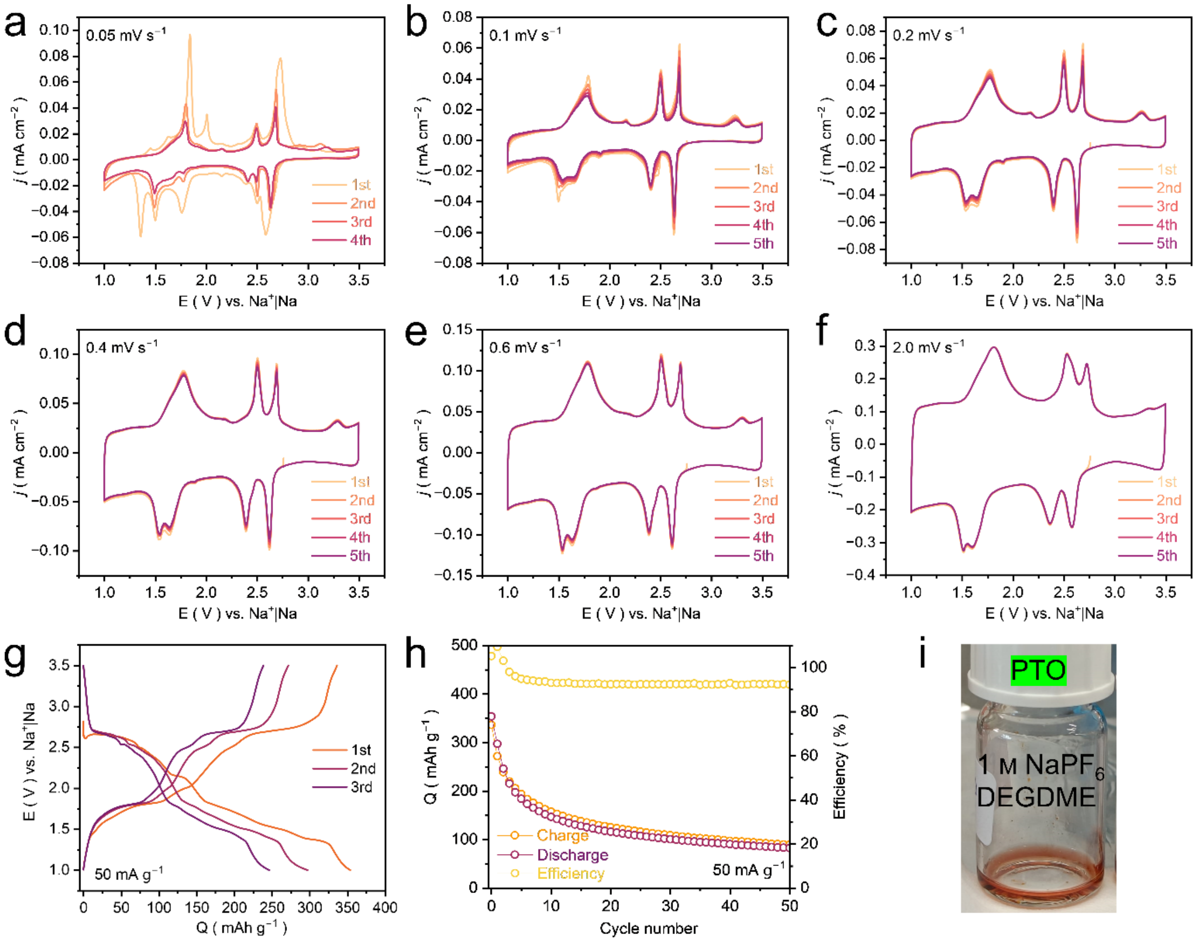

Figure S37. **(a-f)** Cyclic voltammetry profile of PTO@CNTs@KB electrode (PTO: CNTs: KB600: PVDF in 50:20:20:10 weight ratio) in 1 M $NaPF_6$ DEGDME electrolyte at room temperature at various scan rates. **(g)** Galvanostatic charge-discharge profile at 50 mA g^{-1} and **(h)** the corresponding cycle life. **(i)** Digital image of the solubility test of the as-prepared PTO powder dissolved in 1 M $NaPF_6$ in DEGDME electrolyte inside the glovebox.

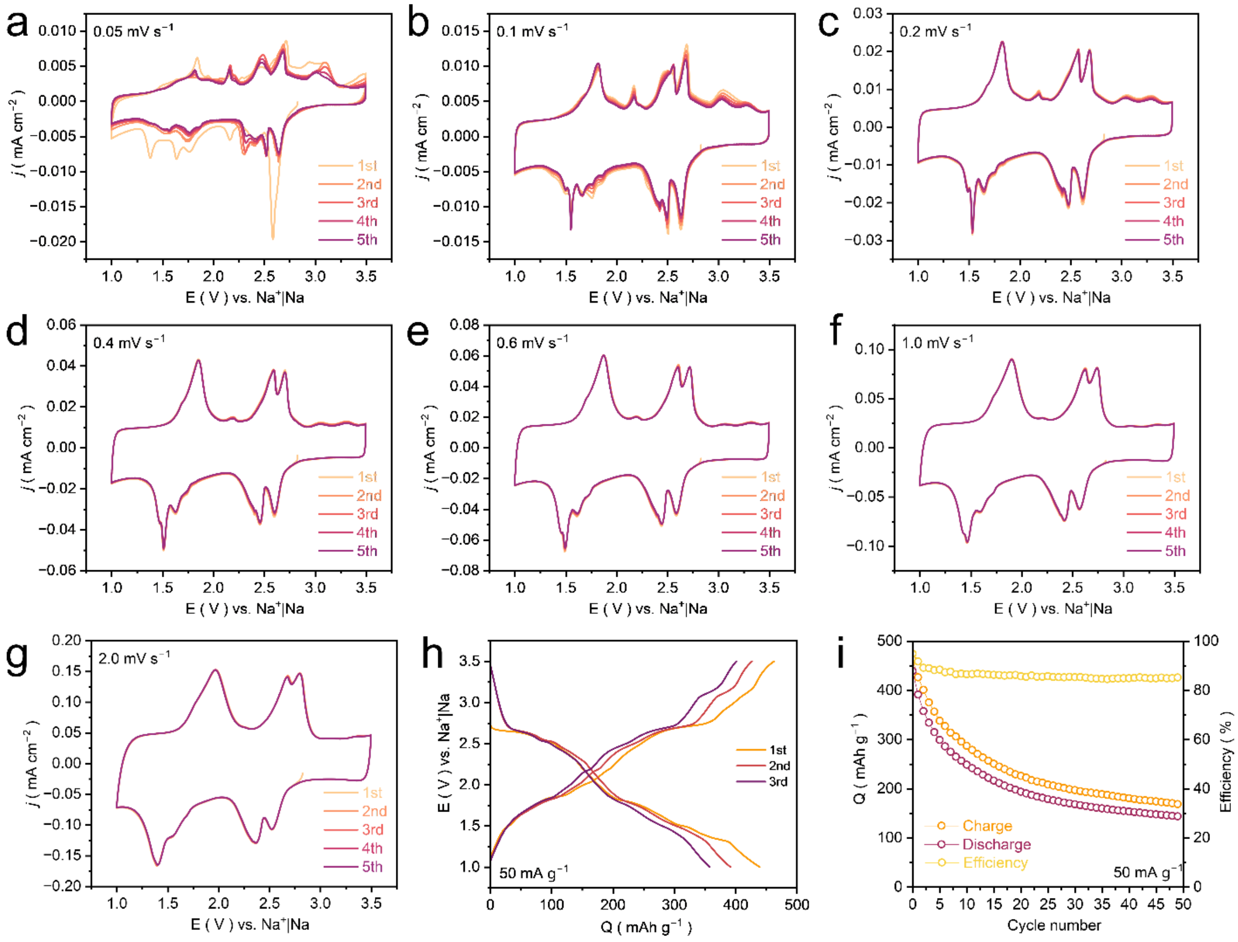

Figure S38. **(a-g)** Cyclic voltammetry profile of PTO@KB electrode (PTO:KB600:PVDF 50:40:10 weight ratio) in 1 M $NaPF_6$ DEGDME electrolyte at room temperature at various scan rates. **(h)** Galvanostatic charge-discharge profile at 50 mA g^{-1} and **(i)** the corresponding cycle life.

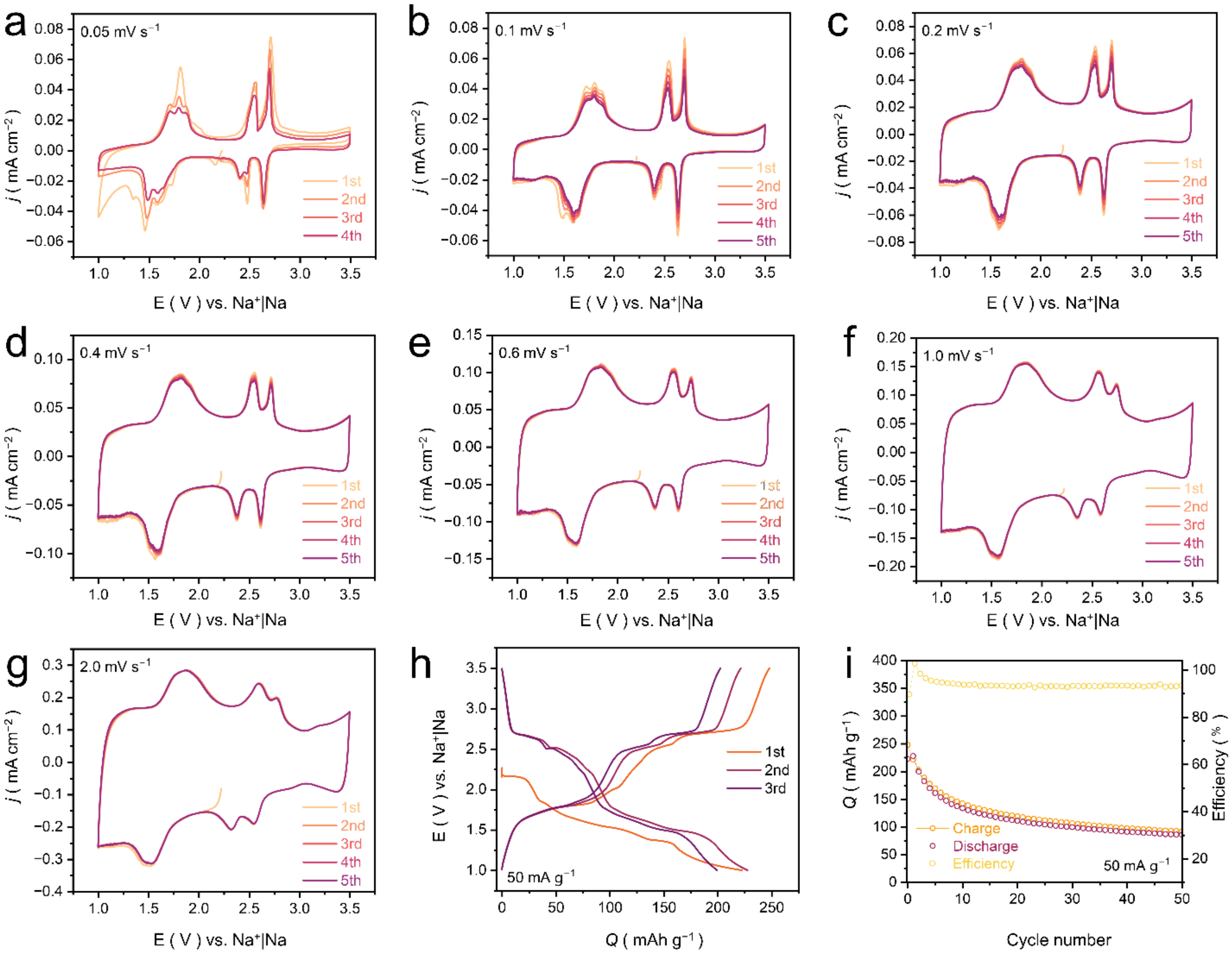

Figure S39. **(a-g)** Cyclic voltammetry profile of PTO@CNTs@KB electrode (PTO: CNTs: KB600: PVDF in 50:20:20:10 weight ratio) in 1 M $NaClO_4$ TEGDME electrolyte at room temperature at various scan rates. **(h)** Galvanostatic charge-discharge profile at 50 mA g^{-1} and **(i)** the corresponding cycle life.

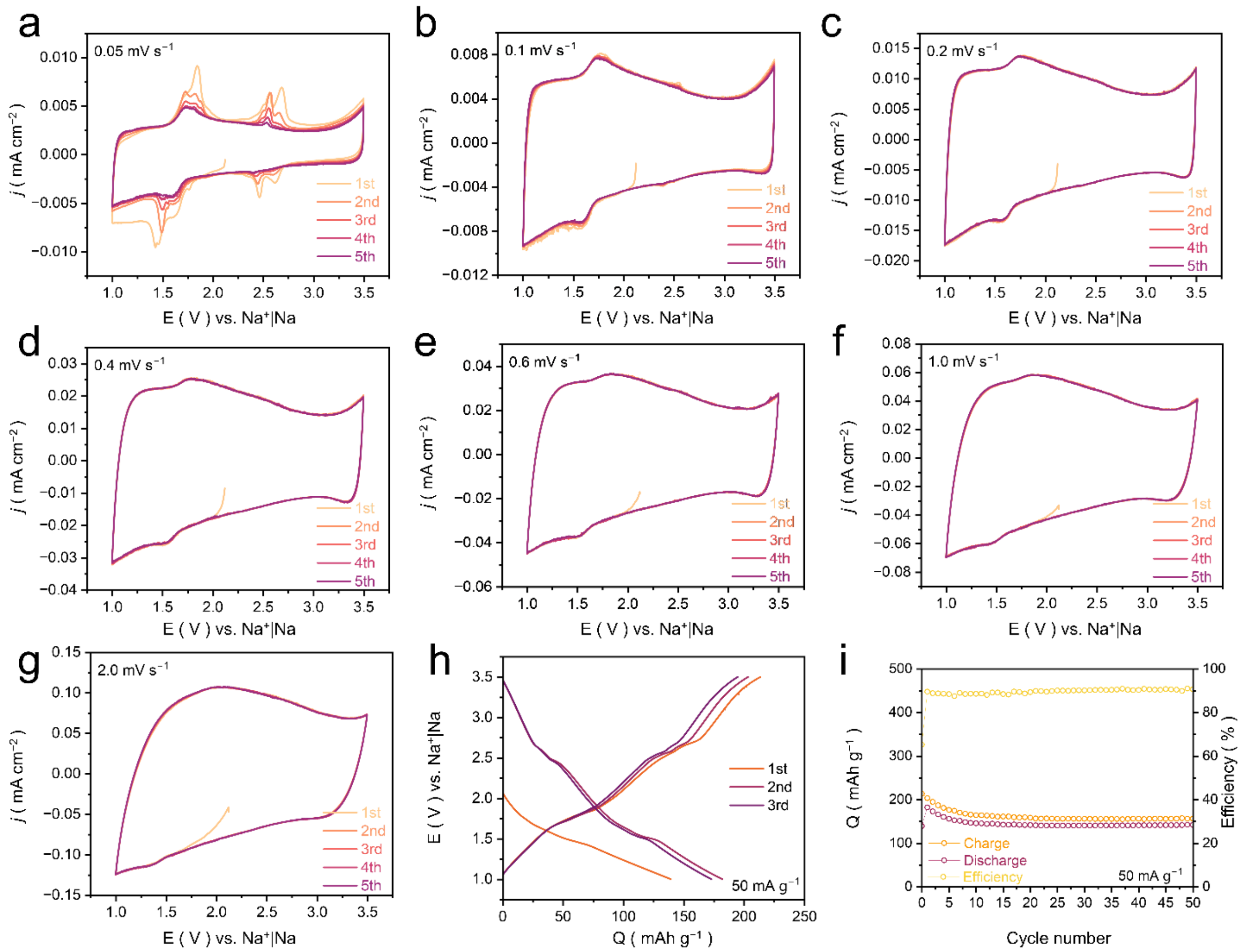

Figure S40. **(a-g)** Cyclic voltammetry profile of PTO@KB electrode (PTO:KB600:PVDF in 50:40:10 weight ratio) in 1 M $NaClO_4$ TEGDME electrolyte at room temperature at various scan rates. **(h)** Galvanostatic charge-discharge profile at 50 mA g^{-1} and **(i)** the corresponding cycle life.

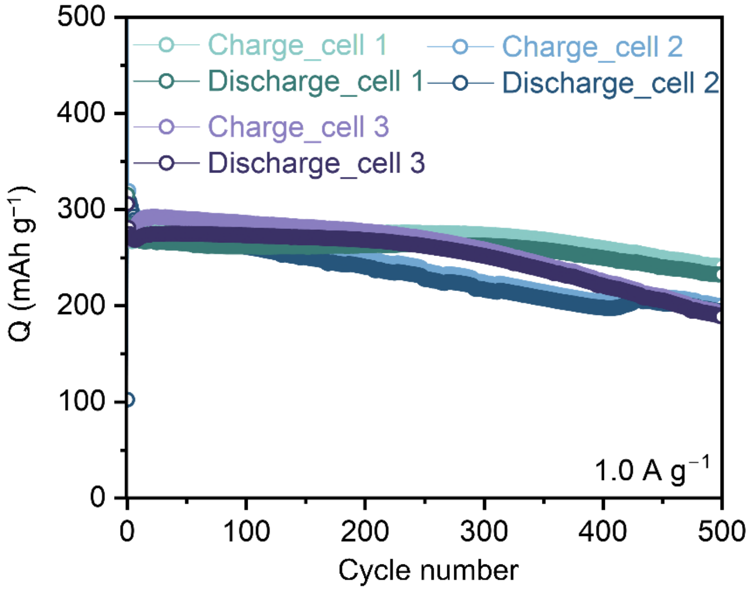

Figure S41. Galvanostatic charge-discharge cycling of PPTO@CNTs@KB electrode (Electrode composition → PPTO:SWCNTs:KB600:PVDF in 50:20:20:10 weight ratio) at a current rate of 1.0 A g^{-1} in 1 M $NaPF_6$ DEGDME electrolyte at room temperature.

Calculation of standard deviation

The standard deviation for the constant current cycling experiment was calculated using the equation below.

$$\Sigma = \sqrt{\frac{\sum(X - \mu)^2}{N}} \qquad \text{S2}$$

σ = standard deviation

X = each/individual value

µ = mean value

N = number of values

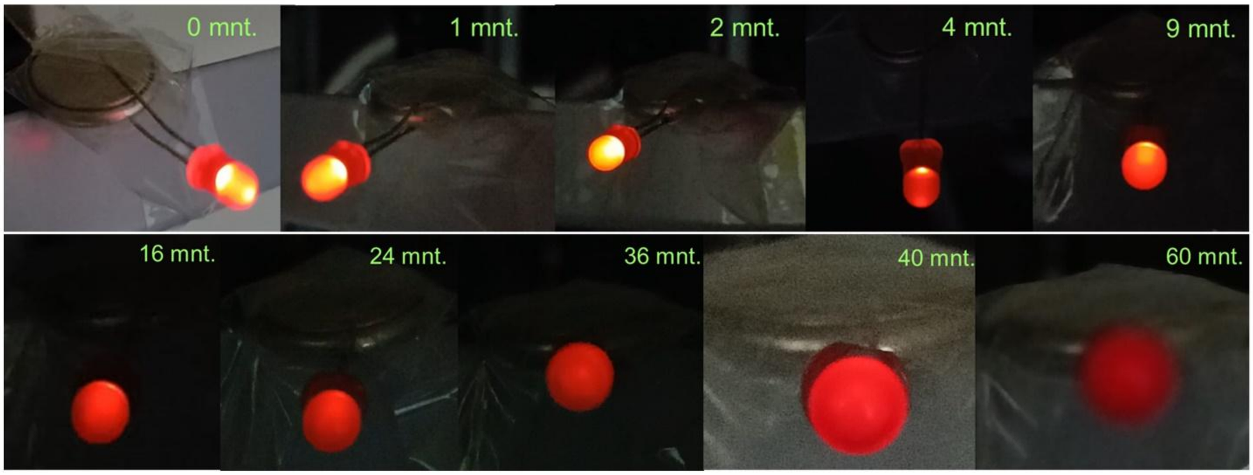

Figure S42. Digital images of a red light-emitting diode (LED) light powered by a single PPTO@CNTs@KB|Na coin cell with 1 M $NaPF_6$ DEGDME electrolyte at room temperature for ~60 minutes. The cell was charged to 3.5 V vs. $Na^+|Na$ (100% SoC), and the LED was connected immediately after that. LED voltage is ~1.8 V. The pictures were taken after the specific time period. The active material mass loading of this coin-cell is in the range of 0.5-0.6 mg cm^{-2}.

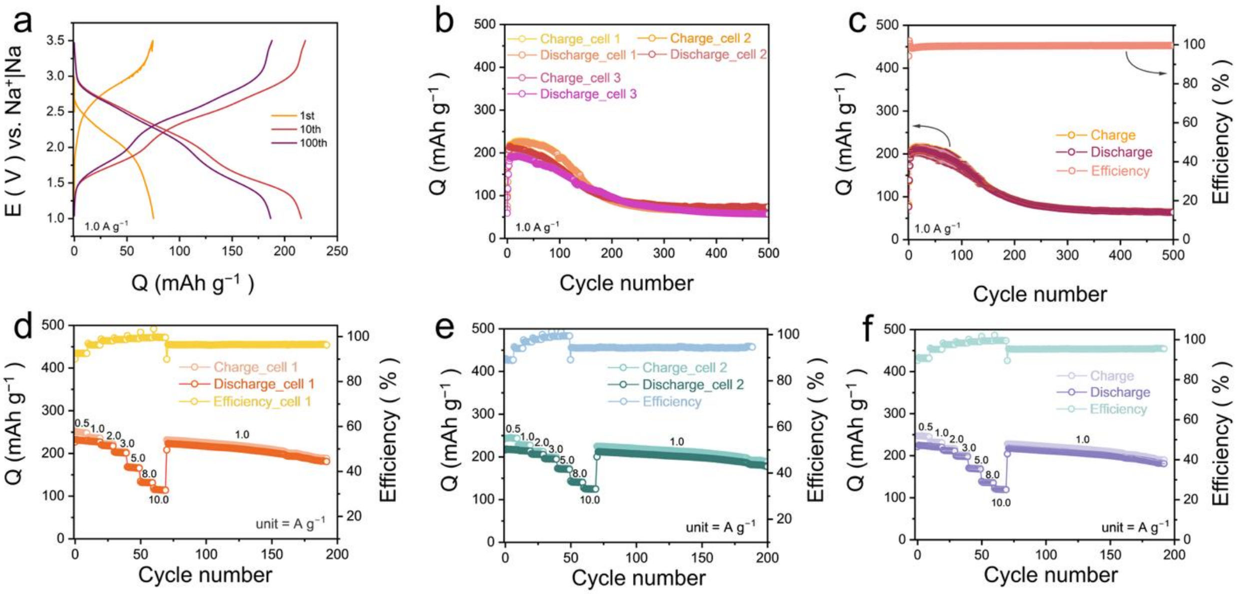

Figure S43. **(a)** Galvanostatic charge-discharge cycling of PPTO@CNTs@KB electrode (PPTO:SWCNTs:KB600:PVDF in 70:15:10:05 weight ratio) in 1 M $NaPF_6$ DEGDME electrolyte at room temperature at a current rate of 1.0 A g^{-1} (results from the first cell). **(b)** Constant current cycling of three separate cells at a current rate of 1.0 A g^{-1}. **(c)** Average of the constant current cycling at 1.0 A g^{-1} of the three cells from (**b**) with error bars. **(d, e)** Constant current cycling at different current rates from the two cells. **(f)** Average of the constant current cycling at different current rates of the two cells from **(d,e)** with error bars.

Redox potential quantum calculations (Table S4, Figure S44)

There are currently two protocols, the direct and isodesmic models, for the theoretical prediction of standard redox potentials in solution. In both cases, a thermodynamic cycle linking the processes in the gas phase with those in the solvent is used. In the direct method, the half-reaction (reduction of PTO) is used in the calculation, whereas in the isodesmic model, a full cell reaction (PTO reduction and Na oxidation) is postulated. We assume that reacting species behave as ideal gases within the rigid rotator–harmonic oscillator approximation. The standard Gibbs free energy of redox reaction, $-\Delta G^\circ_{(s)}$, consists of the free energy change in the gas phase and the solvation free energies of the oxidized and reduced species. The results on the electrode potential values from both methods correlate qualitatively with each other. Comparing with the experimental data, the direct method shows much larger deviations compared with the isodesmic model and therefore, we will discuss in this paper the results of the isodesmic model based on the following thermodynamic cycle:

$$\begin{tikzcd}
\text{PTO (g)} + n\text{Na (g)} \arrow[r, "\Delta G^\circ_{\text{i}}"] \arrow[d, "\Delta G_r{}^\circ{}_{\text{solv}}"] & \text{PTO}^{-n}\text{ (g)} + n\text{Na}^+\text{ (g)} \arrow[r, "\Delta G^\circ_{\text{r}}"] & \text{PTO-nNa (g)} \arrow[d, "\Delta G_p{}^\circ{}_{\text{solv}}"'] \\
\text{PTO (s)} + n\text{Na (s)} \arrow[rr, dashed, "\Delta G^\circ_{(\text{s})}"] & & \text{PTO-nNa (s)}
\end{tikzcd}$$

The Gibbs free energies can be correlated with the redox potential through the equation:

$$E^\circ\ (\text{s}) = -\Delta G^\circ_{(\text{s})} / nF = -(-\Delta G_r{}^\circ{}_{\text{solv}} + \Delta G^\circ_{\text{i}} + \Delta G^\circ_{\text{r}} + \Delta G_p{}^\circ{}_{\text{solv}}) / nF$$

with *F* for the Faraday constant and n for the number of electrons in the process.

Table S4: Calculated redox potentials of PTO in DEGDME with a 7.5 dielectric constant (isodesmic cell reaction model). * Corrected values were derived by calibrating the first calculated potential against the experimental value (E° (s) [V] + 0.11 V)

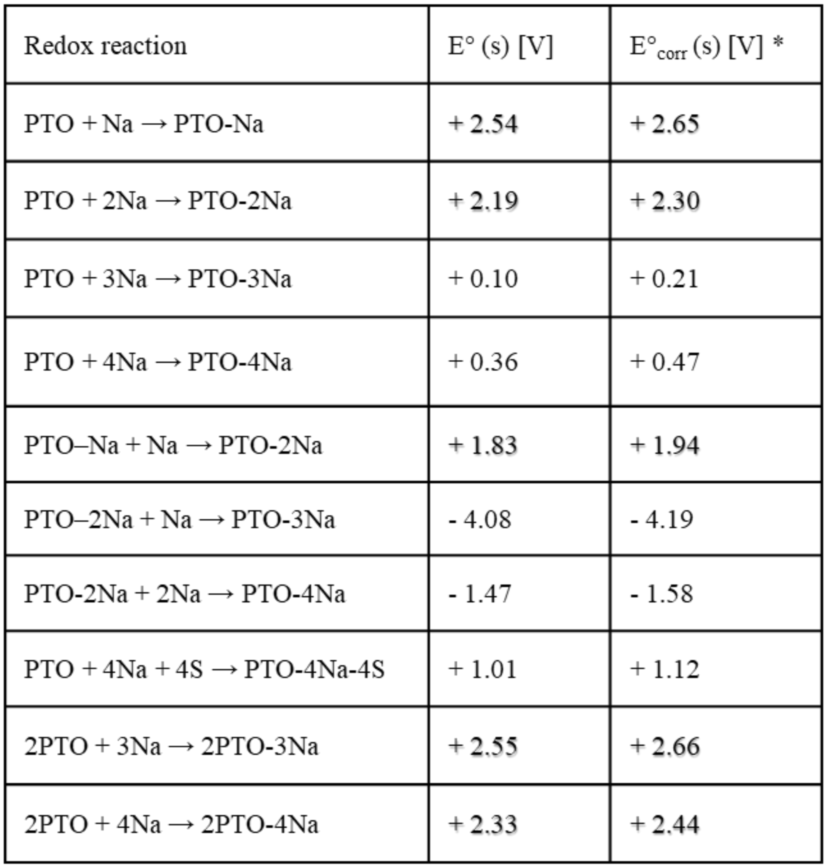

Redox reaction	E° (s) [V]	$E°_{corr}$ (s) [V] *
PTO + Na → PTO-Na	**+ 2.54**	**+ 2.65**
PTO + 2Na → PTO-2Na	**+ 2.19**	**+ 2.30**
PTO + 3Na → PTO-3Na	+ 0.10	+ 0.21
PTO + 4Na → PTO-4Na	+ 0.36	+ 0.47
PTO–Na + Na → PTO-2Na	**+ 1.83**	**+ 1.94**
PTO–2Na + Na → PTO-3Na	- 4.08	- 4.19
PTO-2Na + 2Na → PTO-4Na	- 1.47	- 1.58
PTO + 4Na + 4S → PTO-4Na-4S	+ 1.01	+ 1.12
2PTO + 3Na → 2PTO-3Na	**+ 2.55**	**+ 2.66**
2PTO + 4Na → 2PTO-4Na	**+ 2.33**	**+ 2.44**

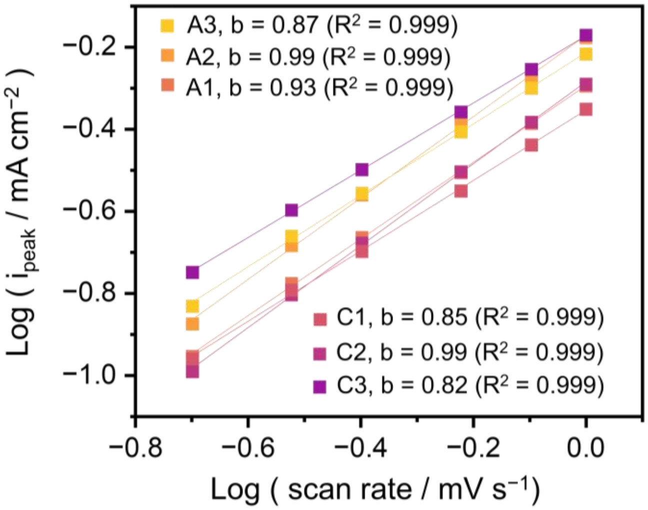

Figure S44. Plot with linear fits of log(i) versus log(ν) from the different redox peaks of the PPTO@CNTs@KB electrode.

GITT measurements (Figure S45, Table S5)

The galvanostatic intermittent titration technique (GITT) measurements were performed by applying a current pulse of 200 mA g^{-1} for 10 minutes, followed by a 4-hour relaxation time. The sodium-ion diffusion coefficient in the PPTO@CNTs@KB electrode was calculated using the following equation:[8,42–45]

$$D_{Na+} = \frac{4}{\pi}\left(\frac{n_m V_m}{S}\right)^2\left(\frac{\Delta E_S}{\tau\left(\frac{dE_\tau}{d\sqrt{\tau}}\right)}\right)^2 = \frac{4}{\pi}\left(\frac{V}{S}\right)^2\left(\frac{\Delta E_S}{\tau\left(\frac{dE_\tau}{d\sqrt{\tau}}\right)}\right)^2 \approx \frac{4}{\pi\tau}(L)^2\left(\frac{\Delta E_S}{\Delta E_\tau}\right)^2 \qquad S3$$

Here, n_m, V_m, and S represent the mole number, molar volume of the active material, and effective surface area (1.13 cm^2) of the electrode, respectively. **τ** is the relaxation time required to reach a steady state, L is the average dry thickness of the electrode (25.95 µm). ΔE_S is the voltage change between consecutive relaxation periods, and ΔE_τ is the voltage change after every constant pulse during the charge/discharge process. The schematic below illustrates the potential changes.

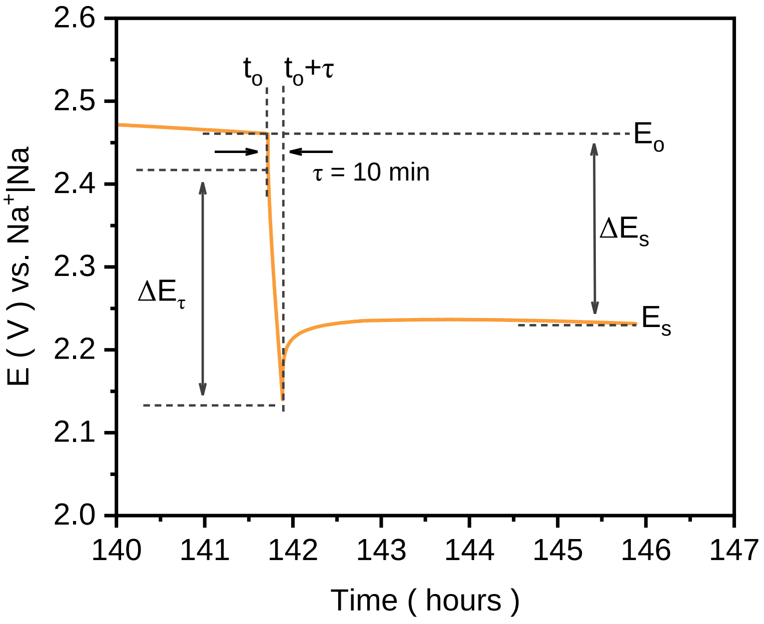

Figure S45. GITT measurement of PPTO@CNTs@KB *vs.* Na cell. Demonstration of a single titration during the GITT test with labeling of various parameters.

Table S5. Comparison of the Na^+ diffusion coefficients of the various OAM-based positive electrodes for Na batteries.

Positive electrode	**D_{Na^+} ($cm^2\ s^{-1}$)**	**Reference**
PPTO@CNTs@KB	**2.85×10^{-10}**	**This work**
PPTO-CNTs	$\sim 1.00 \times 10^{-11}$	[9]
P5Q@CMK-3	1.29×10^{-11}	[8]
Na_2BNDI	$\sim 2.00 \times 10^{-11}$	[33]
PBAQ-3	$\sim 1.00 \times 10^{-10}$	[17]
TAPQ	$\sim 5.00 \times 10^{-11}$	[46]
PAQS	1.34×10^{-10}	[21]
SAQ	1.9×10^{-19} - 7.7×10^{-19}	[47]
Tp-PTO-COF@CNTs	2.4×10^{-11}	[40]
Tp-PTO-COF	2.3×10^{-11}	[40]

PTCDA/NC/CNTs	8.15×10^{-13}	[48]
Tp-PTO-COF/CNTs	3.2×10^{-11}	[40]
$Na_3V_2(PO_4)_3$	10^{-12} -$10^{-14.5}$	[49]
$Na_2C_6O_6$	7.9×10^{-16}	[50]
P3-$Na_{0.62}Ti_{0.37}Cr_{0.63}O_2$	9.0×10^{-14}	[51]
$Na_2AQ_{26}DS$	2.2×10^{-13}	[52]
P2-$Na_{0.62}Ti_{0.37}Cr_{0.63}O_2$	2.0×10^{-13}	[51]

Additional Figures S46–S54

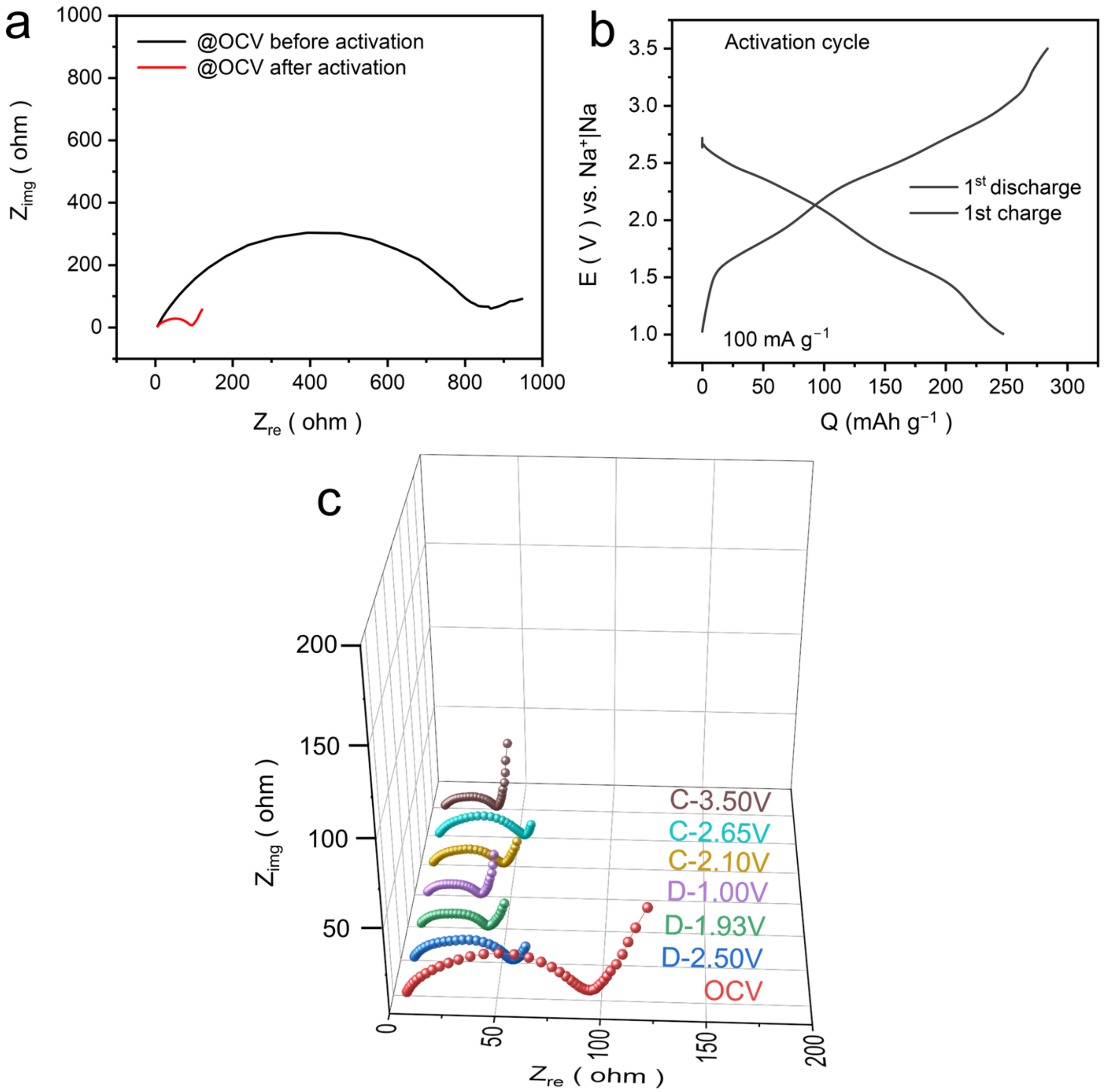

Figure S46. Electrochemical impedance spectroscopy (EIS) analysis of PPTO@CNTs@KB//Na cell in 1 M NaPF$_6$ DEGDME electrolyte at room temperature. (a) Nyquist plots at open-circuit voltage before and after the activation cycle. **(b)** Galvanostatic charge-discharge profile (activation cycle) at a current rate of 100 mA g^{-1}. **(c)** Nyquist plots were recorded in the PEIS mode at various charge-discharge states with 7 points per decay, having logarithmic spacing.

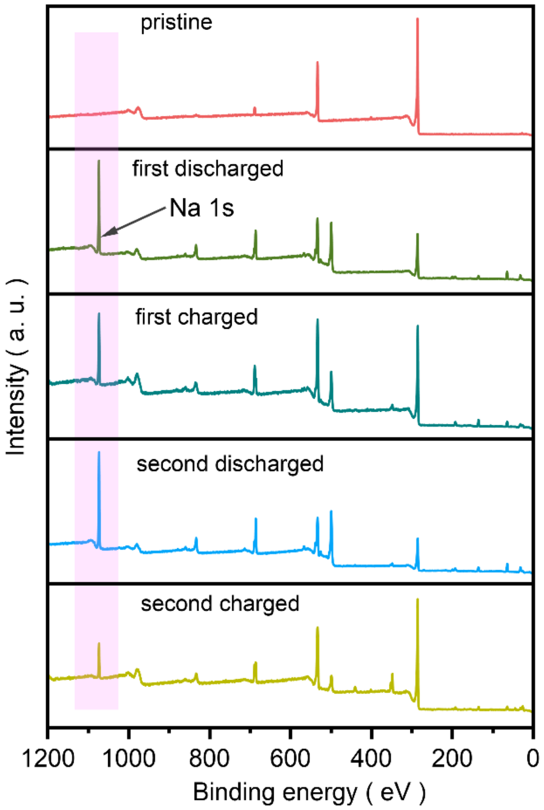

Figure S47. XPS survey spectra of PPTO@CNTs@KB electrodes at different states of charge and discharge.

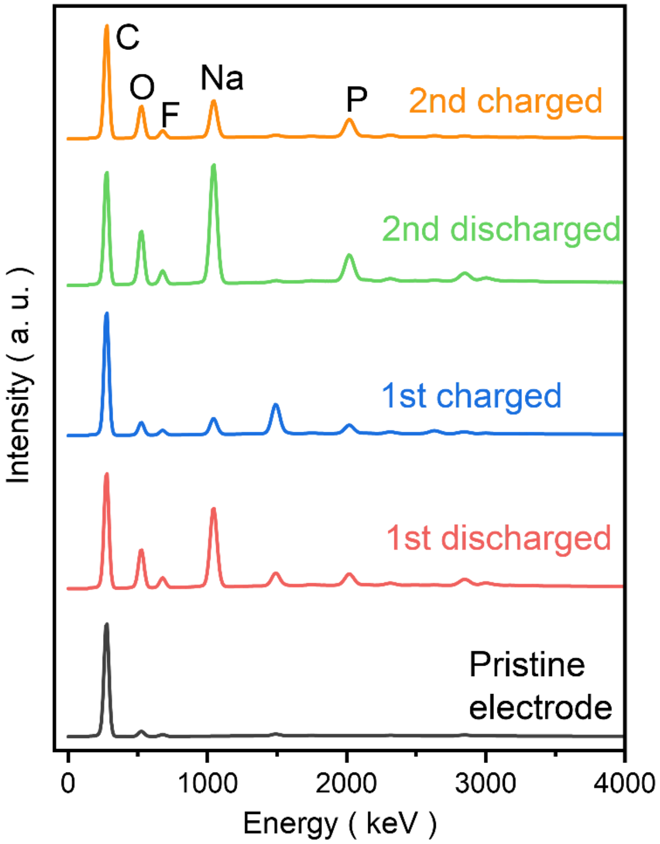

Figure S48. Ex-situ EDS spectra of PPTO@CNTs@KB electrodes at different states of charge and discharge. The phosphorus (P) and fluorine (F) peak possibly arises from the minute electrolyte salt left over at the electrode surface after washing (if any).

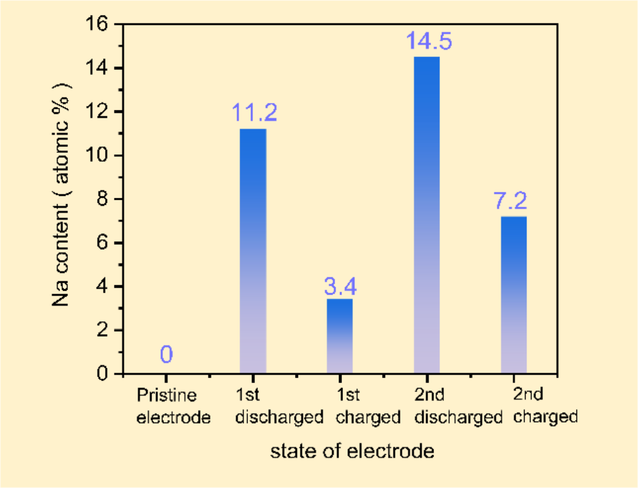

Figure S49. Relative sodium content in the PPTO@CNTs@KB electrode at various charged and discharged states, obtained from SEM-EDS analysis.

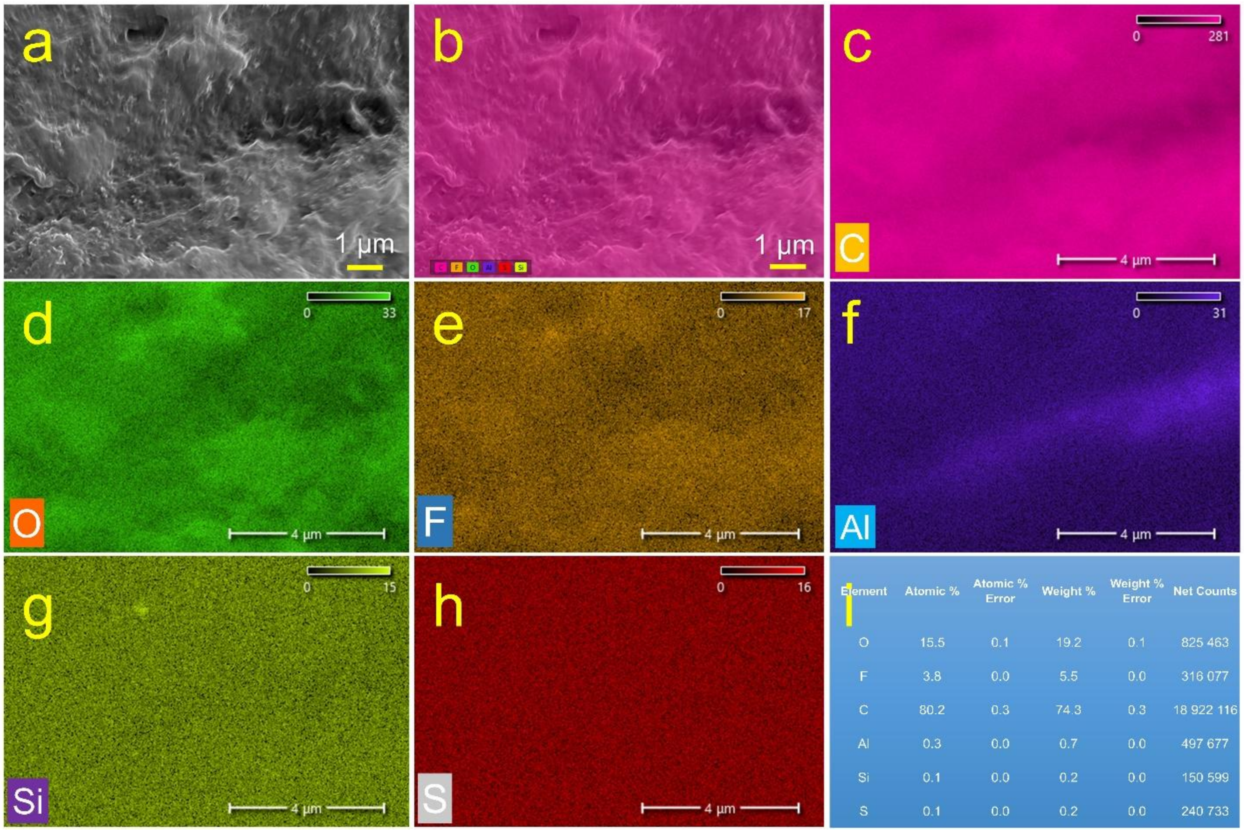

Element	Atomic %	Atomic % Error	Weight %	Weight % Error	Net Counts
O	15.5	0.1	19.2	0.1	825 463
F	3.8	0.0	5.5	0.0	316 077
C	80.2	0.3	74.3	0.3	18 922 116
Al	0.3	0.0	0.7	0.0	497 677
Si	0.1	0.0	0.2	0.0	150 599
S	0.1	0.0	0.2	0.0	240 733

Figure S50. EDS elemental mapping of the pristine PPTO@CNTs@KB electrode**. (a)** Selected area, **(b)** combined image of all elements, **(c)** carbon, **(d)** oxygen, **(e)** fluorine, **(f)** aluminum, **(g)** silicon, and **(h)** sulfur. **(i)** Compositional analysis table.

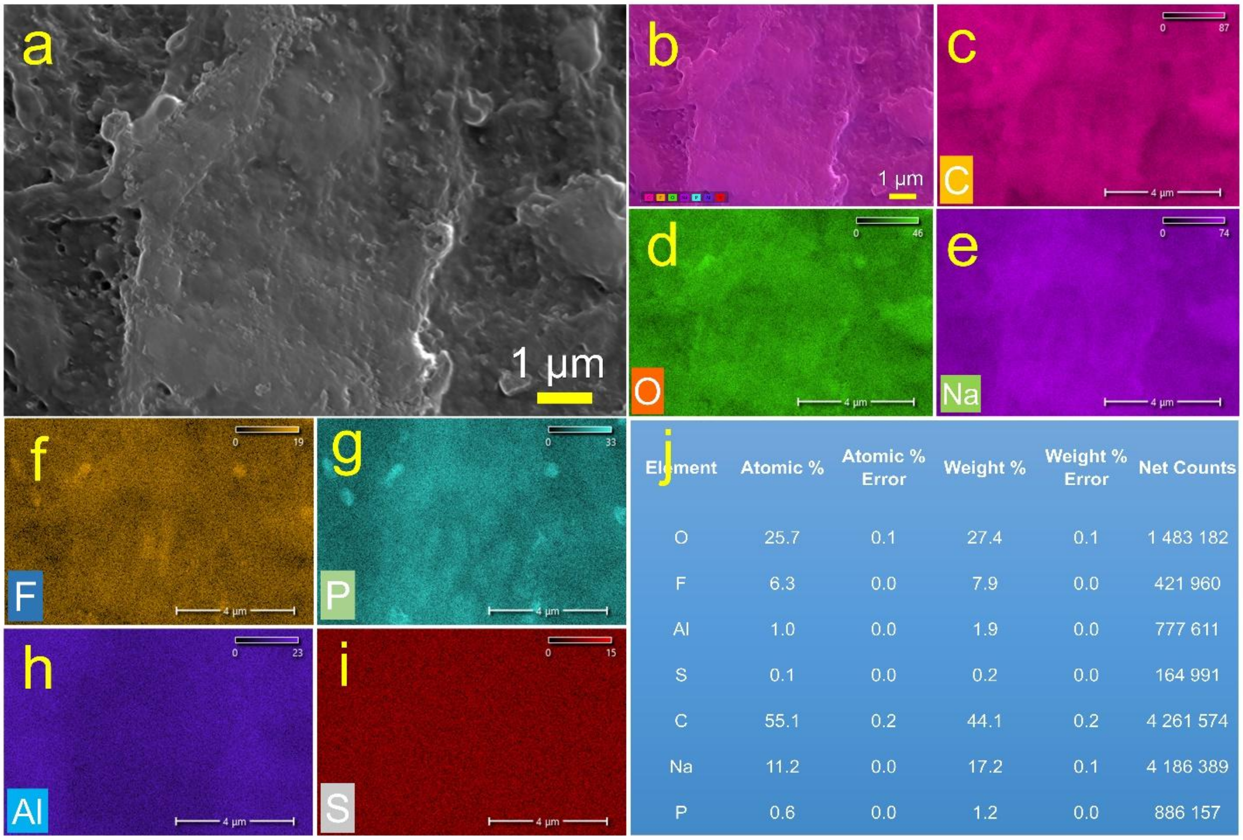

Element	Atomic %	Atomic % Error	Weight %	Weight % Error	Net Counts
O	25.7	0.1	27.4	0.1	1 483 182
F	6.3	0.0	7.9	0.0	421 960
Al	1.0	0.0	1.9	0.0	777 611
S	0.1	0.0	0.2	0.0	164 991
C	55.1	0.2	44.1	0.2	4 261 574
Na	11.2	0.0	17.2	0.1	4 186 389
P	0.6	0.0	1.2	0.0	886 157

Figure S51. EDS elemental mapping of the first discharged PPTO@CNTs@KB electrode**. (a)** Selected area, **(b)** combined image of all elements, **(c)** carbon, **(d)** oxygen, **(e)** sodium, **(f)** fluorine, **(g)** phosphorous **(h)** aluminum, and (i) sulfur. **(j)** Compositional analysis table.

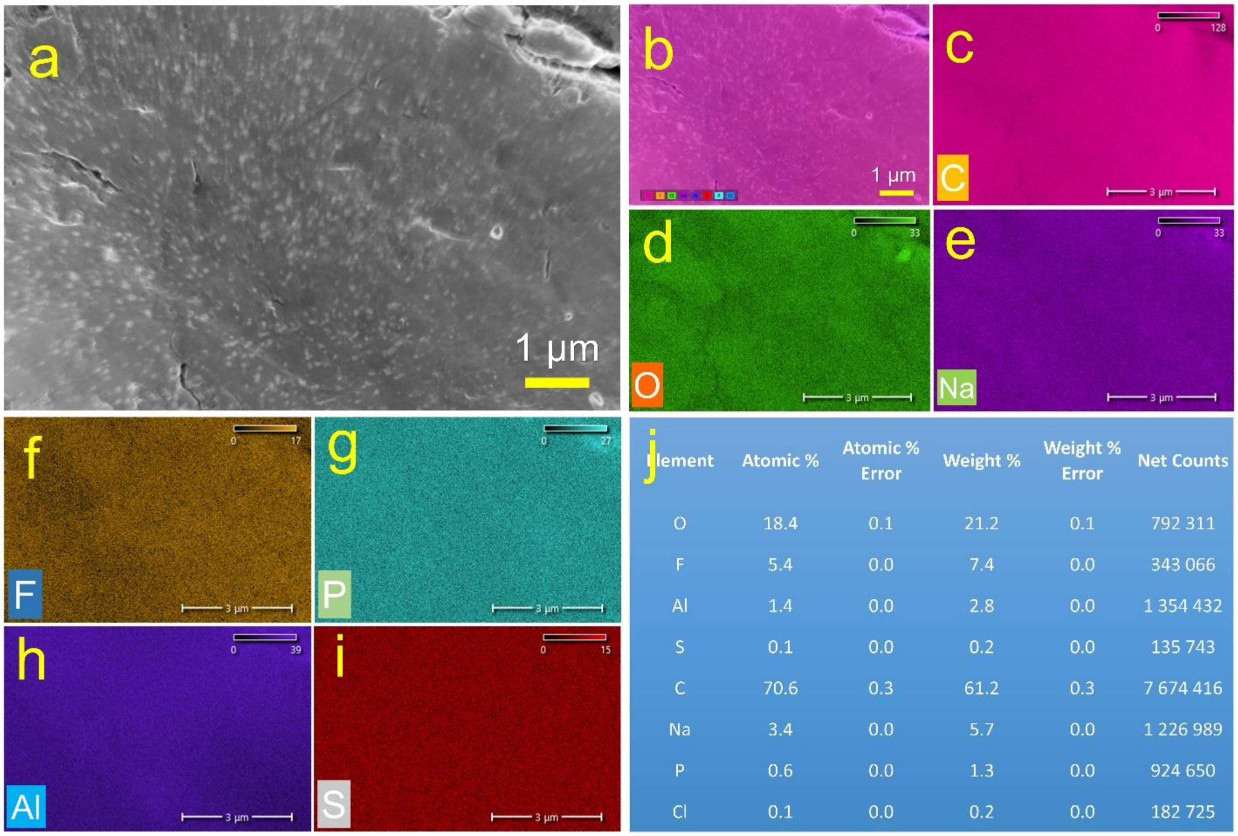

Element	Atomic %	Atomic % Error	Weight %	Weight % Error	Net Counts
O	18.4	0.1	21.2	0.1	792 311
F	5.4	0.0	7.4	0.0	343 066
Al	1.4	0.0	2.8	0.0	1 354 432
S	0.1	0.0	0.2	0.0	135 743
C	70.6	0.3	61.2	0.3	7 674 416
Na	3.4	0.0	5.7	0.0	1 226 989
P	0.6	0.0	1.3	0.0	924 650
Cl	0.1	0.0	0.2	0.0	182 725

Figure S52. EDS elemental mapping of the first charged PPTO@CNTs@KB electrode**. (a)** Selected area, **(b)** combined image of all elements, **(c)** carbon, **(d)** oxygen, **(e)** sodium, **(f)** fluorine, **(g)** phosphorous **(h)** aluminum, and (i) sulfur. **(j)** Compositional analysis table.

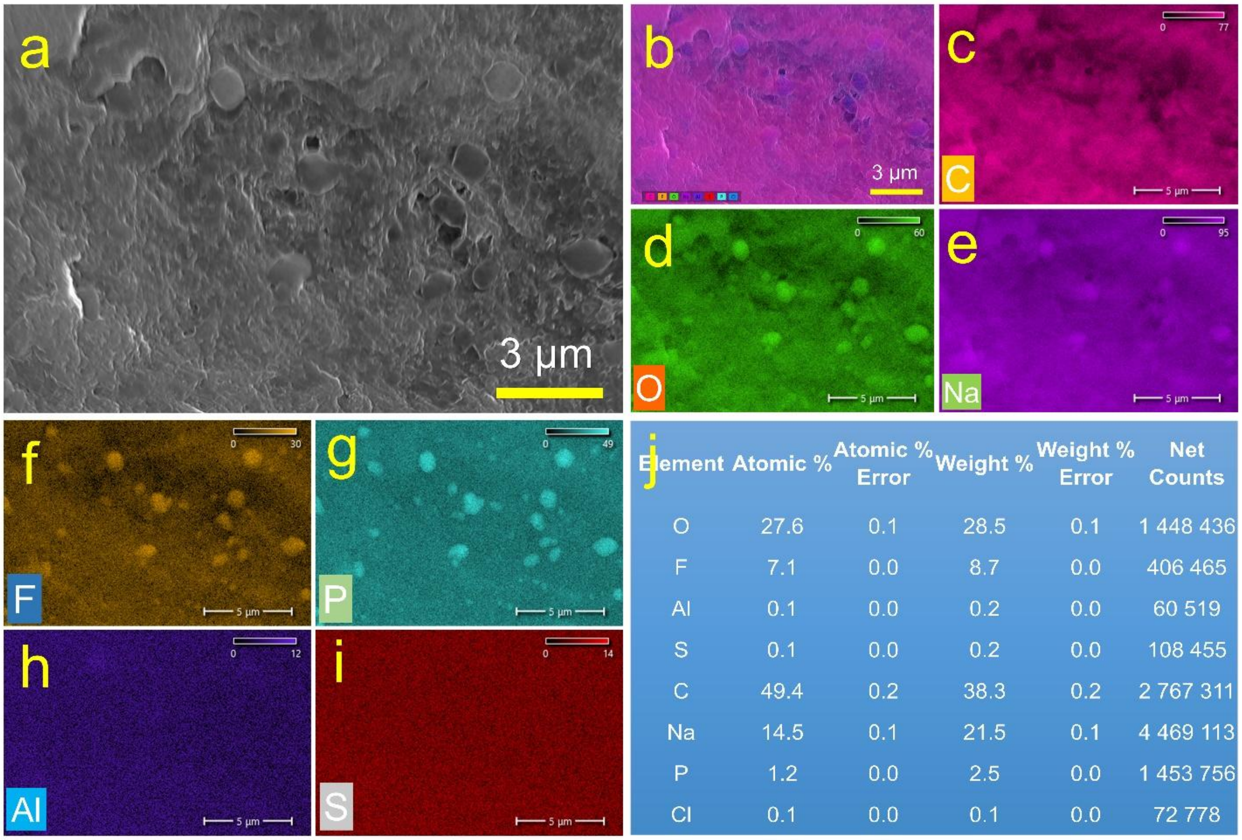

Element	Atomic %	Atomic % Error	Weight %	Weight % Error	Net Counts
O	27.6	0.1	28.5	0.1	1 448 436
F	7.1	0.0	8.7	0.0	406 465
Al	0.1	0.0	0.2	0.0	60 519
S	0.1	0.0	0.2	0.0	108 455
C	49.4	0.2	38.3	0.2	2 767 311
Na	14.5	0.1	21.5	0.1	4 469 113
P	1.2	0.0	2.5	0.0	1 453 756
Cl	0.1	0.0	0.1	0.0	72 778

Figure S53. EDS elemental mapping of the second discharged PPTO@CNTs@KB electrode**. (a)** Selected area, **(b)** combined image of all elements, **(c)** carbon, **(d)** oxygen, **(e)** sodium, **(f)** fluorine, **(g)** phosphorous **(h)** aluminum, and (i) sulfur. **(j)** Compositional analysis table.

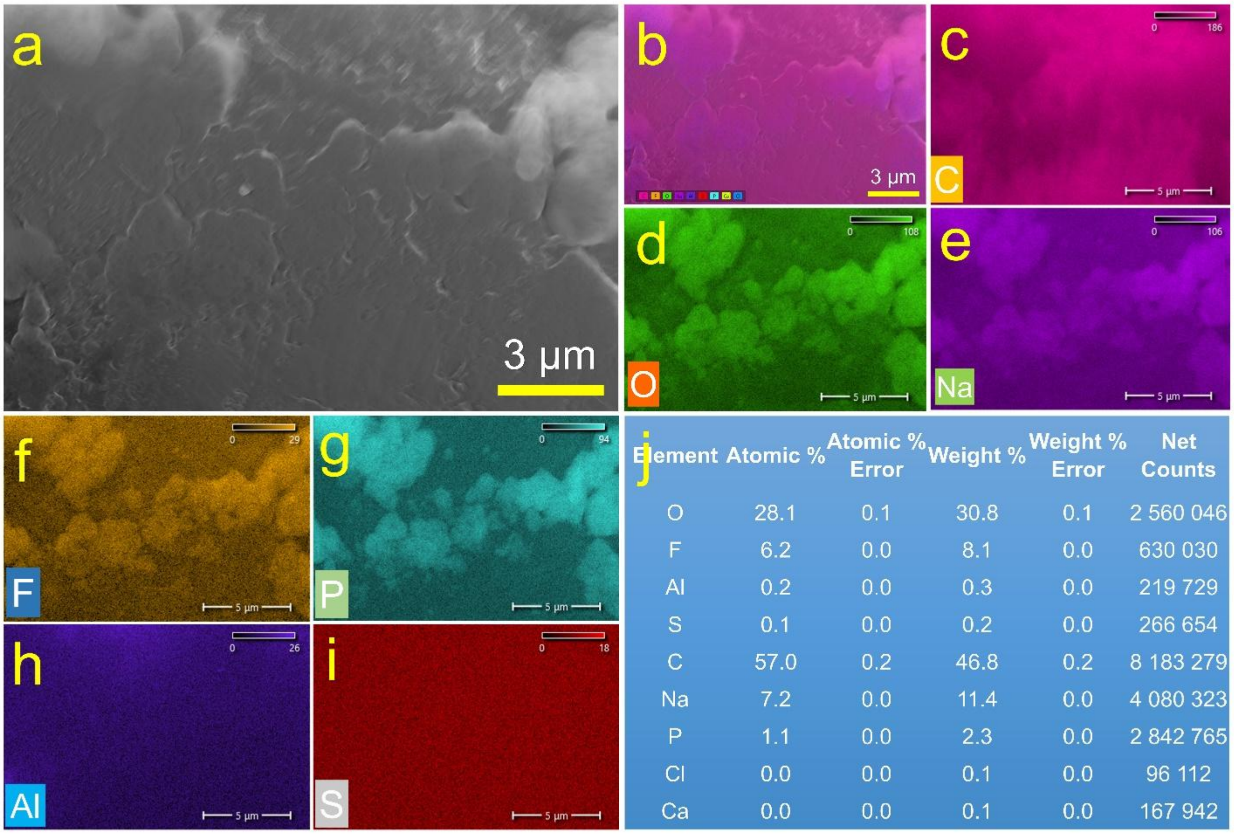

Element	Atomic %	Atomic % Error	Weight %	Weight % Error	Net Counts
O	28.1	0.1	30.8	0.1	2 560 046
F	6.2	0.0	8.1	0.0	630 030
Al	0.2	0.0	0.3	0.0	219 729
S	0.1	0.0	0.2	0.0	266 654
C	57.0	0.2	46.8	0.2	8 183 279
Na	7.2	0.0	11.4	0.0	4 080 323
P	1.1	0.0	2.3	0.0	2 842 765
Cl	0.0	0.0	0.1	0.0	96 112
Ca	0.0	0.0	0.1	0.0	167 942

Figure S54. EDS elemental mapping of the second charged PPTO@CNTs@KB electrode**. (a)** Selected area, **(b)** combined image of all elements, **(c)** carbon, **(d)** oxygen, **(e)** sodium, **(f)** fluorine, **(g)** phosphorous, **(h)** aluminum, and **(i)** sulfur. **(j)** Compositional analysis table.

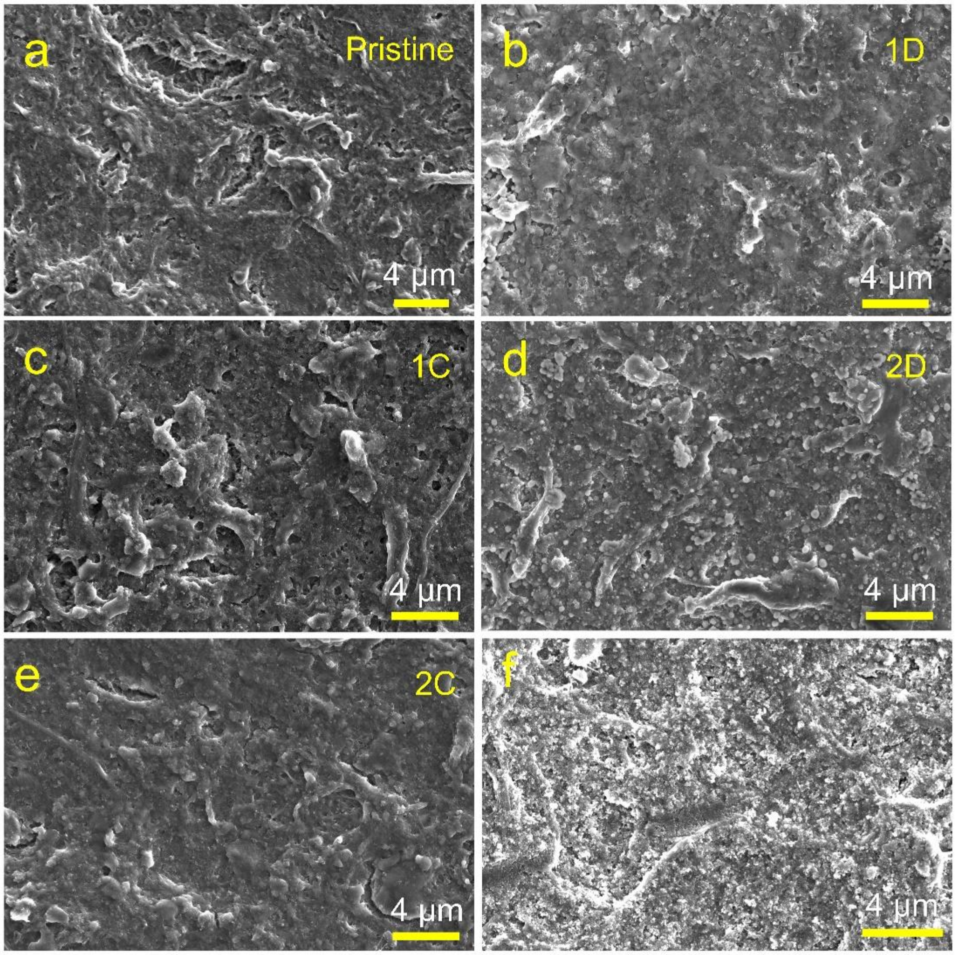

Figure S55. FE-SEM images of the PPTO@CNTs@KB electrode at different states of charge**. (a)** pristine electrode, **(b)** first discharged, **(c)** first charged, **(d)** second discharged, **(e)** second charged, and **(f)** after 500 cycles at 1 A g^{-1}.

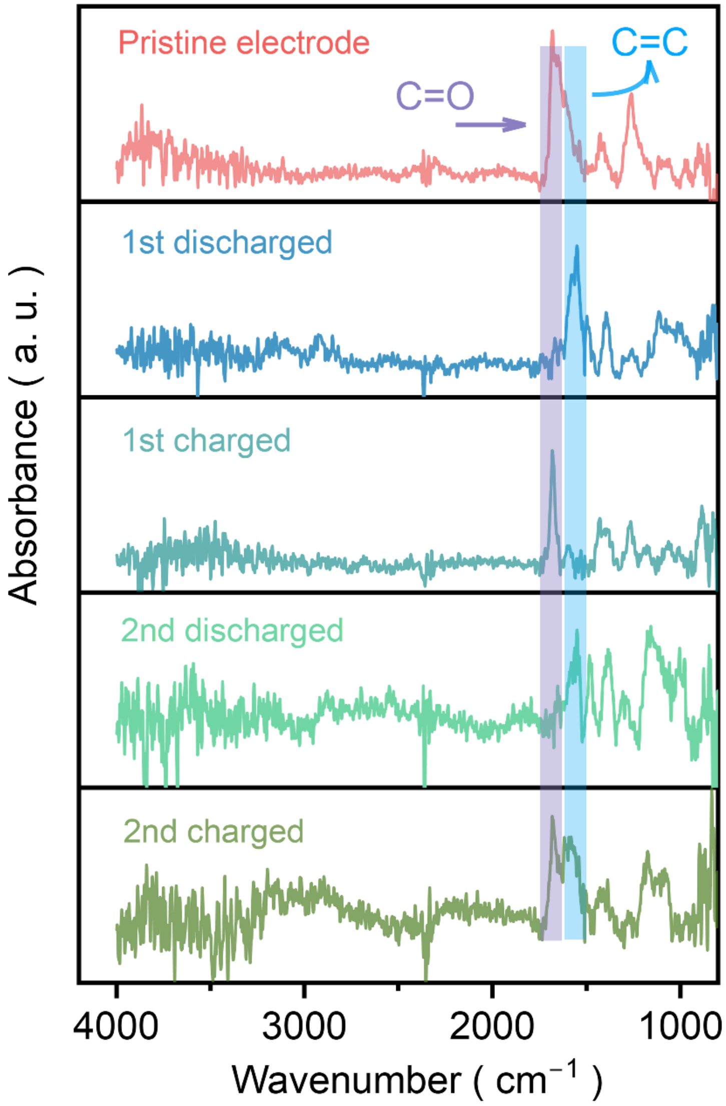

Figure S56. Ex-situ ATR-FTIR spectra at different states of charge for the PPTO@CNTs@KB electrode.

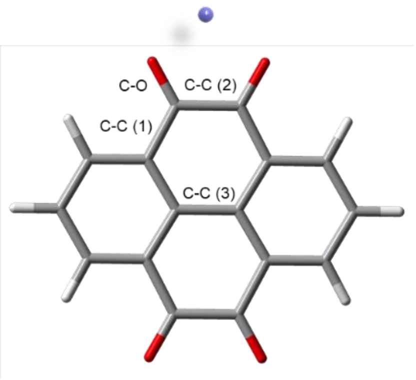

Bond	PTO (s) [Å]	PTO-2Na (s) [Å]	PTO-4Na (s) [Å]
C-C (1)	1.49 (1.48)	1.45 (1.45)	1.45 (1.45)
C-O	1.21 (1.21)	1.28 (1.27)	1.35 (1.34)
C-C (2)	1.54 (1.55)	1.48 (1.48)	1.40 (1.42)
C-C (3)	1.48 (1.48)	1.40 (1.40)	1.43 (1.42)

Figure S57. Selected bond distances obtained from the calculated most stable geometry of PTO, reduced PTO-1Na, and PTO-4Na in the gas phase and in solution (values in brackets). Atom color coding: Carbon: grey, oxygen: red, hydrogen: white, and sodium ion: violet.

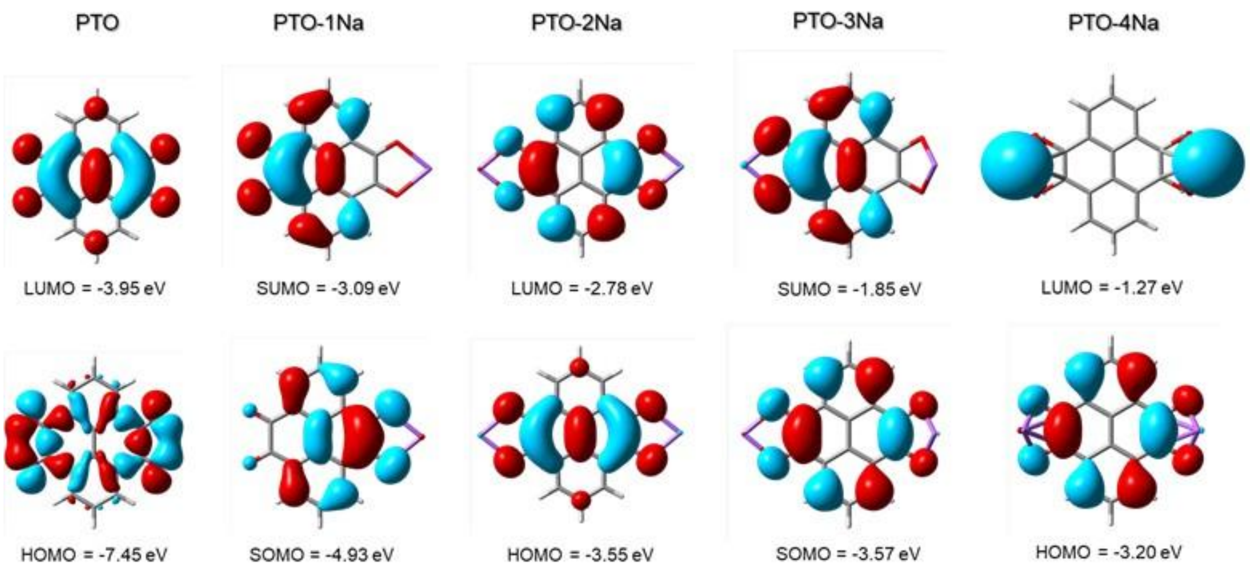

Figure S58. Calculated frontier molecular orbitals of PTO and reduced PTO-nNa (n = 1–4) in the gas phase.

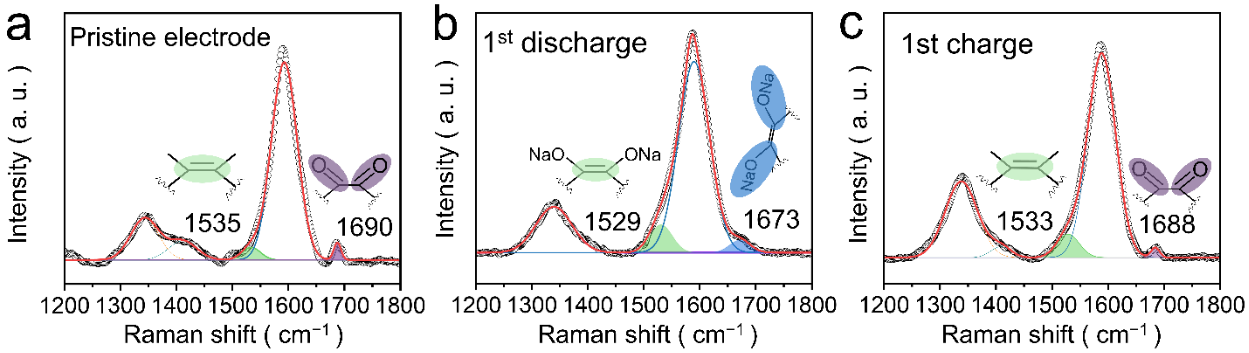

Figure S59. Ex-situ Raman spectra of the PPTO@CNTs@KB electrode at (a) pristine, (b) 1st discharged process, and (c) first charged process.

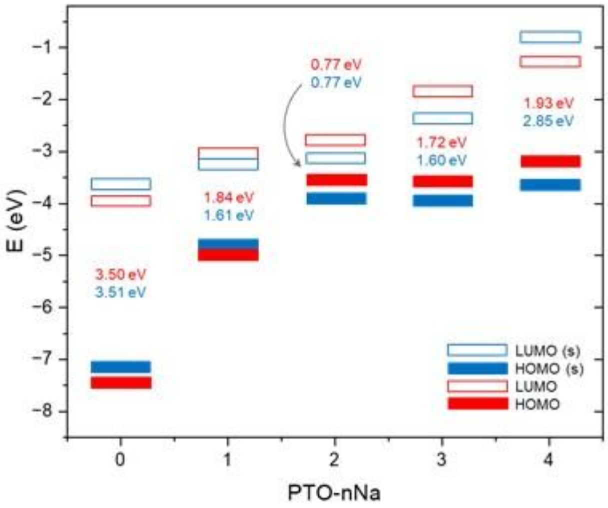

Figure S60. Frontier molecular orbital energies of PTO and reduced PTO-nNa species (n = 1–4) in the gas (red) and solvent (blue) phase.

References

[1] R. Wessling, K. Chinner, P. Wenz, C. Douglas, O. Dumele, B. Esser, *Org. Lett.* **2025**, *27*, 12047.

[2] J. Schindelin, I. Arganda-Carreras, E. Frise, V. Kaynig, M. Longair, T. Pietzsch, S. Preibisch, C. Rueden, S. Saalfeld, B. Schmid, J. Y. Tinevez, D. J. White, V. Hartenstein, K. Eliceiri, P. Tomancak, A. Cardona, *Nat. Methods* **2012**, *9*, 676.

[3] M. Osenberg, A. Hilger, M. Neumann, A. Wagner, N. Bohn, J. R. Binder, V. Schmidt, J. Banhart, I. Manke, *J. Power Sources* **2023**, *570*, 233030.

[4] S. Berg, D. Kutra, T. Kroeger, C. N. Straehle, B. X. Kausler, C. Haubold, M. Schiegg, J. Ales, T. Beier, M. Rudy, K. Eren, J. I. Cervantes, B. Xu, F. Beuttenmueller, A. Wolny, C. Zhang, U. Koethe, F. A. Hamprecht, A. Kreshuk, *Nat. Methods* **2019**, *16*, 1226.

[5] B. Prifling, M. Weber, N. Ray, A. Prechtel, M. Phalempin, S. Schlüter, D. Vetterlein, V. Schmidt, *Transp. Porous Media* **2023**, *149*, 501.

[6] M. B. Minus, S. R. Moor, F. F. Pary, L. P. T. Nirmani, M. Chwatko, B. Okeke, J. E. Singleton, T. L. Nelson, N. A. Lynd, E. V. Anslyn, *Org. Lett.* **2021**, *23*, 2873.

[7] J. Xie, W. Chen, G. Long, W. Gao, Z. J. Xu, M. Liu, Q. Zhang, *J. Mater. Chem. A* **2018**, *6*, 12985.

[8] M. Adil, M. Schmidt, J. Vogt, T. Diemant, M. Oschatz, B. Esser, *Batter. Supercaps* **2024**, e202400312.

[9] R. Shi, L. Liu, Y. Lu, Y. Li, S. Zheng, Z. Yan, K. Zhang, J. Chen, *Adv. Energy Mater.* **2021**, *11*, 2002917.

[10] M. Tang, S. Zhu, Z. Liu, C. Jiang, Y. Wu, H. Li, B. Wang, E. Wang, J. Ma, C. Wang, *Chem* **2018**, *4*, 2600.

[11] L. Wang, S. Fang, H. Wang, Q. Peng, Y. Liu, H. Dong, H. Yan, Y. Wang, S. Chou, B. Sun, Y. Xiao, S. Chen, *Carbon Energy* **2024**, e632.

[12] Y. Yao, M. Pei, C. Su, X. Jin, Y. Qu, Z. Song, W. Jiang, X. Jian, F. Hu, *Small* **2024**, *20*,

2401481.

[13] W. Zhang, T. Sun, W. Hao, M. Cheng, Z. Zha, M. Shi, Z. Tao, *Energy Storage Mater.* **2024**, *70*, 103561.

[14] L. Mo, G. Zhou, P. Ge, Y. E. Miao, T. Liu, *Sci. China Mater.* **2022**, *65*, 32.

[15] F. A. Obrezkov, A. F. Shestakov, V. F. Traven, K. J. Stevenson, P. A. Troshin, *J. Mater. Chem. A* **2019**, *7*, 11430.

[16] C. Huangfu, Z. Liu, X. Lu, Q. Liu, T. Wei, Z. Fan, *Energy Storage Mater.* **2021**, *43*, 120.

[17] L. W. Luo, W. Ma, P. Dong, X. Huang, C. Yan, C. Han, P. Zheng, C. Zhang, J. X. Jiang, *ACS Nano* **2022**, *16*, 14590.

[18] M. Mao, C. Luo, T. P. Pollard, S. Hou, T. Gao, X. Fan, C. Cui, J. Yue, Y. Tong, G. Yang, T. Deng, M. Zhang, J. Ma, L. Suo, O. Borodin, C. Wang, *Angew. Chemie Int. Ed.* **2019**, *58*, 17820.

[19] L. Chen, Y. Zhao, *Mater. Lett.* **2019**, *243*, 69.

[20] C. Wang, W. Tang, S. Jia, Y. Yan, D. Li, Y. Hu, J. Gao, H. Wu, M. Wang, S. Liu, H. Lai, T. Zou, L. Xu, J. Xiong, C. Fan, *Chem. Eng. J.* **2021**, *426*, 131251.

[21] Y. Hu, Y. Gao, L. Fan, Y. Zhang, B. Wang, Z. Qin, J. Zhou, B. Lu, *Adv. Energy Mater.* **2020**, *10*, 2002780.

[22] Y. Pang, H. Li, S. Zhang, Q. Ma, P. Xiong, R. Wang, Y. Zhai, H. Li, H. Kang, Y. Liu, L. Zhang, L. Zhang, T. Zhou, C. Zhang, *J. Mater. Chem. A* **2022**, *10*, 1514.

[23] D. Li, C. Wang, J. Hu, W. Tang, S. Jia, M. Guo, C. Fan, *Chem. Eng. J.* **2022**, *449*, 137745.

[24] D. Ruiz-Martínez, T. Lana-Villarreal, R. Gómez, *ACS Appl. Energy Mater.* **2021**, *4*, 6806.

[25] R. Thangavel, M. Moorthy, B. K. Ganesan, W. Lee, W. Yoon, Y. Lee, *Small* **2020**, *16*, 2003688.

[26] M. R. Raj, N. Kim, G. Lee, *Sustain. Energy Fuels* **2021**, *5*, 175.

[27] Y. Wu, X. Chen, G. Lin, X. Zhu, J. Qiu, Y. Luo, Z. Xu, Q. Chen, V. Ganesh, R. Zeng, *J. Electroanal. Chem.* **2020**, *877*, 114749.

[28] K. Li, Y. Wang, B. Gao, X. Lv, Z. Si, H. guo Wang, *J. Colloid Interface Sci.* **2021**, *601*, 446.

[29] X. Liu, Z. Ye, *Adv. Energy Mater.* **2021**, *11*, 2003281.

[30] Z. Sun, K. Zhu, P. Liu, H. Li, L. Jiao, *Adv. Funct. Mater.* **2021**, *31*, 2107830.

[31] J. Chen, H. Yin, Q. Xue, J. Zhang, X. Chen, X. Liu, R. He, L. Zhu, F. Wu, *Adv. Funct. Mater.* **2024**, 2411362.

[32] G. Ding, L. Zhu, Q. Han, L. Xie, X. Yang, L. Chen, G. Wang, X. Cao, *Electrochim. Acta* **2021**, *394*, 139116.

[33] Y. Wang, P. Bai, B. Li, C. Zhao, Z. Chen, M. Li, H. Su, J. Yang, Y. Xu, *Adv. Energy Mater.* **2021**, *11*, 2101972.

[34] Y. Hu, Q. Yu, W. Tang, M. Cheng, X. Wang, S. Liu, J. Gao, M. Wang, M. Xiong, J. Hu, C. Liu, T. Zou, C. Fan, *Energy Storage Mater.* **2021**, *41*, 738.

[35] Y. Wu, X. Mao, M. Zhang, X. Zhao, R. Xue, S. Di, W. Huang, L. Wang, Y. Li, Y. Li, *Adv. Mater.* **2021**, *33*, 2106079.

[36] R. Chu, H. Song, Z. Ullah, Z. Guan, Y. Zhang, L. Zhao, M. Chen, W. Li, Q. Li, L. Liu, *Electrochim. Acta* **2020**, *362*, 137115.

[37] F. Y. Chou, J. C. Tang, H. Y. Lee, J. C. Lee, S. Ratchahat, T. H. Chen, W. Kaveevivitchai, *ACS Appl. Energy Mater.* **2020**, *3*, 11300.

[38] H. Banda, D. Damien, K. Nagarajan, M. Hariharan, M. M. Shaijumon, *J. Mater. Chem. A* **2015**, *3*, 10453.

[39] W. Deng, X. Liang, X. Wu, J. Qian, Y. Cao, X. Ai, J. Feng, H. Yang, *Sci. Rep.* **2013**, *3*, 2671.

[40] L. Chen, Y. Li, Y. Zhang, S. Ren, J. Bi, X. Xue, D. Han, D. Wu, Y. Wang, X. Chen, Y. Wu, *Chem. Eng. J.* **2024**, *497*, 154743.

[41] K. Sakaushi, E. Hosono, G. Nickerl, T. Gemming, H. Zhou, S. Kaskel, J. Eckert, *Nat. Commun.* **2013**, *4*, 1485.

[42] J. Kim, S. Park, S. Hwang, W. S. Yoon, *J. Electrochem. Sci. Technol.* **2022**, *13*, 19.

[43] Y. C. Chien, H. Liu, A. S. Menon, W. R. Brant, D. Brandell, M. J. Lacey, *Nat. Commun.* **2023**, *14*, 35.

[44] S. D. Kang, W. C. Chueh, *J. Electrochem. Soc.* **2021**, *168*, 120504.

[45] M. Yin, K. Guo, J. Meng, Y. Wang, H. Gao, Z. Xue, *Adv. Mater.* **2024**, *36*, 2405747.

[46] T. Sun, X. Feng, Q. Sun, Y. Yu, G. Yuan, Q. Xiong, D. Liu, X. Zhang, Y. Zhang, *Angew. Chemie Int. Ed.* **2021**, *60*, 26806.

[47] D. Werner, D. H. Apaydin, E. Portenkirchner, *Batter. Supercaps* **2018**, *1*, 160.

[48] G. Zhou, L. Mo, C. Zhou, Y. Wu, F. Lai, Y. Lv, J. Ma, Y. E. Miao, T. Liu, *Chem. Eng. J.* **2021**, *420*, 127597.

[49] Q. Wang, B. Zhao, S. Zhang, X. Gao, C. Deng, *J. Mater. Chem. A* **2015**, *3*, 7732.

[50] Y. Wang, Y. Ding, L. Pan, Y. Shi, Z. Yue, Y. Shi, G. Yu, *Nano Lett.* **2016**, *16*, 3329.

[51] S. Guo, Y. Sun, J. Yi, K. Zhu, P. Liu, Y. Zhu, G. Zhu, M. Chen, M. Ishida, H. Zhou, *NPG Asia Mater.* **2016**, *8*, e266.

[52] D. Li, W. Tang, C. Y. Yong, Z. H. Tan, C. Wang, C. Fan, *ChemSusChem* **2020**, *13*, 1991.

[53] M. J. Frisch, G. W. Trucks, H. B. Schlegel, G. E. Scuseria, M. A. Robb, J. R.Cheeseman, G. Scalmani, V. Barone, G. A. Petersson, H. Nakatsuji, X. Li,M. Caricato, A. V. Marenich, J. Bloino, B. G. Janesko, R. Gomperts, B. Mennucci, H. P. Hratchian, J. V. Ortiz, A. F. Izmaylov, J. L. Sonnenberg, D. Williams-Young, F. Ding, F. Lipparini, F. Egidi, J. Goings, B. Peng, A. Petrone, T. Henderson, D. Ranasinghe, V. G. Zakrzewski, J. Gao, N. Rega, G. Zheng, W. Liang, M. Hada, M. Ehara, K. Toyota, R. Fukuda, J. Hasegawa, M. Ishida, T. Nakajima, Y. Honda, O. Kitao, H. Nakai, T. Vreven, K. Throssell, J. A. Montgomery, J. E. P. Jr., F. Ogliaro, M. J. Bearpark, J. J. Heyd, E. N. Brothers, K. N. Kudin, V. N. Staroverov, T. A. Keith, R. Kobayashi, J. Normand, K. Raghavachari, A. P. Rendell, J. C. Burant, S. S. Iyengar, J. Tomasi, M. Cossi, J. M. Millam, M. Klene, C. Adamo, R. Cammi, J. W. Ochterski, R. L. Martin, K. Morokuma, O. Farkas, J. B. Foresman, D. J. Fox, 2016, *Gaussian 16, Revision B.01*

[54] GaussView, Version 6.1, R. Dennington, T. A. Keith, and J. M. Millam, Semichem Inc., Shawnee Mission, KS, 2016.